

# Short-Wave Vortex Instabilities in Stratified Flow

by

Luke Bovard

A thesis  
presented to the University of Waterloo  
in fulfillment of the  
thesis requirement for the degree of  
Master of Mathematics  
in  
Applied Mathematics

Waterloo, Ontario, Canada, 2013

© Luke Bovard 2013

I hereby declare that I am the sole author of this thesis. This is a true copy of the thesis, including any required final revisions, as accepted by my examiners.

I understand that my thesis may be made electronically available to the public.

## Abstract

Stratified flow is the essential underlying physical model for atmospheric and stratified flow. In recent years, the study of stratified turbulence has been more thoroughly investigated due to its difference from classical turbulence. As a first step to investigating the mechanisms of turbulence, linear stability plays a critical role in determining under what conditions a flow remains stable or becomes turbulent. In the study of transition to stratified turbulence, a common vortex model, known as the Lamb-Chaplygin dipole, is used to investigate the conditions under which stratified flow transitions to turbulence. Numerous investigations have determined that a critical length scale, known as the buoyancy length, plays a key role in the breakdown and transition to stratified turbulence. At this buoyancy length scale, an instability unique to stratified flow, the zigzag instability provides the mechanisms for this break down. In this thesis we discover and investigate a new instability of the Lamb-Chaplyin dipole that exists at the sub-buoyancy scale. Through numerical linear stability analysis we show that this short-wave instability exhibits growth rates similar to that of the zigzag instability. We conclude with nonlinear studies of this short-wave instability and demonstrate this new instability saturates at a level proportional to the aspect ratio.

## Acknowledgements

Thanks to my supervisor Dr. Michael Waite. Good luck with the new addition to your family. Additional thanks goes to Dr. Marek Statsna and Dr. Francis Poulin.

Obligatory thanks to everyone else who I have learnt from and talked to over all these year. There are too many to name, so I won't. Just know that if you knew me I'd probably thank you. This saves me having to remember people and just cover everyone in one full swoop.

The work for this thesis was written under the music of, in order of most played, Queen, Taylor Swift, The Beatles, Dire Straits, and Billy Joel. I kept statistics and it works out to be a few thousands plays of each, which is probably about 4 days straight of music per artists!

Richard you wanted me to add you punching Chris by mistake many years ago to this thesis. Here you go.

Special thanks to Patricia for making the last few months bearable. It made writing this thesis much easier. Thanks et merci y gracias por todo.

Finally, and most importantly, I dedicate this thesis to the two best teachers I've ever had. Without both of them, who knows where I'd be now.

## **Dedication**

To Dr. Edward Vrscaj and Dr. Jamal Sakhr.

# Table of Contents

List of Tables	ix
List of Figures	x
<b>1 Introduction</b>	<b>1</b>
<b>2 Fluids Background</b>	<b>2</b>
2.1 Boussinesq approximation . . . . .	2
2.2 Linear stability analysis . . . . .	5
2.3 The zigzag instability . . . . .	10
2.3.1 A Brief History of Vortex Instabilities . . . . .	10
2.3.2 Discovery of the Zigzag Instability . . . . .	11
2.4 Formulation of the linear problem . . . . .	14
2.4.1 The Lamb-Chaplygin Dipole . . . . .	15
2.5 Scaling analysis . . . . .	17
2.5.1 Stratified Turbulence (to be written when nonlinear chapter is written)	21
<b>3 Numerical Background</b>	<b>22</b>
3.1 Spectral Methods Motivation . . . . .	22
3.2 FFT and Spectral Derivatives . . . . .	23
3.3 Dealiasing . . . . .	26

3.3.1	Spectral Method . . . . .	28
3.3.2	Pseudospectral Method . . . . .	34
3.3.3	Spectral vs Psuedospectral . . . . .	35
3.4	Timestepping and Examples . . . . .	35
3.5	Navier-Stokes in Fourier Space . . . . .	39
3.5.1	Fourier Transformed Navier-Stokes . . . . .	39
3.5.2	Projection Tensor . . . . .	43
3.5.3	Numerical Formulation of NS in Fourier . . . . .	43
3.5.4	Integrating Factor . . . . .	44
3.5.5	Hyperviscosity . . . . .	45
3.5.6	Concluding Remarks . . . . .	46
3.6	Numerical Scheme for Linear and Nonlinear Boussinesq Equations . . . . .	46
3.6.1	Linear Boussinesq Equations Scheme . . . . .	46
3.6.2	Nonlinear Boussinesq Scheme . . . . .	49
<b>4</b>	<b>Linear Theory</b>	<b>50</b>
4.1	Introduction . . . . .	50
4.2	Set-up . . . . .	50
4.3	Growth Rate . . . . .	51
4.4	Structure . . . . .	57
4.5	Subdominant modes . . . . .	68
4.5.1	Krylov Eigenvalue Routines . . . . .	69
4.5.2	Results . . . . .	71
4.6	Dimensional Analysis . . . . .	72
<b>5</b>	<b>Nonlinear theory</b>	<b>76</b>
5.1	Set-up . . . . .	76
5.2	Results . . . . .	79

<b>6</b>	<b>Conclusions</b>	<b>87</b>
	<b>APPENDICES</b>	<b>88</b>
<b>A</b>	<b>Spectral Example in Matlab</b>	<b>89</b>
	<b>References</b>	<b>91</b>



# List of Tables

# List of Figures

2.1	(get permission from JFM for picture + caption) A sequence of frontal (top) and side (bottom) views showing the growth of the zigzag instability for $F_h = 0.19$ and $Re = 365$ . From left to right the pictures are taken at 7, 36, 75, 109, 121, 176 seconds after the flaps have closed. The vortex pair is propagating to the left. In this experiment, tape has been applied to force the the natural wavelength of the instability to produce a clearer result. . .	13
2.2	The Lamb-Chaplygin dipole. . . . .	16
3.1	Spectral differentiation of two functions $\max(0, 1 -  x - \pi /2)$ (top) and $e^{\sin x}$ (bottom) from [48]. On the right is the spectral derivative computed with $n = 24$ . Red curve represents the exact derivative. Even as such small $N$ , the derivative of $e^{\sin x}$ is very smooth and the error is on the order of $\mathcal{O}(10^{-13})$ . The spectral derivative of $\max(0, 1 -  x - \pi /2)$ is not as good due to the discontinuity at $x = \pi$ . . . . .	27
3.2	Different sine curves that fit the same set of data points [60]. This is an example of aliasing. . . . .	31
3.3	Stability region of Adams-Bashforth second order. Adapted from [48] . . .	38
3.4	Spectral solution to the advection equation with variable windspeed. Figure is a reproduced version of Output 6 of Trefethen [48] . . . . .	40
3.5	Solution to the viscous Burgers equation using spectral (red) and pseudospectral (blue). . . . .	41
3.6	The inverse diffusion times, $1/\tau_d$ , of the wavenumbers for the regular viscosity, blue, and the hyperviscosity case, red. The hyperviscosity inverse diffusion times are lower then the regular viscosity case, corresponding to longer diffusion times. This has the effect of simulating larger Reynolds numbers. Note that at $k_{max}$ the two cases coincide. . . . .	47

4.1	Time series of the growth rate, obtained from the derivative of the energy, for $F_h = 0.1$ and $Re = 10,000$ . Panel (a) is $k_z = 20$ and Panel (b) is $k_z = 60$ .	52
4.2	Growth rate $\sigma$ as a function of $k_z F_h$ for fixed $F_h =$ (a) 0.2, (b) 0.1, (c) 0.05 with $Re = 2000$ (cyan), $Re = 5000$ (red), $Re = 10000$ (black), $Re = 20,000$ (blue). In panel (b) the green line is the hyperviscosity case with $Re = 20,000$ .	53
4.3	Imaginary part of the growth rate for $F_h = 0.05$ and $Re = 20,000$ (blue) and $Re = 10,000$ (black).	55
4.4	Growth rate $\sigma$ as a function of $k_z F_h$ for fixed $Re =$ (a)20,000, (b)10000, (c)5000 with $F_h = 0.05$ (red), $F_h = 0.1$ (black), $F_h = 0.2$ (blue).	56
4.5	The location of the second peak as a function of the buoyancy Reynolds number $Re_b$ . $k_z F_h$ is taken from Fig. 4.2. The straight line is $Re_b^{2/5}$ .	58
4.6	Growth rate $\sigma$ as a function of $F_h k_z$ for fixed $Re_b$ . In (a), red is $Re = 20,000, F_h = 0.1$ and blue is $Re = 5000, F_h = 0.2$ , both corresponding to $Re_b = 500$ ; in (b) red is $Re = 20,000, F_h = 0.05$ and blue is $Re = 5000, F_h = 0.1$ , both corresponding to $Re_b = 50$ .	59
4.7	Perturbation vertical vorticity $\omega_z$ at the zigzag peak for $F_h = 0.2$ (left) , 0.1 (middle) , 0.05 (right) and $Re = 20,000$ .	60
4.8	Perturbation fields $u, v, w, \rho$ at the zigzag peak for $F_h = 0.1$ and $Re = 20,000$ . Here $k_z = 6$ .	61
4.9	Perturbation vertical vorticity $\omega_z$ at local oscillatory minimum for $Re = 20,000$ (top) , 10000 (middle) , 5000 (bottom) ; and $F_h = 0.2$ (left) , 0.1 (middle) , 0.05 (right) .	
4.10	Perturbation fields $u, v, w, \rho$ at the oscillatory minimum for $F_h = 0.1$ and $Re = 20,000$ . Here $k_z = 20$ .	63
4.11	Perturbation vertical vorticity $\omega_z$ at second peak for $Re = 20,000$ (top) , 10000 (middle) , 5000 (bottom) and $F_h = 0.2$ (left) , 0.1 (middle) , 0.05 (right) .	64
4.12	Perturbation fields $u, v, w, \rho$ at the short wave instability for $F_h = 0.1$ and $Re = 20,000$ . Here $k_z = 60$ .	65
4.13	Perturbed vertical vorticity $\omega_z$ at (a) the zigzag peak (b) the second peak for $Re = 5000, F_h = 0.2$ .	66
4.14	Structure of the v velocity from $k_z = 3$ up to $k_z = 110$ for $F_h = 0.1$ and $Re = 20,000$ . The wavenumber is increasing left to right and top to bottom. Here the scaling has not been applied to better illustrate the structure.	67

4.15	Angle of the wake behind the v velocity field as a function of the perturbation wavelength for $F_h = 0.1$ and $Re = 20,000$ . The red line is a reference slope of 1. . . . .	68
4.16	Krylov methods with two different choices of $n = 50$ (left), $100$ (right) for $Re = 10000$ , $N = 256$ , $F_h = 0.1$ . Star denotes the dominant eigenvalues from the energy method, circle is the leading approximation from the Krylov method, triangle and x are the second and third eigenvalues respectively. . .	71
4.17	Growth rate $\sigma$ as a function $k_z$ at $Re = 10,000$ with $F_h = \infty$ (green), $F_h = 0.2$ (blue), $F_h = 0.1$ (black), $F_h = 0.05$ (red) . . . . .	75
5.1	Time series of the potential energy (circle) and kinetic energy (star) for $L = 5$ (blue) and $L = 9$ (black). . . . .	78
5.2	Time series of the kinetic energy (top line) and potential energy (bottom line) for $Re = 5000$ and $F_h = 0.2$ . . . . .	80
5.3	Saturation levels for a range of aspect ratios for $Re = 2000$ and $F_h = 0.2$ . . .	81
5.4	Saturation levels for a range of aspect ratios for $Re = 5000$ and $F_h = 0.2$ . . .	82
5.5	Growth rate for $Re = 5000$ and $F_h = 0.2$ with the linear results (red) and the nonlinear results (blue). Note we have not scaled by $F_h$ unlike the results in Chapter 3. . . . .	86

# Chapter 1

## Introduction

The buoyancy scale is  $L_b = U/N$  although sometimes a factor of  $2\pi$  is included as well. What does this number represent? In the atmosphere,  $U \sim 10$  m/s and  $N \sim 10^{-2}$  s $^{-1}$ .

# Chapter 2

## Fluids Background

### 2.1 Boussinesq approximation

The Navier-Stokes equations are the mathematical equations that govern the evolution of fluid flow. In the context of the ocean and atmosphere, the Navier-Stokes equations, along with equations for conservation of mass, energy, and state provide good models of the evolution of fluid flow (e.g. Batchelor[5]). For our purposes, however, these equations are too general and an approximation, called the Boussinesq approximation, can be made which results in a simplified version of the Navier-Stokes equations:

$$\frac{\partial \mathbf{u}}{\partial t} + \mathbf{u} \cdot \nabla \mathbf{u} = -\frac{1}{\rho_0} \nabla p - \frac{\rho' g}{\rho_0} \hat{\mathbf{e}}_z + \nu \nabla^2 \mathbf{u}, \quad (2.1)$$

$$\nabla \cdot \mathbf{u} = 0, \quad (2.2)$$

$$\frac{\partial \rho'}{\partial t} + \mathbf{u} \cdot \nabla \rho' = \kappa \nabla^2 \rho' - \frac{\partial \bar{\rho}}{\partial z} w, \quad (2.3)$$

where we have the following dimensional variables

- $\mathbf{u}(x, y, z, t) = (u(x, y, z, t), v(x, y, z, t), w(x, y, z, t))$  is the velocity field in the  $x, y, z$ -directions respectively,
- $p(x, y, z, t)$  is the pressure field,
- $\rho(x, y, z, t)$  is the density,
- $\rho_0$  is a constant reference density,

- $\bar{\rho}(z)$  is a background density profile,
- $\rho'(x, y, z, t)$  is a perturbation density,
- $g$  is the gravitational constant,
- $\nu$  is the constant kinematic velocity,
- $\kappa$  is the constant molecular diffusivity.

Equations (2.1)-(2.3) are a set of five coupled partial differential equations for the unknowns  $\mathbf{u}, p, \rho$ . Herein, we will refer to equation (2.1) as the velocity equations, equation (2.2) as the continuity equation, and equation (2.3) as the density equation. An additional useful quantity is the buoyancy frequency or the Brunt-Väisälä frequency which is defined as

$$N^2 = -\frac{g}{\rho_0} \frac{d\bar{\rho}}{dz}. \quad (2.4)$$

Note that we have included a negative sign because we assume that the density profile is decreasing. We now assume that  $N$  is constant, which implies a linear background density profile.

A rigorous derivation of the Boussinesq equation is quite delicate and we provide a brief overview of the derivation. A complete derivation, along with many of the subtleties can be found in numerous books such as [27, 49, 51] and a rigorous mathematical derivation in (Spiegel and Veronis). The Navier-Stokes equations for a compressible Newtonian fluid can be written as

$$\rho \frac{D\mathbf{u}}{Dt} = -\nabla p + \rho \mathbf{g} + \mu \nabla^2 \mathbf{u}, \quad (2.5)$$

$$\frac{1}{\rho} \frac{D\rho}{Dt} + \nabla \cdot \mathbf{u} = 0. \quad (2.6)$$

The Boussinesq equations are based on the following decomposition of the density [27, 51]

$$\rho(\mathbf{x}, t) = \rho_0 + \bar{\rho}(z) + \rho'(\mathbf{x}, t) \quad (2.7)$$

where we assume that  $\rho' \ll \bar{\rho}(z) \ll \rho_0$ . In other words, variations to the density are small compared to a reference density.

The first approximation we make is replacing the mass continuity equation with the more simple incompressible equation  $\nabla \cdot \mathbf{u} = 0$ . However, since we are interested in a fluid

with non-constant density, it is not as simple as setting  $\rho = \rho_0$ . The approximation we make is that even though the density is non-constant, it is approximately in hydrostatic balance [51]. Thermodynamically [27], this means that density varies as

$$\frac{\delta\rho}{\rho} = -\alpha\delta T \quad (2.8)$$

where  $\alpha$  is the thermal expansion coefficient, which for many gases is on the order of  $10^{-3} \text{ K}^{-1}$  and fluids  $10^{-4} \text{ K}^{-1}$  [27]. If the variation in temperature  $\delta T \sim 10 \text{ K}$ , which is a reasonable approximation for many applications of oceanic and atmospheric modeling, then  $\alpha\delta T \ll 1$ . Comparing the material derivative and the velocity term in the conservation equation yields, assuming a characteristic velocity and length scales of  $U$  and  $L$  [27],

$$\frac{(1/\rho)(D\rho/Dt)}{\nabla \cdot \mathbf{u}} \sim \frac{(U/\rho)\delta\rho/L}{U/L} = \frac{\delta\rho}{\rho} \ll 1. \quad (2.9)$$

Thus we can replace the mass continuity with the “incompressibility condition”.

We have simplified the equations of motion, however we still have five unknowns with only four equations. To get a fifth equation, we again appeal to thermodynamics. It can be shown that given the above density approximation, the thermodynamic equation of state of the density [51] can be written as

$$\frac{D\rho'}{Dt} - N^2 w = \kappa \nabla^2 \rho' \quad (2.10)$$

which closes the system. Finally, in the momentum equation, if we plug in the density approximation we obtain

$$\left(1 + \frac{\bar{\rho}}{\rho_0} + \frac{\rho'}{\rho_0}\right) \frac{D\mathbf{u}}{Dt} = -\frac{1}{\rho_0} \nabla p + \left(1 + \frac{\bar{\rho}}{\rho_0} + \frac{\rho'}{\rho_0}\right) \mathbf{g} + \mu \nabla^2 \mathbf{u}. \quad (2.11)$$

The terms multiplying the interial terms are tiny and can be neglected [27]. The terms multiplied gravity need to be treated more carefully because of the hydrostatic balance condition. The resulting equation is [27, 51] is

$$\frac{\partial \mathbf{u}}{\partial t} + \mathbf{u} \cdot \nabla \mathbf{u} = -\frac{1}{\rho_0} \nabla p - \frac{\rho' g}{\rho_0} \hat{\mathbf{e}}_z + \nu \nabla^2 \mathbf{u}. \quad (2.12)$$

Thus we have derived the so-called Boussinesq approximation.



## 2.2 Linear stability analysis

The stability of flows has a long and rich history within fluid dynamics. The classic experiment into the stability of fluid flow is that of Reynolds [43]. In this experiment, Reynolds injected dye into the laminar flow through a pipe. By varying the velocity of the flow through the pipe Reynolds observed various effects. If the velocity was sufficiently low, Reynolds was able to observe “a beautiful straight line through the tube”. At slightly higher velocities, the straight line behaviour remained near the initial part of the pipe but further down “the streak would shift about the tube, but there was no appearance of sinuosity”. By increasing the velocity significantly, the dye would again initially remain straight near the initial part of the tube, but instead of shifting about the tube “the colour band would all at once mix up with the surrounding water, and fill the rest of the tube with a mass of coloured water”. (add image from Acheson?)

What Reynolds observed was the transition and breakdown of a flow into turbulence. Through careful observation, he determined that the dimensionless quantity that governed the behaviour of the flow was the Reynolds number

$$Re = \frac{UL}{\nu}, \quad (2.13)$$

a number which, as discussed above represents the ratio between the inertial and viscous terms in the Navier-Stokes equations. Reynolds found that if  $Re < 13000$  then the flow would remain stable.

The natural question to ask is to whether we can predict such criteria for any given flow. Ideally, given information about a certain flow, one would be like to be able to determine how the fluid will evolve based on various parameters of the flow, such as viscosity, temperature, or velocity. Unfortunately this task has not been achieved in general and there is no known way to determine such criteria for any arbitrary flow. This is due to the complicated nonlinear behaviour of the Navier-Stokes equations which makes devising a general algorithm for this task incredibly difficult. Tackling this goal in general is immensely difficult and beyond current mathematics, indeed it is not even known whether or not in three dimensions given an initial condition a solution even exists for all times.

Thus, to proceed, a simplifying approach must be derived. In order to do this, consider the following idea. Let  $(\mathbf{u}_0, p)$  denote a basic state that solves the Navier-Stokes equations and let  $(\mathbf{u}', p')$  denote a small unknown perturbation such that  $|\mathbf{u}', p'| \ll |\mathbf{u}_0, p|$ . Mathematically this means

$$\mathbf{u}(\mathbf{x}, t) = \mathbf{u}_0(\mathbf{x}, t) + \mathbf{u}'(\mathbf{x}, t), \quad p(\mathbf{x}, t) = p_0(\mathbf{x}, t) + p'(\mathbf{x}, t). \quad (2.14)$$

Now let us plug (2.14) into the Navier-Stokes equations and expand, dropping the  $(\mathbf{x}, t)$  notation,

$$\frac{\partial \mathbf{u}_0}{\partial t} + \frac{\partial \mathbf{u}'}{\partial t} + (\mathbf{u}_0 + \mathbf{u}') \cdot \nabla (\mathbf{u}_0 + \mathbf{u}') = -\frac{1}{\rho_0} \nabla (p_0 + p') + \nu \nabla^2 (\mathbf{u}_0 + \mathbf{u}'), \quad (2.15)$$

$$\nabla \cdot \mathbf{u}_0 + \nabla \cdot \mathbf{u}' = 0. \quad (2.16)$$

Expanding out the advection term yields

$$(\mathbf{u}_0 + \mathbf{u}') \cdot \nabla (\mathbf{u}_0 + \mathbf{u}') = \mathbf{u}_0 \cdot \nabla \mathbf{u}_0 + \mathbf{u}_0 \cdot \nabla \mathbf{u}' + \mathbf{u}' \cdot \nabla \mathbf{u}_0 + \mathbf{u}' \cdot \nabla \mathbf{u}' \quad (2.17)$$

$$= \mathbf{u}_0 \cdot \nabla \mathbf{u}_0 + \mathbf{u}_0 \cdot \nabla \mathbf{u}' + \mathbf{u}' \cdot \nabla \mathbf{u}_0 + \mathcal{O}(\mathbf{u}'^2), \quad (2.18)$$

where we have written the  $\mathbf{u}' \cdot \nabla \mathbf{u}'$  term has  $\mathcal{O}(\mathbf{u}'^2)$  because this term is of order  $\mathbf{u}'$  squared, which we assume to be small. Now recall that the basic state  $\mathbf{u}_0$  solves the Navier-Stokes equations. Thus in (2.16) there are terms that depend just on  $\mathbf{u}_0$  and they will vanish by definition of it being a solution to the Navier-Stokes equations. Thus we now have that

$$\frac{\partial \mathbf{u}'}{\partial t} + \mathbf{u}_0 \cdot \nabla \mathbf{u}' + \mathbf{u}' \cdot \nabla \mathbf{u}_0 + \mathcal{O}(\mathbf{u}'^2) = -\frac{1}{\rho_0} \nabla p' + \nu \nabla^2 \mathbf{u}' \quad (2.19)$$

$$\nabla \cdot \mathbf{u}' = 0. \quad (2.20)$$

So far, the equation above is exact and we have just suppressed the quadratic nonlinear term in the Big-O notation. Now the critical assumption we make is that because  $\mathbf{u}'$  is small relative to the basic state  $\mathbf{u}_0$ ,  $\mathbf{u}'^2$  is even smaller and thus is negligible. In other words, we are throwing away the quadratic nonlinearity of the perturbation term because it assumed to be small.

Now making the approximation that  $\mathcal{O}(\mathbf{u}'^2)$  is small we obtain

$$\frac{\partial \mathbf{u}'}{\partial t} + \mathbf{u}_0 \cdot \nabla \mathbf{u}' + \mathbf{u}' \cdot \nabla \mathbf{u}_0 = -\frac{1}{\rho_0} \nabla p' + \nu \nabla^2 \mathbf{u}' \quad (2.21)$$

$$\nabla \cdot \mathbf{u}' = 0. \quad (2.22)$$

The above set of equations is linear which means they are more amenable to analytical and numerical techniques.

To illustrate the usefulness in this approach, we demonstrate an example of the general idea of linear stability and apply it to the formulation of the experiment of Reynolds. This is a standard example and we follow the derivation of [21]. It will also elucidate the key features of linear stability analysis that we will use throughout this thesis.

The first simplifying assumption we make is that the basic state  $\mathbf{u}_0 = U(z)\hat{\mathbf{e}}_x$ , a parallel shear flow, which simplifies the above equations to

$$\frac{\partial \mathbf{u}'}{\partial t} + U \frac{\partial \mathbf{u}'}{\partial x} + w' \frac{dU}{dz} \hat{\mathbf{e}}_x = -\frac{1}{\rho_0} \nabla p' + \nu \nabla^2 \mathbf{u}' \quad (2.23)$$

$$\nabla \cdot \mathbf{u}' = 0. \quad (2.24)$$

If we had considered the Euler equations instead of the Navier-Stokes equations, we would have the same equations as above except with  $\nu = 0$ . Despite this seemingly simple modification, the resulting equation is very different. When the inviscid equations are considered, there are many elegant results about the stability of the flow that can be derived for the special case of parallel shear flow. For example, the Rayleigh's inflection point theorem states that a necessary condition for instability is that the basic velocity profile should have an inflection point[21]. Unfortunately, many of the results for inviscid flow theory do not hold for viscous flow theory. A complete discussion of this result and its generalisation, among other theorems, can be found in [21, 27].

Since the resulting set of equations is a set of coupled linear equations, the solution set is complex exponentials. Thus, the next natural step is to expand the solution as Fourier modes

$$\mathbf{u}'(\mathbf{x}, t) = \hat{\mathbf{u}}(z) e^{i(\alpha x + \beta y - \alpha c t)} \quad (2.25)$$

$$p'(\mathbf{x}, t) = \hat{p}(z) e^{i(\alpha x + \beta y - \alpha c t)} \quad (2.26)$$

where we take the real part of the above solutions. We require that the solution remains bounded as  $x, y \Rightarrow \pm\infty$  which means that  $\alpha, \beta$  must remain real. For  $c$ , however, we let it remain an arbitrary complex number  $c = c_r + i c_i$ . Depending on the sign of  $c_i$  the result will either decay or grown exponentially as time goes to infinity. We thus associate stability with  $c_i \leq 0$  and instability with  $c_i > 0$ . Hence, if we are able to solve the above system and derive a criteria for the value of  $c_i$  we will be able to derive some criteria for the stability of the flow.

Plugging in the above Fourier expansions into the linear equations would yield an eigenvalue-eigenvector problem with  $\alpha, \beta, c, Re$  being undetermined. From there we could apply numerical linear algebra routines to solve numerically for various  $Re, \alpha, \beta$  and obtain a stability curve for  $c$ . However, a result due to Squire allows us to simplify the problem significantly. Squire's theorem states that to obtain the minimum critical Reynolds number it is sufficient to consider only two-dimensional disturbances[21]. In other words, for every three dimensional mode, there is a more unstable two dimensional eigenmode. A proof is provided in [21]. Because we only need to consider two dimensional flow, the unknown

velocity  $\mathbf{u}'$  can be rewritten in terms of the stream function  $\psi'(x, y, z, t)$ . Another advantage of writing the equations in terms of the stream function is that the pressure is eliminated further reducing the number of unknowns.

Expanding  $\psi'$  as a complex exponential and denoting  $\phi$  as the amplitude of the stream function and  $D = d/dz$ , the linear equations can be re-written as a single equation,

$$(D^2 - \alpha^2)^2 \phi = (i\alpha Re)(U - c)(D^2 - \alpha^2)\phi - (i\alpha Re)U''\phi \quad (2.27)$$

along with the appropriate boundary conditions. This equation is known as the Orr-Sommerfeld equation and has a rich history in the development of fluid mechanics. A comprehensive discussion of the various methods of solving this equation and others like it using techniques such as WKB theory, asymptotics, and perturbation theory, is contained in [21, 52, 15].

This simple derivation has resulted in a single equation with three unknowns  $\alpha, c, Re$  and by choosing different  $Re$  and  $\alpha$ , we can determine a criteria for  $c$ . Although much work has been done at the beginning of the 20th century to derive approximate solutions to the Orr-Sommerfeld equation, numerically it is very easy to solve. We can reformulate the above equation as a generalised eigenvalue problem for a given parallel shear flow and solve the problem rather easily on a computer[48] and we can find that the condition for stability is  $Re \sim 5500$ , although the question of how valuable this is debatable[48].

Linear stability is a useful technique for determining whether or not a given flow is stable, however it is important to not forget the underlying assumptions. Since we are explicitly assuming that  $|\mathbf{u}'| \ll |\mathbf{u}_0|$  the resulting linear equations are only valid when this is the case. As we shall see in numerical simulations, this assumption is not necessarily valid at all times. If viscous dissipation is neglected, the Euler equations conserve energy. If there is viscous dissipation then the Navier-Stokes only approximately conserve energy, but even if we included a complicated mechanism for molecular dissipation, the resulting equations would still have to conserve energy, as long as there is no external forcing and thus if we were very careful and measured everything the total amount of energy in the system would remain constant. However we have stated that if  $c_i > 0$  then we have exponential growth. Clearly, as time advances, this gets infinitely large very quickly which implies that the perturbation will grow unbounded exponentially. This violates conservation of energy, since the total amount of energy of the perturbation is growing, and violates the assumption that the perturbation is small.

The reason this occurs in linear stability analysis is simple: we implicitly assume that the basic state remains undisturbed, i.e. that the perturbations are small enough so they do not change the basic state. This means, when running a numerical simulation, the

perturbation is able to grow in time while the basic state remains unchanged. Thus we can think of the basic state as continuously pumping in energy into the perturbation state, allowing it to grow unbounded. Physically, this is not the case. In a full nonlinear simulation, the basic state does not remain unchanged and as the perturbation begins to grow, the basic state loses energy and changes and eventually reaches a point where we can no longer assume the perturbation is small compared to the basic state. Thus we have a breakdown of the linear theory and would need to turn to a nonlinear theory to continue our modeling.

However, despite violating conservation of energy, linear stability still provides useful information. Even though the individual eigenmodes grow exponentially, which eigenmodes are growing gives insight into what mechanisms are causing the growth. As we shall see, linear stability theory tells us what length scales dominate in the transition to turbulence in a stratified fluid. Given this information, it is possible to assume a certain scaling of the full nonlinear equations which can provide us with a potential simplified model to study the problem of turbulence in stratified fluids.

So far, we have studied the Navier-Stokes equations directly instead of, the perhaps more promising, Euler equations. Recall the Euler equations arise by setting the viscosity to 0 or letting the Reynolds number go to infinity. The Euler equations also have some other nicer features, such as explicit conservation of energy which might provide a useful potential invariant that we can exploit in the study of stability and turbulence.

To motivate the possible use of the Euler equations, consider the observation that turbulence is very often observed at a high Reynolds number. In the atmosphere for example, the Reynolds number is on the order of  $10^8 - 10^9$  or higher. Since the inverse of the Reynolds number appears in front of the diffusion term, it seems reasonable to instead ignore the diffusion term since the coefficient is  $\mathcal{O}(\text{Re}^{-1}) \ll 1, \text{Re} \gg 1$ . This would be a mistake. This is because the limit  $\text{Re} \rightarrow \infty$  is a singular limit. Consider the following simplified model which arises in the study of boundary layers of shear bounded wall flow[15, 1, 27]

$$\epsilon y'' - y = 0 \quad y(0) = 0, \quad y(1) = 1. \quad (2.28)$$

If we set  $\epsilon = 0$  we would obtain the equation

$$-y = 0 \quad y(0) = 0, y(1) = 1. \quad (2.29)$$

which clearly has no solution that satisfies the boundary conditions. If we tried a perturbation expansion of the form  $y(x) = \sum_{n=0} y_n(x)\epsilon^n$  we would get nowhere because the lowest order term does not exist. If we solve the full equation, we see the problem with

setting  $\epsilon = 0$ ,

$$y(x) = \frac{e^{x/\epsilon} - 1}{e^{1/\epsilon} - 1}. \quad (2.30)$$

In this equation, we cannot set  $\epsilon = 0$  because that results in a singular limit. Thus regardless of how small we choose  $\epsilon$ , there will be a thin layer, called the boundary layer, which is essential to the fluid flow. For a discussion of techniques in singular perturbation theory in terms of the linear stability of the Navier-Stokes equations see [21, 52]. Hence, even though it seems reasonable to neglect the diffusion term to study instability and turbulence, it is not as a promising avenue as one might first expect. In one sense, this singular limit of the Navier-Stokes equations contributes to making turbulence a very difficult problem to investigate analytically and numerically.

Finally, the experimental investigation into instability of fluids and the transition to turbulence produces very appealing images which really illustrate the beauty of fluid dynamics and the reader is recommended to peruse the coffee table book by Van Dyke [53] which illustrates many images from experiments of the classical results in stability theory.

## 2.3 The zigzag instability

### 2.3.1 A Brief History of Vortex Instabilities

The origin of vortex instabilities begins with Lord Kelvin who in 1880 studied perturbations to columnar vortices and determined that they were stable. For the next 90 years, the theory of vortex instability remained relatively quiet until the field was re-ignited by the investigations Crow [18]. Motivated by engineering applications, Crow was an aeronautical engineer, he discovered that for long wavelength perturbations of a pair of counter-rotating vortices that there was a symmetric deformation of the vortices. This worked extended a few years later by Widnall et. al [59] to small wavelength perturbations. Further investigations into small wavelength perturbations were carried out by numerous others e.g. [38, 50]. It was noticed in these studies that the streamlines of the vortex became elliptical when perturbed. Motivated by this, Pierrehumbert [42] investigated the simple case of a single 2D elliptical vortex subject to a constant 3D perturbation. Extensions to this elliptical model were done by Bayly [4] and Waleffe [58] and led to this instability being called the elliptical instability. A complete and detailed history of the elliptical instability, including derivations and results of the above papers and nonlinear investigations, is presented in the review by Kerswell [25]. Most of the investigations into the elliptical instability were

concerned with unstratified flow, but an investigations by Miyazaki and Fukumoto [37] showed with sufficient stratification, the elliptical instability is suppressed.

### 2.3.2 Discovery of the Zigzag Instability

Experiments into this elliptical instability by Leweke and Williamson [30] led Billant, Brancher, and Chomaz [6] to investigate the stability of a three dimensional vortex pair which, as we shall discuss below, provides a good model of the experimental setup. Initially this work was unstratified and confirmed the existence of the elliptical instability. However, following up this work, Billant and Chomaz added in the effects of stratification and discovered a new type of instability at small scales that was distinct from the elliptical instability. They labeled this new instability the “zigzag instability” due to its zigzag-like structure, as we shall see below. In a series of three papers they investigated experimentally[7], theoretically[8], and numerically [9] the evolution of a pair of columnar vortices in a stratified tank.

First Billant and Chomaz investigated the zigzag instability experimentally [7]. To do this, they investigated a columnar vortex pair created by a pair of flaps in a tank of stratified fluid. We now briefly discuss their experimental procedure since it provides important motivation for the resulting numerical study.

In order to study the effects of stratification on the evolution of vortices, they first needs to create the vortices. To do this, they used a pair of motor-controlled flaps whose initial angle and closing time could be controlled precisely by a computer. When the flaps were closed, a pair of counter-rotating vortices was produced. They found that the important determining factor in the creation of the vortices was the angle of the flaps. If the angle was too small, additional vortices created when the flaps finally stopped closing were being advected by the dipole and causing spurious instability. For large angles fluid that was initially inbetween the flaps was being injected in the flow and again causing spurious oscillations. In order to balance out these effects, an angle of  $14^\circ$  was chosen. Additionally, to enforce the emergence of the zigzag instability, tape was applied to the flaps in order to force certain wavenumbers of the evolving flow, see Figure 8 of [7] for the importance of forcing.

After fixing the seperation angle they found that by varying the closing time of the flaps, the velocity of the pair of vortices could be changed. Interestingly, the decay of the vortices, roughly 90s, was independent of the closing time of the flaps. This variation in the velocity determined the experimental parameters for the experiment.

The two important dimensional parameters in this experiment were the horizontal Froude number

$$F_h = \frac{U}{NR} \quad (2.31)$$

and the Reynolds numbers

$$Re = \frac{UR}{\nu} \quad (2.32)$$

where  $U$  is the propagating velocity of the dipole as above,  $R$  is the radius of the dipole,  $\nu$  is the viscosity of the tank, and  $N$  is the buoyancy frequency. Here the viscosity  $\nu$  and the radius  $R$  were fixed by experimental conditions and could not be varied. Thus the only parameters that could be varied were  $N$  and  $U$ . Since the buoyancy frequency was more difficult to vary, as changing it required draining and refilling the tank, only four stratifications were considered ranging from  $N = 1.26 \text{ rad s}^{-1}$  to  $N = 1.97 \text{ rad s}^{-1}$ . Thus the parameter that was easy to control was the initial velocity  $U$ . Because  $U$  shows up in both dimensionless numbers, changing  $U$  resulted in the changing of both numbers, i.e. they are directly related by the following relationship

$$Re = F_h \frac{NR^2}{\nu} \quad (2.33)$$

and for the given stratification numbers the ranges for the Froude number were between 0.10 – 0.23 and for the Reynolds number 200 – 450.

To determine a theoretical model of the dipole, they computed the FFT of the measured vorticity in order to determine the streamfunction. They found that there was a linear fit between the vorticity  $\omega$  and the streamfunction  $\psi$  such that  $\omega = k^2\psi$  where  $k^2 = 1.15\text{cm}^{-2}$  which, as we will show below, corresponds to a columnar Lamb-Chaplygin dipole.

Figure 2.1 demonstrates the evolution for the zigzag instability for  $F_h = 0.19$  and  $Re = 365$ . The structure of the vortices displays a zigzag like structure. Additionally, the anisotropy between the vertical and horizontal directions is quite clear. The periodic behaviour of the vortex pair is also evident.

Following up the experimental work, Billant and Chomaz provided a theoretical account of the zigzag instability starting from the Boussinesq equations [8]. We will only discuss the main result of the paper as the paper is a very technical and long perturbation analysis. In the paper, they investigated the limit where  $F_{h,v} = U/L_{h,v}N \ll 1$  and found that the zigzag motion was accounted for by combination of translation and rotation, which agrees



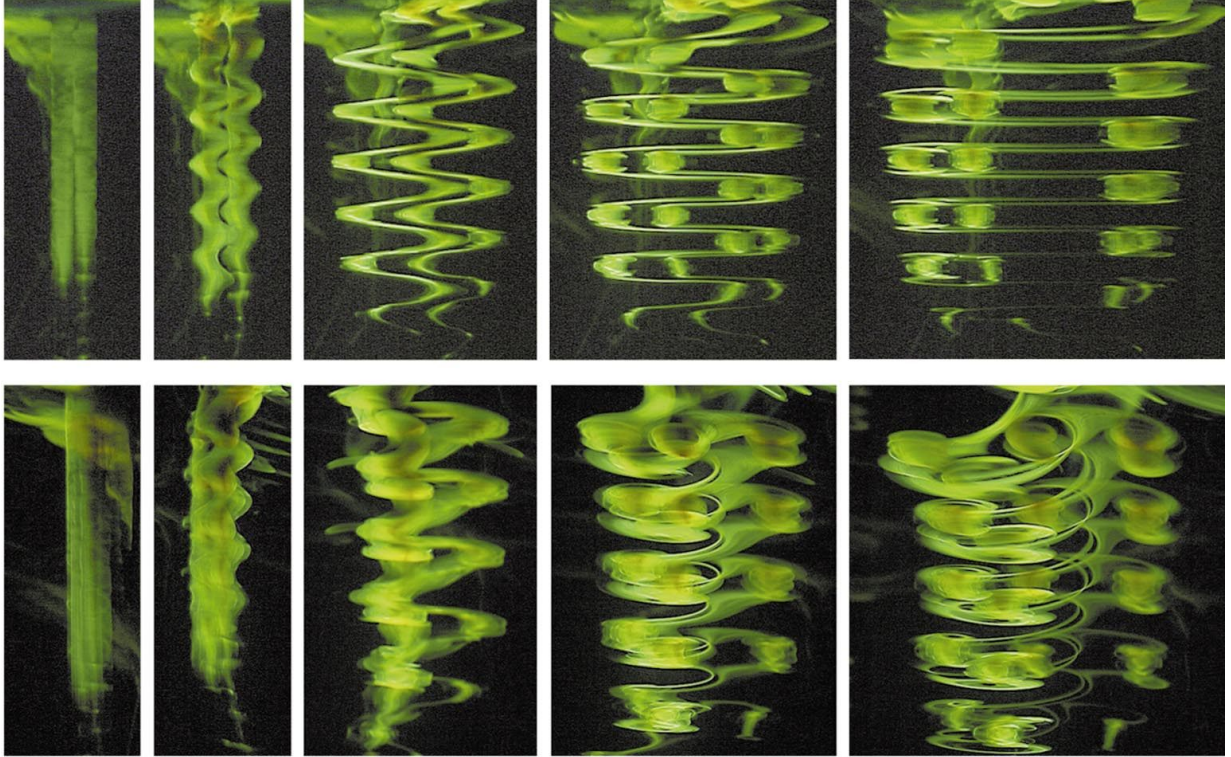


Figure 2.1: (get permission from JFM for picture + caption) A sequence of frontal (top) and side (bottom) views showing the growth of the zigzag instability for  $F_h = 0.19$  and  $Re = 365$ . From left to right the pictures are taken at 7, 36, 75, 109, 121, 176 seconds after the flaps have closed. The vortex pair is propagating to the left. In this experiment, tape has been applied to force the the natural wavelength of the instability to produce a clearer result.

with the experimental observations of [7]. Additionally, they found that the zigzag stability should behave as  $F_v \sim \mathcal{O}(1)$ , i.e.  $L_v \sim U/N$ . This length is known as the buoyancy length scale (cite) and has proven to be a very important length scale in stratified fluid flow, as we shall discuss below. This derivation of the buoyancy length scale, however, should be treated with some care since Billant and Chomaz assumed that  $F_v \ll 1$  and showed that  $F_v \sim \mathcal{O}(1)$ .

In the final paper, Billant and Chomaz conducted a numerical linear stability analysis of the zigzag instability [9]. In this study, they numerically solved the linear Boussinesq equations for the growth rate of the leading eigenmode for specific wavenumbers. We will not discuss the results details of the paper here as their paper forms the basis for much of this thesis and we will rederive and discuss their results throughout the next three chapters. In the remainder of this chapter we derive the numerical equations that Billant and Chomaz used in [9] and provide some more background information. In Chapter 3 we introduce and discuss the numerical technique of spectral methods used to solve the numerical equations. In Chapter 4 we extend the analysis of Billant and Chomaz to length scales well below the sub-buoyancy scale of  $L_b \sim U/N$ .

## 2.4 Formulation of the linear problem

Following Billant and Chomaz [9], we consider the non-dimensional Boussinesq approximation to the Navier-Stokes equations in Cartesian co-ordinates

$$\frac{D\mathbf{u}}{Dt} = -\nabla p - \rho' \hat{\mathbf{e}}_z + \frac{1}{Re} \nabla^2 \mathbf{u}, \quad (2.34)$$

$$\nabla \cdot \mathbf{u} = 0, \quad (2.35)$$

$$\frac{D\rho'}{Dt} - \frac{w}{F_h^2} = \frac{1}{ReSc} \nabla^2 \rho', \quad (2.36)$$

where  $D/Dt = \partial/\partial t + \mathbf{u} \cdot \nabla$ ,  $\mathbf{u} = (u, v, w)$  is the velocity,  $p$  is the pressure, and  $\rho'$  is the density perturbation. We have non-dimensionalised by the characteristic velocity  $U$ , length  $R$ , time-scale  $R/U$ , pressure  $\rho_0 U^2$ , density  $\rho_0 U^2/gR$ , and defined  $Sc = \nu/D$  as the Schmidt number, where  $D$  is the mass diffusivity,  $\rho_0$  is the background density, and  $g$  is the gravitational constant. The Reynolds and horizontal Froude number are as defined above. The buoyancy frequency  $N$ , and hence the Froude number  $F_h$ , is assumed to be constant.

In order to investigate the linear growth rate, we proceed as the introduction and

expand the full velocity field as the sum of a basic state and a perturbation state.

$$\mathbf{u} = \mathbf{u}_0 + \tilde{\mathbf{u}} \quad (2.37)$$

$$p = p_0 + \tilde{p} \quad (2.38)$$

$$\rho' = \rho'_0 + \tilde{\rho}' \quad (2.39)$$

here the basic state is the Lamb-Chaplygin dipole which we will now discuss and explain how it provides a convenient theoretical model for the experiment by Billant and Chomaz [7].

### 2.4.1 The Lamb-Chaplygin Dipole

As the basic state for linear stability analysis we use the Lamb-Chaplygin dipole in a comoving frame [35]. This dipole is a solution to the 2D inviscid Euler equations. This basic state is motivated by numerous laboratory experiments[7, 30], as discussed above, which demonstrated that a vertically oriented Lamb-Chaplygin dipole is a good approximation to the vortex generated by two flaps closing in a tank of salt-stratified water. The dipole, in cylindrical coordinates, is given by the stream function

$$\psi_0(r, \theta) = \begin{cases} -\frac{2}{\mu_1 J_0(\mu_1)} J_1(\mu_1 r) \sin \theta & r \leq 1, \\ -r \left(1 - \frac{1}{r^2}\right) \sin \theta & r > 1, \end{cases} \quad (2.40)$$

and the corresponding vertical vorticity  $\omega_{z0} = \nabla_h^2 \psi_0$

$$\omega_{z0}(r, \theta) = \begin{cases} \mu_1^2 \psi_0(r, \theta) & r \leq 1, \\ 0 & r > 1, \end{cases} \quad (2.41)$$

where  $J_0, J_1$  are the zero and first order Bessel functions,  $\mu_1 \approx 3.8317$  is the first root of  $J_1$ , and  $\nabla_h$  is the horizontal Laplacian. The basic state velocity is purely horizontal and is given by  $\mathbf{u}_{h0} = \nabla_h \psi_0 \times \hat{\mathbf{e}}_z$ . Recall that in the previous section, Billant and Chomaz found experimentally that  $\omega = k^2 \psi$  where  $k = 1.15$ . Here we have that  $\omega_{z0} = \mu_1^2 \psi_0$ . If we consider the dimensional version, we would have that  $k^2 = \mu_1^2 / R^2$  where  $R = 3.6$  cm. This gives  $k^2 = 1.13 \text{ cm}^{-2}$  which corresponds very well with the experimental value of 1.15. Fig. 2.2 is a plot of the vorticity.

Let us now discuss the derivation of this result, which was first written down by Lamb and investigated further, independently, by Chaplygin. Although Lamb was the first to

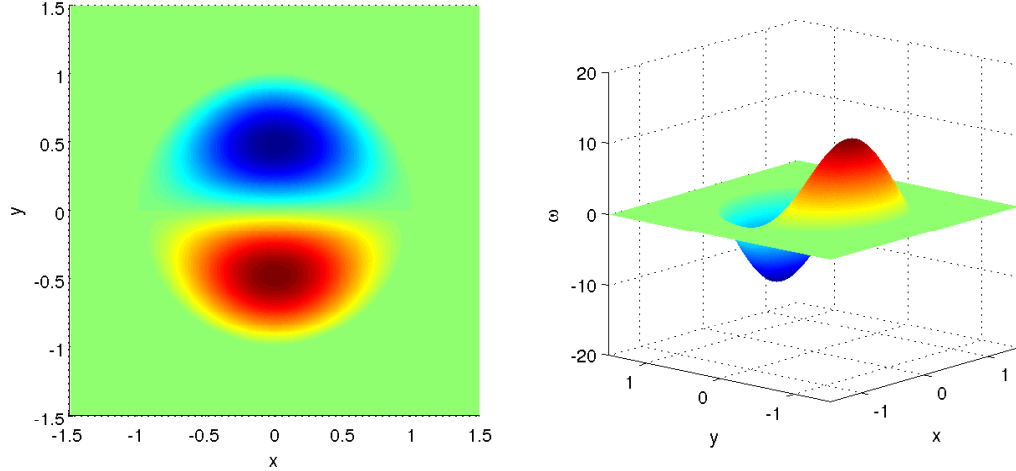


Figure 2.2: The Lamb-Chaplygin dipole.

write down the above solution to the Euler equations, he did not provide any motivation for the derivation beyond it being an exact solution of the 2D steady Euler equations. However, a decade later, Lamb provided a slightly more in depth derivation motivating somewhat the study of this dipole. Independently, in Russia, Chaplygin provided a complete derivation and motivation for studying this dipole, although it remained unknown outside of Russia. Following [35] we repeat the key points of Chaplygin's argument.

Recall that the steady 2D Euler equations can be written in terms of the streamfunction  $\psi$  and a vorticity  $\omega$  as

$$\nabla^2 \psi = -\omega. \quad (2.42)$$

To choose  $\omega$ , Chaplygin was motivated by the situation where we have a continuous vortex whose outer region is steady irrotational flow while the inner region is a translating vortex. Recall that the potential function for a flow outside a cylinder is

$$\psi = v_0 \left( r - \frac{a^2}{r} \right) \sin \theta, \quad (2.43)$$

where  $a$  is the radius of the dipole and  $v_0$  is the propagation velocity.

Inside the radius  $a$ , Chaplygin chose the vorticity to be  $\omega = n^2\psi$  where  $n$  is a constant. In polar coordinates (2.42) becomes

$$\frac{\partial^2\psi}{\partial r^2} + \frac{1}{r}\frac{\partial\psi}{\partial r} + \frac{1}{r^2}\frac{\partial^2\psi}{\partial\theta^2} = n^2\psi \quad (2.44)$$

which we can guess at a solution of the form  $\psi(r, \theta) = Z(r) \sin \theta$ . Although Chaplygin did not provide specific motivation for choosing this specific vorticity, the above equation has a form that is similar to the irrotational flow outside the dipole and this makes the matching conditions simple. The resulting equation for  $Z(r)$  is the well known Bessel equation (cite some book) and after grinding through the algebra, one obtains (2.40). Chaplygin also investigated the resulting pressure field produced by the dipole and was able to compute the circulation of the dipole. Unlike Lamb, he also considered a generalisation of the above where the dipole is no longer symmetric about the x-axis. The corresponding vorticity in this case is given by

$$\omega = n^2(\psi - \lambda) \quad (2.45)$$

where  $\lambda$  is an arbitrary parameter where  $\lambda = 0$  is a completely symmetric dipole and  $\lambda \rightarrow \infty$  corresponds to a completely asymmetric dipole. Here, again, Chaplygin investigated fully the pressure and circulation produced by this dipole. Additionally, in the same set of papers, Chaplygin also investigated the case of the dipole in rotating fluid, which was independently rediscovered 80 years later. Full details of this derivation are in [35] (flierl et. al)

## 2.5 Scaling analysis

We have mentioned two dimensionless numbers in stratified flow, the Reynolds number and the Froude number. Both these dimensionless numbers arise when comparing the relative sizes of various terms in the Navier-Stokes equations. Depending on what aspect of a problem we are looking at, these numbers can appear in different places when we choose different scalings. We will now discuss some of the scaling arguments that have been used in stratified flow as it can provide insights into what mechanisms underlie the transition to and evolution of turbulence. A comprehensive review of scaling in stratified turbulence is provided in a recent review by Riley and Lindborg [46] and we will discuss the important scaling arguments therein.

For reference, we reproduce the Boussinesq equations here

$$\frac{\partial \mathbf{u}'_h}{\partial t'} + \mathbf{u}'_h \cdot \nabla'_h \mathbf{u}'_h + u'_z \frac{\partial \mathbf{u}'_h}{\partial z'} = -\frac{1}{\rho_0} \nabla'_h p' + \nu \nabla'^2 \mathbf{u}_h, \quad (2.46)$$

$$\frac{\partial u'_z}{\partial t'} + \mathbf{u}'_h \cdot \nabla'_h u'_z + u'_z \frac{\partial u'_z}{\partial z'} = -\frac{1}{\rho_0} \frac{\partial p'}{\partial z'} - \frac{\rho' g}{\rho_0} + \nu \nabla'^2 u_z, \quad (2.47)$$

$$\nabla'_h \cdot \mathbf{u}'_h + \frac{\partial u'_z}{\partial z'} = 0, \quad (2.48)$$

$$\frac{\partial \rho'}{\partial t'} + \mathbf{u}'_h \cdot \nabla'_h \rho' + u'_z \frac{\partial \rho'}{\partial z'} + \frac{\partial \rho}{\partial z'} u'_z = D \nabla'^2 \rho', \quad (2.49)$$

where the primed quantities denote the dimensional quantities.

As a starting point, we produce a scaling argument that separates the horizontal and vertical directions. As we saw in the experiment of Billant and Chomaz [7], in the zigzag instability there was a clear separation between the vertical and horizontal scales. This difference in the vertical and horizontal directions suggests defining two length scales, the horizontal length scale  $L_h$  and the vertical length scale  $L_v$ . Associated with this separation we introduce the horizontal velocity scale  $U$  and the vertical velocity scale  $V$ . The resulting scaling is

$$x' = L_h x, \quad y' = L_h y, \quad z' = L_v z, \quad \mathbf{u}'_h = U \mathbf{u}, \quad u'_z = V u_z \quad (2.50)$$

We also define another useful quantity that plays an important role in the scaling of stratified flows, the aspect ratio

$$\delta = \frac{L_v}{L_h}, \quad (2.51)$$

which measures how anisotropic the length scales are. For the time scale, we choose the advective time scale

$$t' = \frac{L_h}{U} t, \quad (2.52)$$

which is the characteristic time of a vortex to be advected around the characteristic length [45, 10, 32]. Following these references the pressure and density scales are

$$p' = \rho_0 U^2 p, \quad \rho' = \frac{U^2 \rho_0}{g L_v} \rho''. \quad (2.53)$$

The only quantity left unspecified is the vertical velocity which can be determined by setting the terms in the density equation to be the same order which yields

$$u'_z = u \frac{F_h^2}{\delta} u_z \quad (2.54)$$

This scaling now leads to the following set of equations [46]

$$\frac{\partial \mathbf{u}_h}{\partial t} + \mathbf{u}_h \cdot \nabla_h \mathbf{u}_h + \frac{F_h^2}{\alpha^2} u_z \frac{\partial \mathbf{u}_h}{\partial z} = -\nabla_h p + \frac{1}{\text{Re}} \left( \nabla_h^2 \mathbf{u}_h + \frac{1}{\alpha^2} \frac{\partial^2 \mathbf{u}_h}{\partial z^2} \right), \quad (2.55)$$

$$F_h^2 \left( \frac{\partial u_z}{\partial t} + \mathbf{u}_h \cdot \nabla_h u_z + \frac{F_h^2}{\alpha^2} u_z \frac{\partial u_z}{\partial z} \right) = -\frac{\partial p}{\partial z} - \rho + \frac{F_h^2}{\text{Re}} \left( \frac{1}{\alpha^2} \frac{\partial u_z}{\partial z^2} + \nabla_h^2 u_z \right) \quad (2.56)$$

$$\nabla_h \cdot \mathbf{u}_h + \frac{F_h^2}{\alpha^2} \frac{\partial u_z}{\partial z} = 0, \quad (2.57)$$

$$\frac{\partial \rho}{\partial t} + \mathbf{u}_h \cdot \nabla_h \rho + \frac{F_h^2}{\alpha^2} u_z \frac{\partial \rho}{\partial z} = u_z + \frac{1}{\text{Re} Sc} \left( \frac{1}{\alpha^2} \frac{\partial^2 \rho}{\partial z^2} + \nabla_h^2 \rho \right) \quad (2.58)$$

where

$$\text{Re} = \frac{U L_h}{\nu}, \quad F_h = \frac{U}{L_h N}, \quad Sc = \frac{\nu}{D} \quad (2.59)$$

Lilly was the first to write these equations down although he assumed istrophy, i.e.  $\delta = 1$ .

Let us now investigate the limit of strong stratification, i.e.  $F_h \rightarrow 0$  but let us leave the behaviour of  $F_h/\delta$  undetermined. Additionally, let us consider  $\text{Re} \gg 1$  so, for the purposes of the scale analysis, ignore them. This results in the following equations

$$\frac{\partial \mathbf{u}_h}{\partial t} + \mathbf{u}_h \cdot \nabla_h \mathbf{u}_h + \frac{F_h^2}{\alpha^2} u_z \frac{\partial \mathbf{u}_h}{\partial z} = -\nabla_h p + \frac{1}{\text{Re}} \frac{1}{\alpha^2} \frac{\partial^2 \mathbf{u}_h}{\partial z^2}, \quad (2.60)$$

$$0 = -\frac{\partial p}{\partial z} - \rho \quad (2.61)$$

$$\nabla_h \cdot \mathbf{u}_h + \frac{F_h^2}{\alpha^2} \frac{\partial u_z}{\partial z} = 0 \quad (2.62)$$

$$\frac{\partial \rho}{\partial t} + \mathbf{u}_h \cdot \nabla_h \rho + \frac{F_h^2}{\alpha^2} u_z \frac{\partial \rho}{\partial z} = u_z + \frac{1}{\text{Re} Sc} \frac{1}{\alpha^2} \frac{\partial^2 \rho}{\partial z^2} \quad (2.63)$$

It was initially assumed by Lilly [32] and Riley et. al [45] that as  $F_h \rightarrow 0$  then so does

$F_h/\delta$ . Thus the resulting equations are

$$\frac{\partial \mathbf{u}_h}{\partial t} + \mathbf{u}_h \cdot \nabla_h \mathbf{u}_h = -\nabla_h p + \frac{1}{\text{Re}} \frac{1}{\alpha^2} \frac{\partial^2 \mathbf{u}_h}{\partial z^2}, \quad (2.64)$$

$$0 = -\frac{\partial p}{\partial z} - \rho \quad (2.65)$$

$$\nabla_h \cdot \mathbf{u}_h = 0 \quad (2.66)$$

$$\frac{\partial \rho}{\partial t} + \mathbf{u}_h \cdot \nabla_h \rho = \frac{1}{\text{Re} Sc} \frac{1}{\alpha^2} \frac{\partial^2 \rho}{\partial z^2} \quad (2.67)$$

These equations have been well known in the atmospheric modelling community. Notice that in these resulting equations, the horizontal and vertical velocities have become almost completely decoupled. They are not completely decoupled because there is still dependence through the pressure term. However this decoupling led Lilly to conjecture that stratified turbulence in the strong stratification limit will obey 2D turbulence [32]. (add link to review of 2D turbulence). 2D turbulence exhibits an inverse energy cascade however this has not been observed in stratified turbulence (cite stuff... add when nonlinear written).

Building on the work of Lilly [32] and Riley et. al. [45], Billant and Chomaz [10] modified the argument suggesting that in the limit of strong stratifications that instead  $F_h/\delta \rightarrow 1$  as  $F_h \rightarrow 1$ . This scaling analysis leads to  $L_v \sim U/N$  which is the result obtained for the zigzag instability.

$$\frac{\partial \mathbf{u}_h}{\partial t} + \mathbf{u}_h \cdot \nabla_h \mathbf{u}_h + u_z \frac{\partial \mathbf{u}_h}{\partial z} = -\nabla_h p + \frac{1}{\text{Re}} \frac{1}{\alpha^2} \frac{\partial^2 \mathbf{u}_h}{\partial z^2}, \quad (2.68)$$

$$0 = -\frac{\partial p}{\partial z} - \rho \quad (2.69)$$

$$\nabla_h \cdot \mathbf{u}_h + \frac{\partial u_z}{\partial z} = 0 \quad (2.70)$$

$$\frac{\partial \rho}{\partial t} + \mathbf{u}_h \cdot \nabla_h \rho + u_z \frac{\partial \rho}{\partial z} = u_z + \frac{1}{\text{Re} Sc} \frac{1}{\alpha^2} \frac{\partial^2 \rho}{\partial z^2} \quad (2.71)$$

The assumption that  $F_h/\delta \rightarrow 1$  can be rewritten to state that  $L_v \sim U/N$ , which is the buoyancy scale. In this case, there is no decoupling between the horizontal and vertical directions.



### **2.5.1 Stratified Turbulence (to be written when nonlinear chapter is written)**

In this final section of background a few results from stratified turbulence that are relevant to the zigzag instability are discussed. A complete discussion of the generation of and full blown stratified turbulence is beyond the scope of this thesis and instead we refer the reader to a recent review of recent theoretical, numerical, and experimental results by Riley and Lindborg.

Discuss some recent results in the nonlinear evolution and turbulence generating of the zigzag instability.

# Chapter 3

## Numerical Background

In this chapter we discuss the numerical techniques and methods used in this thesis. In this thesis we use the spectral method to numerically solve the linear and nonlinear Navier-Stokes equations. Spectral methods provide a convenient and quick way to compute derivatives of sufficiently well-behaved periodic functions. In evaluating derivatives of smooth periodic functions, spectral methods provide an advantage over other methods of evaluating derivatives, such as finite difference, as the derivatives can be computed to with greater accuracy, often to machine precision, in exchange for only a relatively modest increase in complexity. Specifically, finite difference methods run in  $\mathcal{O}(N)$  time, where  $N$  is the number of grid points, but the error tends to be on the order of  $\mathcal{O}(N^{-p})$  where  $p$  is a small integer [22]. Spectral methods, however, run in  $\mathcal{O}(N \log N)$  time but the errors are on the order of  $\mathcal{O}(N^{-p})$  when the function is  $C^p$  [48]. A complete overview of spectral methods is beyond the scope of this thesis and we only discuss the key features needed for numerical work. Comprehensive reviews of spectral methods are provided in many books, e.g. Trefethen [48], Boyd [12], and Canuto [14].

### 3.1 Spectral Methods Motivation

Spectral methods have their origins in the Fourier transform. Let us denote the Fourier transform,  $\mathcal{F}$ , of  $f(x)$  as  $\mathcal{F}(f(x)) = \hat{f}(k)$ , given by

$$\mathcal{F}(f(x)) = \hat{f}(k) = \int_{-\infty}^{\infty} dx e^{-ikx} f(x). \quad (3.1)$$

Now consider the Fourier transform of the derivative  $df/dx$ :

$$\mathcal{F}\left(\frac{df}{dx}\right) = \int_{-\infty}^{\infty} dx e^{-ikx} \frac{df}{dx} = e^{-ikx} f(x) \Big|_{-\infty}^{\infty} + ik \int_{-\infty}^{\infty} dx e^{-ikx} f(x) = ik \hat{f}(k), \quad (3.2)$$

and thus the Fourier transform of a derivative is just  $ik$  times the Fourier transform of  $f(x)$ . An important assumption here that  $f(x)$  vanishes sufficiently quickly at infinity otherwise the  $e^{-ikx} f(x)$  term is non-negligible. For most applications of the Fourier transform, but not all, this assumption is valid. For a complete treatment of the conditions of the existence of the Fourier transform, see e.g. Kammler [26]. With this result in hand, it is easy to show via induction that the Fourier transform of  $d^n f/dx^n$  is  $(ik)^n \hat{f}(k)$ . Hence, once we have the Fourier transform  $\hat{f}(k)$ , the  $n$ -th derivative is obtained by computing the inverse Fourier transform

$$\frac{d^n f}{dx^n} = \frac{1}{2\pi} \int_{-\infty}^{\infty} dx e^{ikx} (ik)^n \hat{f}(k). \quad (3.3)$$

This procedure suggests a method to compute the derivative of a function. Computationally, if we have a way to evaluate  $\hat{f}(k)$  from  $f(x)$  and  $f(x)$  from  $\hat{f}(k)$ , then the  $n$ -th derivative is easy to compute via the following algorithm:

1. Compute  $\hat{f}(k)$  from  $f(x)$
2. Multiply  $\hat{f}(k)$  by  $(ik)^n$
3. Invert  $(ik)^n \hat{f}(k)$  to obtain  $f^{(n)}(x)$

We need a method to evaluate the integrals (3.1) and (3.3). One possible avenue would be to apply well known integral quadratures to evaluate these integrals. However, there are more efficient and better alternatives. The correct avenue to implementing the above algorithm is to consider the discrete analogue of the Fourier transform, the discrete Fourier transform. From the discrete Fourier transform, we discuss the Fast Fourier Transform, which is a fast way to evaluate the discrete Fourier transform.

## 3.2 FFT and Spectral Derivatives

Let us now investigate how we can quickly compute the Fourier transform of a function on a computer. In analogy to the Fourier transform, we define [48] the discrete Fourier

transform<sup>1</sup> (DFT) on  $N$  data points  $v_j$

$$\hat{v}_k = \frac{2\pi}{N} \sum_{j=1}^N e^{-ikx_j} v_j, \quad k = -\frac{N}{2} + 1, \dots, \frac{N}{2}, \quad (3.4)$$

and the inverse discrete Fourier transform (IDFT) on  $N$  data points  $\hat{v}_k$

$$v_j = \frac{1}{2\pi} \sum_{k=-N/2+1}^{N/2} e^{ikx_j} \hat{v}_k, \quad j = 1, \dots, N. \quad (3.5)$$

where  $x_j \in [0, 2\pi]$ . Here we take  $N$  to be even to simplify the formulas, however all results hold for odd  $N$  with slight modification. The range of the wavenumbers is from  $-N/2 + 1$ , not  $-N/2$ , due to the  $2\pi$  periodicity of  $v_j$ . Wavenumbers  $-N/2$  are equivalent to  $N/2$  and we do not want to count this wavenumber twice.

From the definitions of the DFT and inverse DFT, we can see a close analogy to the continuous Fourier and inverse Fourier transforms. It can be shown [48] that these are the correct discrete analogies.

In order to approximate the derivative of a function, we first need to determine how to sample the function  $f(x)$ . We assume  $f(x)$  to be periodic on  $0 \leq x \leq 2\pi$ . If the domain is different, a simple scaling can transform the periodic domain to this standard interval. To compute the derivative of  $f(x)$ , we first sample at the points

$$x_j = \frac{2\pi j}{N}, j = 1, \dots, N \quad (3.6)$$

and set  $v_j = f(x_j)$ . Now we can compute the DFT from  $v_j$  giving the coefficients  $\hat{v}_k$  which is the discrete analogue of  $\hat{f}(k)$ . Since this is the analogue of the Fourier transform, we now multiply by  $ik$  resulting in the analogue of computing the first derivative. Finally, we compute the inverse DFT from  $ik\hat{v}_k$  which produces the spectral approximation,  $v'_j$ , to the derivative of the sampled function  $f'(x)$  at points  $x_j$ . However, there is some subtlety involved in treating the wavenumber  $N/2$ , which is usually set to zero [48].

Despite having a discrete algorithm to compute an analogue of the Fourier transform, our goal has still not been reached because we are still left with doing  $\mathcal{O}(N^2)$  operations. This results because there are  $N$  coefficients and for each coefficient a sum of  $N$  terms must be added together. For small  $N$ , computing spectral derivatives are not that much

---

<sup>1</sup>Note that there is no universal standard on where to put the factors of  $N$  and  $2\pi$ .

slower than finite differences methods, however they quickly become impractical for large  $N$ . This barrier can be overcome through the Fast Fourier Transform (FFT) algorithm. This algorithm has a rich history and has been rediscovered multiple times, beginning with Gauss in the early 1800s before Fourier published his results on Fourier series [26]. The most popular and well known rediscovery of the FFT was in 1965 by Cooley-Tukey [16].

The FFT employs a divide and conquer algorithm. The basic idea is to notice that computing the discrete Fourier transform can be divided into even and odd terms which can be computed independently of each other. Thus assuming  $N$  is a power of two, we have two new discrete Fourier transform problems of size  $N/2$ . Each of those problems can themselves be decomposed into problems of size  $N/4$ . Repeating this process recursively we are able to divide the computation of the DFT into  $\mathcal{O}(\log N)$  problems. Computing the DFT of each problem takes roughly  $\mathcal{O}(N)$  and thus the total running time is on the order of  $\mathcal{O}(N \log N)$ . In this simple case, it is easy to prove rigorously from the recursion relationship that the running time is  $\mathcal{O}(N \log N)$  using the Master theorem [17].

$\mathcal{O}(N \log N)$  is a general result that holds for all values of  $N$ , but the proofs are more complicated and in most applications,  $N$  is chosen to be a power of small primes for which there exist many well optimised and developed algorithms. The derivation and implementation of the FFT for general values of  $N$  is an interesting and complicated question that has sparked a lot of research into the best way to decompose the problem. Additionally, the actual implementation details can differ depending on the value of  $N$ , the type of computer, and the type of data being considered. It is beyond the scope of the thesis to discuss such implementation details and further technical and hardware details that can be used in implementations can be found in [23].

Now that we have an algorithm to compute the FFT, the inverse Fast Fourier Transform (IFFT) can easily be derived since the form of (3.5) is very similar to that of (3.4) and the same strategy of divide and conquer can be applied. With this we have the following algorithm for computing the spectral derivative:

1. Sample function  $f(x)$  at  $N$  data points  $x_j$  to obtain  $v_j, j = 1, \dots, N$ .
2. Compute, using the FFT,  $\hat{v}_k$  from  $v_j$ .
3. Multiply  $\hat{v}_k$  by  $(ik)^n$  to compute the  $n$ -th derivative.
4. Invert  $(ik)^n \hat{v}_k$  using the IFFT to obtain an approximation to  $f^{(n)}(x)$  at  $x_j$ .

To illustrate spectral derivatives, we follow [48] and demonstrate spectral differentiation

using two simple examples. Consider the following two periodic functions

$$f(x) = \max(0, 1 - |x - \pi|/2), \quad g(x) = e^{\sin x} \quad (3.7)$$

which are both periodic on the interval  $[0, 2\pi]$ .

As we can see in Fig. 3.1 when the original function is sufficiently smooth and periodic, here  $g(x)$ , the accuracy of the derivative is very good. However, when the function is not smooth, as exhibited in  $f(x)$ , the accuracy is not very good. Here  $g(x)$  is not differentiable at  $\pi$  and spectral methods have a difficult time dealing with this. For a complete discussion of the specific smoothness and accuracy is contained in Chapter 4 of [48].

In this section, we have focused only on simple one-dimensional examples, but the method easily generalises to arbitrary dimensions. To compute multiple partial derivatives, the only change to the algorithm is that we have separate wavenumbers for the different directions. The only modification is computing the higher dimensional FFTs. To compute the  $n$ -dimensional FFT of a given function, we must compute the FFT of all the columns and all the rows in each dimension [26]. For example in 2D dimensions, we would compute the FFT of each of the columns, and then computing the FFT of all the rows of the previous result [34].

### 3.3 Dealiasing

In the previous section we demonstrated that spectral differentiation can produce very accurate results in only  $\mathcal{O}(N \log N)$  operations. However, we have only considered the spectral derivative of a single function  $f(x)$ . The question naturally arises about what happens if we have products of functions, for example advection like terms in the Navier-Stokes equations

$$u \frac{\partial u}{\partial x} + v \frac{\partial u}{\partial y} + w \frac{\partial u}{\partial z} \quad (3.8)$$

where we now have a product of a function and a derivative. Such terms are known as a convolution and require a more careful treatment. In this section, we introduce two closely related methods for evaluating expressions of the above form, the spectral method and the pseudospectral method. For this we carefully follow the treatment of Durran [22].

Consider the following general 1D non-linear PDE

$$\frac{\partial \psi}{\partial t} + F(\psi) = 0 \quad (3.9)$$

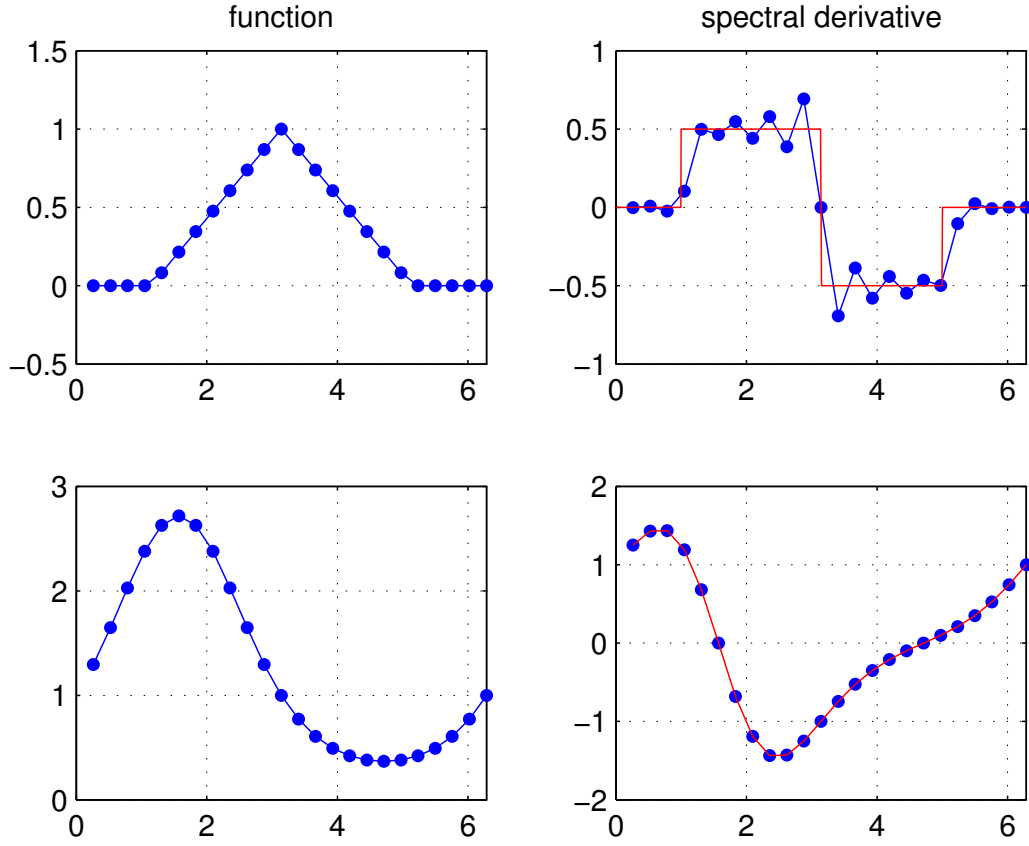


Figure 3.1: Spectral differentiation of two functions  $\max(0, 1 - |x - \pi|/2)$  (top) and  $e^{\sin x}$  (bottom) from [48]. On the right is the spectral derivative computed with  $n = 24$ . Red curve represents the exact derivative. Even as such small  $N$ , the derivative of  $e^{\sin x}$  is very smooth and the error is on the order of  $\mathcal{O}(10^{-13})$ . The spectral derivative of  $\max(0, 1 - |x - \pi|/2)$  is not as good due to the discontinuity at  $x = \pi$ .

where  $F(\psi)$  is some general nonlinear function. Consider seeking a series expansion of the form [22]

$$\psi(x, t) \approx \phi(x, t) = \sum_{k=1}^N a_k(t) \varphi_k(x) \quad (3.10)$$

where  $\varphi_k$  are basis functions around which we are interested in expanding the solution. Some examples of such functions might be complex exponentials, Bessel functions, or spherical harmonics. In general, we will not be able to find the eigenfunctions that provide the natural basis to seek a series expansion. Without the proper basis functions, it is clear that the approximate solution will never exactly solve the original PDE and we have to determine a way to minimise the error. For many problems, there is often some degree of symmetry so choosing a certain basis makes sense. For example, for a problem within a periodic box, it makes sense to choose complex exponentials as a basis; if the problem is based on a sphere, spherical harmonics are a natural choice. Thus, we are interested in not finding the correct  $\varphi_k$  for a given problem but instead focus picking a known basis and appropriately choosing  $a_k(t)$  to minimise the residual [22],

$$R(\phi) = \frac{\partial \phi}{\partial t} + F(\phi), \quad (3.11)$$

in some way.

### 3.3.1 Spectral Method

How we choose to minimise this error leads to different methods of solving the problem. Right now we consider the so-called “spectral method” which is a special case of a very general technique called Galerkin approximation. The spectral method requires the residual be orthogonal to the basis functions  $\varphi_k$ , i.e.

$$\int_S R(\phi(x)) \varphi_k(x) dx = 0 \quad k = 1, \dots, N. \quad (3.12)$$

For the special case of the spectral method, we require that the basis functions be orthogonal. Other basis functions that are not orthogonal but satisfy other constraints, such as support over very small areas, lead to a different approximation known as the finite element method[22]. It can be shown [22] that (3.12) is equivalent to minimising the  $L^2$  error of the residual.



By imposing the above integral, it can be shown[22] that the resulting system of ODEs for the above is

$$\frac{da_k}{dt} = -\frac{1}{M_{k,k}} \int_S \left[ F \left( \sum_{n=1}^N a_n \varphi_n \right) \varphi_k \right] dx \quad k = 1, \dots, N \quad (3.13)$$

where  $M_{k,k} = \langle \varphi_k, \varphi_k \rangle$ . For our work, we are interested in a specific case of basis functions,  $\varphi_k(x) = e^{ikx}$  and the inner product to be the standard inner product for complex functions

$$\int_S g(x) h^*(x) dx = 0 \quad (3.14)$$

To demonstrate the above formulation, we use the spectral method to solve the 1D advection equation with variable windspeed,

$$\frac{\partial \phi}{\partial t} + c(x, t) \frac{\partial \phi}{\partial x} = 0, F(\phi) = c(x, t) \frac{\partial \phi}{\partial x}. \quad (3.15)$$

We now expand out  $\phi(x, t)$  as the sum of  $N = 2K + 1$  Fourier modes, where here we are now letting  $N$  be an odd number in contrast to the previous section where  $N$  was even. This is chosen because it simplifies the formulas, however the results hold for even  $N$  as well, but with some slight alterations to the algebra. Expanding

$$\phi(x_j, t) = \sum_{n=-K}^K a_n(t) e^{inx_j}, \quad (3.16)$$

and plugging this into the above yields

$$\frac{da_k}{dt} = -\frac{i}{2\pi} \sum_{n=-K}^K n a_n \int_{-\pi}^{\pi} c(x, t) e^{i(n-k)x} dx \quad k = -K, \dots, K. \quad (3.17)$$

Expanding out  $c(x, t)$  as a Fourier series we obtain

$$\frac{da_k}{dt} = -\frac{i}{2\pi} \sum_{n=-K}^K \sum_{m=-K}^K n a_n c_m \int_{-\pi}^{\pi} e^{i(n+m-k)x} dx \quad k = -K, \dots, K \quad (3.18)$$

and upon using the orthogonality of the integral, we obtain

$$\frac{da_k}{dt} = - \sum_{\substack{m+n=k \\ |m|, |n| \leq K}} i n c_m a_n \quad (3.19)$$

where we require that  $n+m = k$  and  $|n|, |m| \leq K$ . If we want to evaluate this sum directly, we would need to evaluate  $\mathcal{O}(K^2)$  operations due to the double sum in the convolution. Historically, this was a barrier for spectral methods because even though they provided accurate results, this  $\mathcal{O}(K^2)$  bottleneck did not allow for larger numerical simulations, where  $\mathcal{O}(K)$  finite differences method could [22].

In order to get around this bottleneck, we can turn the  $\mathcal{O}(K^2)$  to  $\mathcal{O}(K \log K)$  using the FFT. The general idea is as follows: transform the Fourier coefficients to real space in  $\mathcal{O}(K \log K)$ , multiply the two terms together at each grid point in  $\mathcal{O}(K)$ , and transform back to Fourier space in  $\mathcal{O}(K \log K)$ . The resulting algorithm is  $\mathcal{O}(K \log K)$ . However, if we were to implement this naively, errors would arise, due to the phenomena of aliasing.

At a basic level, aliasing is the result of multiplying two terms grid-pointwise that generate short waves that can be aliased into long waves. This arises in the spectral method when we compute the product of two Fourier coefficients. A very similar, but exaggerated example, is known as the wagon wheel effect and can illustrate the general idea of short waves being interpreted as long waves [61]. The wagon wheel effect arises when an object appears to be stationary but is really moving. For example, imagine a camera that takes a picture every second of a turbine, but the turbine is moving at 10 revolutions per second. For someone looking at the shots from the camera, they would claim the turbine isn't moving. If the turbine is moving slightly faster, say 10.1 revolutions per second, the camera would show that the turbine is moving, albeit rather slowly. If it were moving slightly slower, say 9.9 revolutions per second, the camera would show the turbine moving backwards. Thus one would interpret the turbine as moving very slowly in either case and thus conclude that it must have a very slow period, or long wavelength. In actuality, the period is much more rapid and the wavelength of one revolution is much shorter.

Mathematically, we can see a similar phenomena by sampling a sine wave. Consider Figure 3.2 which has 11 points. The short wavelength red sine curve samples these points with a short wavelength while a longer wavelength blue curve also samples, despite being non-existent in the actual data. The goal is to minimise this effect.

To illustrate this consider two functions  $f(x), g(x)$ . We want to compute the Fourier coefficients of the product

$$f(x)g(x) = \sum_{m=-K}^K p_k e^{ikx}, \quad (3.20)$$

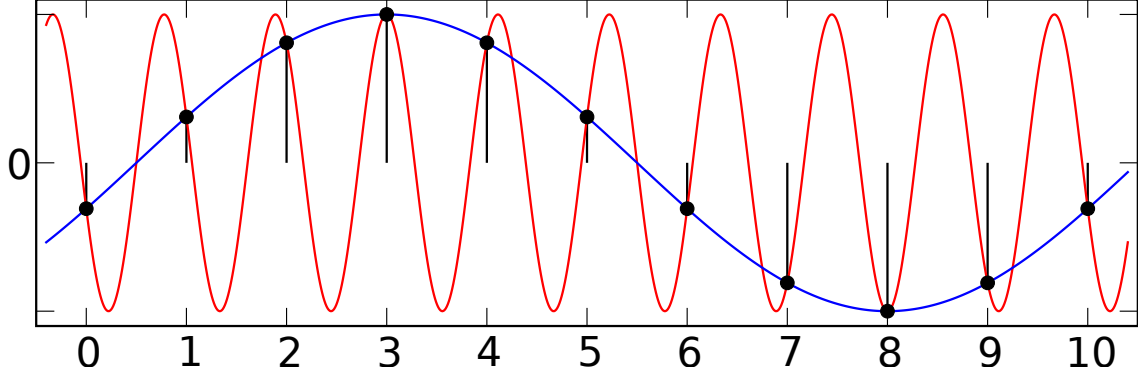


Figure 3.2: Different sine curves that fit the same set of data points [60]. This is an example of aliasing.

and we can expand  $f(x), g(x)$  as Fourier series

$$f(x) = \sum_{m=-K}^K a_m e^{imx}, \quad g(x) = \sum_{n=-K}^K b_n e^{inx}. \quad (3.21)$$

The above algorithm states that we convert the Fourier coefficients  $a_m, b_n$  to real space and multiply. Suppose that in real space the spacing between the grid points is

$$x_j = \frac{2\pi j}{2N+1} \quad (3.22)$$

where we let  $2N+1$  denotes the total number of grid points.

How do we choose  $N$ ? Naively, it seems logical to set that  $N = K$  so that both real and Fourier space have the same number of co-efficients. This naive choice leads to aliasing error and instead we must choose  $N > K$  to avoid this aliasing error. To get intuition for why, aliasing error arises when two poorly resolved waves are multiplied together and produce a longer wavelength wave, as discussed above in Figure 3.2. We can avoid this if all short wavelengths are resolved properly.

To find the optimal value of  $N$ , consider multiplying two functions given by Fourier modes, each with the largest wavenumber  $K$ . This product generates a wave with wavenumber  $2K$ , recalling that multiplication of waves is addition of the wavenumbers. The largest possible resolvable wave in the real space grid is  $\pi/\Delta x = N + 1/2$ . Here we can explicitly

see what happens if  $K = N$ . The  $2K = 2N$  waves would not be resolved properly because the largest possible wavenumber to be resolved is only  $N$ . An obvious choice to fix this is to choose  $N = 2K$  and thus we could resolve all possible wavenumbers. However this choice is too loose a bound since it would imply that for every simulation, we would require twice as many grid space coefficients as Fourier coefficients. It is possible to do better.

To do better, consider which wavenumber the  $2K$  would be aliased into, which will be  $2K - 2\pi/\Delta x$  thus

$$K < |2K - \frac{2\pi}{\Delta x}|, \quad (3.23)$$

and upon subbing in  $\Delta x$  we find that

$$N > \frac{3}{2}K - 1 \quad (3.24)$$

There is an alternative way to get at the same result. Consider the discrete Fourier transform of the product  $f(x)g(x)$

$$p_k = \frac{1}{2N+1} \sum_{j=1}^{2N+1} f(x_j)g(x_j)e^{-ikx_j}, \quad (3.25)$$

and now plug in the

$$f(x) = \sum_{m=-N}^N a_m e^{imx}, \quad g(x) = \sum_{n=-N}^N b_n e^{inx}, \quad (3.26)$$

where we have replaced  $K$  with  $N$  where  $N > K$ . This is the same expansion as before but we have set  $a_l, b_l = 0$  if  $K < |l| \leq N$ . Plugging these into the above yields

$$p_k = \frac{1}{2N+1} \sum_{m=-N}^N \sum_{n=-N}^N \sum_{j=1}^{2N+1} a_m b_n e^{i(m+n-k)x_j}. \quad (3.27)$$

Recalling that  $x_j = 2\pi j/(2N+1)$  the inner summation is

$$\sum_{j=1}^{2N+1} e^{i(m+n-k)x_j} = \begin{cases} 1 & m+n-k=0 \\ 1 & m+n-k=2N+1 \\ 1 & m+n-k=-(2N+1) \\ 0 & \text{otherwise} \end{cases} \quad (3.28)$$

which is a restatement of the well known orthogonality condition [22]. Thus we can break up the above summation into three cases,  $m + n = k, m + n = k \pm (2N + 1)$  which gives

$$p_k = \sum_{\substack{m+n=k \\ |m|, |n| \leq N}} a_m b_n + \sum_{\substack{m+n=k+2N+1 \\ |m|, |n| \leq N}} a_m b_n + \sum_{\substack{m+n=k-2N-1 \\ |m|, |n| \leq N}} a_m b_n. \quad (3.29)$$

Note the similarity with the result from the spectral method, which is identical to summation encountered in the spectral method, recalling that the coefficients are zero for values greater than  $K$ . The aliasing error arises from the second two terms. We want to eliminate this error so we have to decide how to choose  $N$  to eliminate this term. We consider the first aliasing error term. We have that if  $m, n > K$  then  $a_m b_n = 0$ . It follows that  $m + n > 2K$  this term will vanish, i.e.  $m + n = k + 2N + 1 > 2K$  for all  $k = -K, \dots, K$ . Thus we want to consider  $k = -K$  since this is the smallest possible value of this summation, i.e.  $-K + 2N + 1 > 2K$ . Rearranging this yields  $N > (3K - 1)/2$  as before. An identical argument gives the same result for the other aliasing term.

This dealiasing rule is known as the “two-thirds rule” and will completely eliminate aliasing effects. The above algorithm tells us how to choose  $N$  given  $K$ , however in many applications we typically work the other way around, choosing  $N$  and limiting  $K$ . We now can now write down the algorithm for evaluating the following term  $c(x)\partial\phi/\partial x$  in Fourier space, when we are initially only given  $M$  samples:

- Sample  $c(x), \phi(x, t)$  at  $M$  points.
- Compute the Fourier coefficients of  $c(x), \phi(x, t)$  using the FFT yielding  $M$  Fourier coefficients  $a_i, b_j$  respectively.
- Evaluate the spectral derivative of  $\phi$  by multiplying the coefficients by  $ik$ , i.e  $a_l = ik a_l$ .
- Modify the Fourier coefficients so the top  $1/3$  are zero.
- Take the IFFT back to real space.
- Multiply the real space coefficients gridwise.
- Take the FFT of this product.

This procedure will allow us to evaluate the Navier-Stokes equations in Fourier space by evaluating convolution terms by multiplying fields in real space and to eliminate numerical error. In the next section, we provide a simple example that illustrates this method in practice.

### 3.3.2 Pseudospectral Method

We have so far been focusing on eliminating the aliasing error at the cost of eliminating some Fourier modes which can be achieved by taking  $N > 3K/2$ . A closely related method known as the pseudospectral method is an alternative way to evaluate the above equations. In this case, instead of enforcing that the residual is orthogonal to the basis functions, we instead choose a collocation method [22], i.e.

$$R(\phi(j\Delta x)) = 0, \quad (3.30)$$

where we enforce that the coefficients satisfying the equation at each grid point. Let us now expand  $\phi(x, t), c(x, t)$  are Fourier series

$$\phi(x, t) = \sum_{n=-K}^K a_n e^{inx}, \quad c(x, t) = \sum_{m=-K}^K c_m e^{imx}. \quad (3.31)$$

Substituting into the test equation and enforcing the collocation requirement yields

$$\sum_{n=-K}^K \frac{da_n}{dt} e^{inx_j} + \sum_{m=-K}^K c_m e^{imx_j} \sum_{n=-K}^K i n a_n e^{inx_j} = 0. \quad (3.32)$$

which we can alternatively write as

$$\frac{d\phi_j}{dt} + c_j \frac{\partial \phi_j}{\partial x} = 0, \quad (3.33)$$

where we have written

$$\phi(x_j) = \sum_{n=-K}^K a_n e^{inx_j}, \quad c(x_j) = \sum_{n=-K}^K c_n e^{inx_j}, \quad \frac{\partial \phi_j}{\partial x} = \sum_{n=-K}^K i n a_n e^{inx_j}. \quad (3.34)$$

This is the set of equations we want to solve. Thus we now have a way to evaluate using the following algorithm:

1. Evaluate  $\phi(x, t), c(x, t)$  at  $M$  points.
2. Compute the spectral derivative of  $\phi(x, t)$  using the methods of the previous sections.
3. Multiply all the coefficients gridpoint wise.
4. Timestep the resulting solution.

### 3.3.3 Spectral vs Psuedospectral

The equations resulting from the pseudospectral method are actually very similar to the spectral equations except that there is no dealiasing. To see why, multiply the above equation by  $e^{-ikx_j}$  and sum over all  $j$  and we will obtain

$$\frac{da_k}{dt} = - \sum_{\substack{m+n=k \\ |m|, |n| \leq K}} inc_m a_n - \sum_{\substack{m+n=k+2K+1 \\ |m|, |n| \leq K}} inc_m a_n - \sum_{\substack{m+n=k-2K-1 \\ |m|, |n| \leq K}} inc_m a_n. \quad (3.35)$$

For comparison, the spectral method equations are

$$\frac{da_k}{dt} = - \sum_{\substack{m+n=k \\ |m|, |n| \leq K}} inc_m a_n, \quad (3.36)$$

where in both equations  $k = -K, \dots, K$ .

There are many similarities between these two equations but we have to remember that they were derived in two completely different ways. Recall that to evaluate the convolution term in the spectral method, we obtained the following equation

$$p_k = \sum_{\substack{m+n=k \\ |m|, |n| \leq N}} a_m b_n + \sum_{\substack{m+n=k+2N+1 \\ |m|, |n| \leq N}} a_m b_n + \sum_{\substack{m+n=k-2N-1 \\ |m|, |n| \leq N}} a_m b_n. \quad (3.37)$$

which has the exact same form as the pseudospectral method but the crucial difference is that the sum is over  $N$  and not  $K$ . If we set  $N = K$ , which would result in dealiasing error, we would obtain the pseudospectral method. Thus, at a fundamental level, the pseudospectral method is just the spectral method without dealiasing.

## 3.4 Timestepping and Examples

Recall that our model 1D problem is

$$\frac{\partial \psi}{\partial t} + F(\psi) = 0. \quad (3.38)$$

We have been focusing on evaluating the  $F(\psi)$  term but now we turn to the time derivative term. Fortunately, this term is much simpler to deal with than the nonlinear terms since it appears only as a single derivative.

To evaluate this term, consider the approximation to the first derivative [22]

$$\frac{\partial \psi}{\partial t} \approx \frac{\psi^{n+1} - \psi^n}{\Delta t}. \quad (3.39)$$

Here the subscript now denote the solution  $\psi$  evaluated at  $n$ th timestep. Now that the time derivative is handled, at what timestep do we evaluate the  $F(\psi)$  term? We could evaluate it at  $\psi_n$  or  $\psi_{n+1}$  or maybe other possible previous times. Let us consider evaluating at  $\psi_n$ . Now plugging everything in we obtain the following scheme, known as the forward Euler scheme [22]

$$\psi_{n+1} = \psi_n - \Delta t F(\psi_n). \quad (3.40)$$

Here the right hand side is a function solely of  $\psi_n$ . When scheme can be written as a function of all previous terms, the scheme is known as explicit. However, we could have chosen to evaluate  $\psi$  at  $\psi_{n+1}$  and we would obtain the backward Euler scheme [22]

$$\psi_{n+1} = \psi_n - \Delta t F(\psi_{n+1}). \quad (3.41)$$

Here, if  $F(\psi)$  is nonlinear function, we cannot isolate for  $\psi_{n+1}$ . Instead we would have to use some sort of root finding solver to find the correct  $\psi_{n+1}$  given  $\psi_n$ . Schemes that exhibit this property are known as implicity schemes. Depending on the problem at hand, one scheme may be better than the other. For this thesis, we uses Adams-Bashforth 2nd and 3rd order, follwing previous work [9, 56].

Once we have choosen a time-stepping scheme, the stability of the scheme is important to know. If we pick  $\Delta t$  too large, for example, the right handside might grow too large and become unstable. By finding the stability region of a scheme, it tells us when we can except our solution to not blow up. To investigate this we define the amplitude  $A$  to be

$$A = \frac{\psi_{n+1}}{\psi_n}, \quad (3.42)$$

and stability is defined to be

$$|A|^2 \leq 1, \quad (3.43)$$

since  $A$  can potentially be complex. The reasoning from this equation arises from rearranging the above so that  $\phi_{n+1} = A\phi_n$ . If  $|A| \leq 1$  then the solution is not growing in time. If  $|A| > 1$  then at each time-step the solution is being multiplied by a number greater then



one, hence it is growing. To illustrate, we use the second order Adams-Bashforth scheme [22]

$$\psi_{n+1} = \psi_n + \frac{\Delta t}{2}(3F(\psi_n) - F(\psi_{n-1})). \quad (3.44)$$

Clearly the growth rate of a scheme will depend on the given function  $F(\psi)$ . However the standard procedure is to investigate the following model problem [22]

$$\frac{d\psi}{dt} = (\lambda + i\omega)\psi. \quad (3.45)$$

where  $\lambda, \omega$  are real numbers.

To determine the stability region we use the method from Leveque [29] which gives a stability region of

$$z = \frac{2(\xi^2 - \xi)}{3\xi - 1} \quad (3.46)$$

where  $\xi$  is the unit circle. Fig. 3.3 illustrates the stability region of the Adams-Bashforth second order.

To illustrate time-stepping schemes and how they are applied to problems, consider the following one dimensional advection equation[48]

$$\frac{\partial u}{\partial t} + c(x)\frac{\partial u}{\partial x} = 0, \quad c(x) = \frac{1}{5} + \sin^2(x - 1), \quad u(x, 0) = e^{-100(x-1)^2}, x \in [0, 2\pi], t > 0 \quad (3.47)$$

where we are solving on a periodic domain. The physical interpretation of this equation is the simple one dimensional advection of a velocity field  $u(x, t)$  by the fixed field  $c(x)$ . To evaluate the advection term, we use a spectral method with 2/3s dealiasing. As discussed in the previous section, there is still non-standard terminology throughout the literature regarding the names of the various methods of using FFTs. Trefethen, for example, calls pseudospectral methods, ‘collocation methods’[48] which is also a term used by Durran [22], although Durran prefers the term pseudospectral.

For a time-stepping scheme, we use a second-order Adams-Bashforth[22] scheme. Rewriting wave-equation as

$$\frac{\partial u}{\partial t} = -c(x)\frac{\partial u}{\partial x} = F(u) \quad (3.48)$$

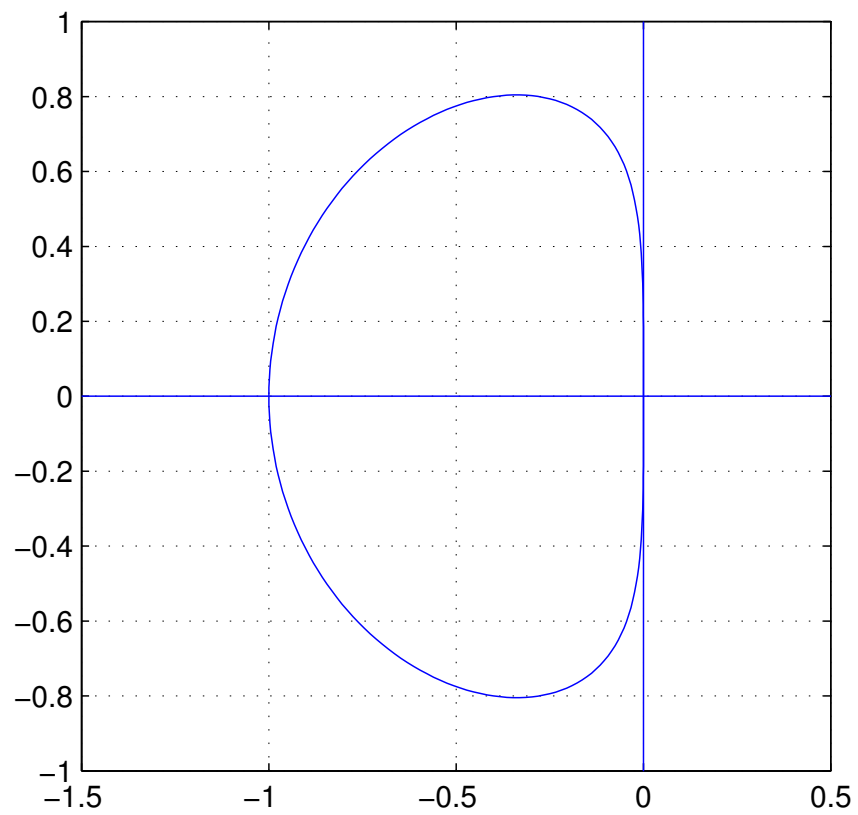


Figure 3.3: Stability region of Adams-Bashforth second order. Adapted from [\[48\]](#)

which we can write in Fourier space as

$$\frac{\partial \hat{u}}{\partial t} = -\widehat{c(x) \frac{\partial u}{\partial x}} = F(\hat{u}) \quad (3.49)$$

the Adams-Bashforth scheme is

$$\hat{u}^{n+1} = \hat{u}^n + \frac{\Delta t}{2} [3F(\hat{u}^n) - F(\hat{u}^{n-1})] \quad (3.50)$$

Since the Adams-Bashforth scheme uses a previous time-step, we will use forward Euler for the first time-step. To evaluate  $F(u)$  we will use the spectral differentiation, as discussed above. See Appendix A for the sample MATLAB code which illustrates how to achieve dealiasing in practice.

Fig. 3.4 demonstrates the solution to the above advection equation using spectral methods. As can be observed, the solution is very smooth and evolves very clearly for only  $N = 128$ .

In the previous section we discussed spectral and pseudospectral schemes. To illustrate the differences between the two, we solve the viscous Burgers equation using both spectral and pseudospectral methods [22]

$$\frac{\partial \psi}{\partial t} + \psi \frac{\partial \psi}{\partial x} = \nu \frac{\partial^2 \psi}{\partial x^2}. \quad (3.51)$$

The initial condition used was a Gaussian. To handle the time-stepping, we use an Adams-Bashforth second order as discussed above. Fig. 3.5 illustrates the results of the numerical experiment. Initially, both the spectral and pseudospectral codes have similar energy wise but after around 1 time unit, the pseudospectral is dissipating energy faster than the spectral code. However, the key difference is that at around  $T = 3.6$  the pseudospectral code diverges due to aliasing error. The spectral code, which does dealias, does not experience this divergence and continues to decay due to viscous effects. Indeed, it can be shown [22] that for inviscid problems, the spectral method will conserve energy. This example illustrates the importance and necessity of dealiasing.

## 3.5 Navier-Stokes in Fourier Space

### 3.5.1 Fourier Transformed Navier-Stokes

We now turn to the formulation of the Navier-Stokes equations in the Fourier domain which provides a convenient formulation to analyse the underlying mechanisms of turbulence. Recall that in the Fourier domain, derivatives become multiplication of wavenumbers

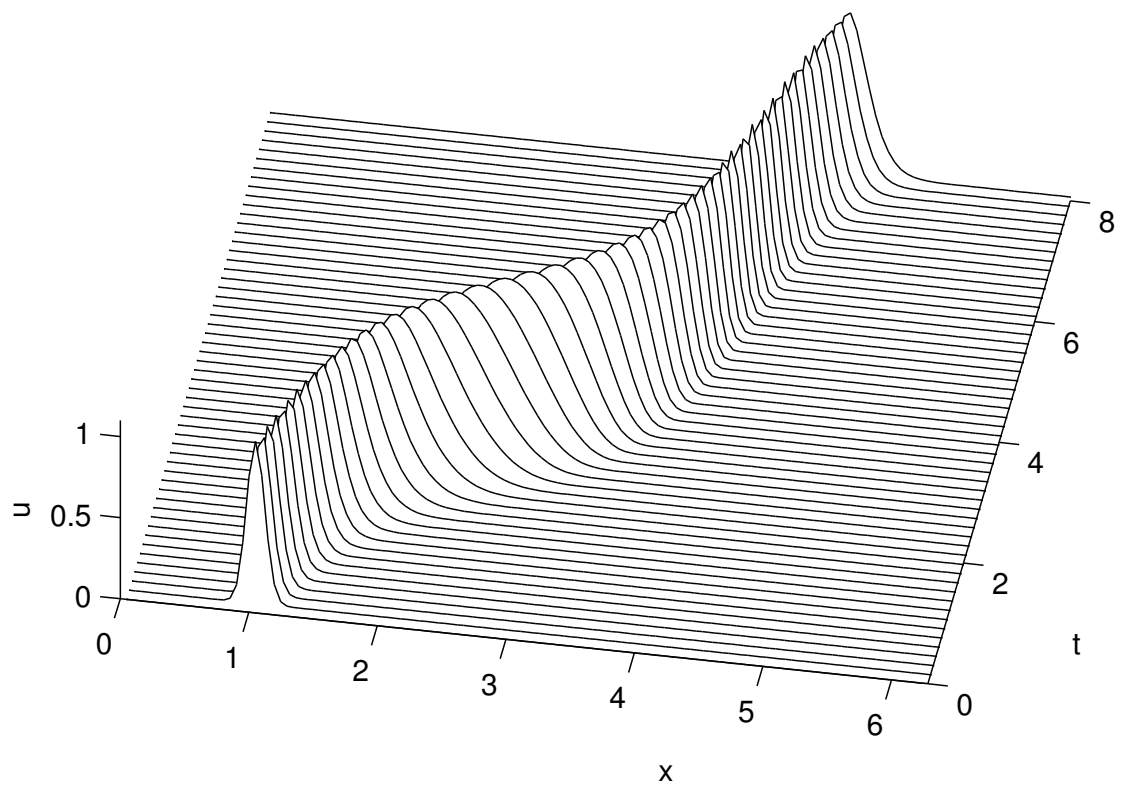


Figure 3.4: Spectral solution to the advection equation with variable windspeed. Figure is a reproduced version of Output 6 of Trefethen [48]

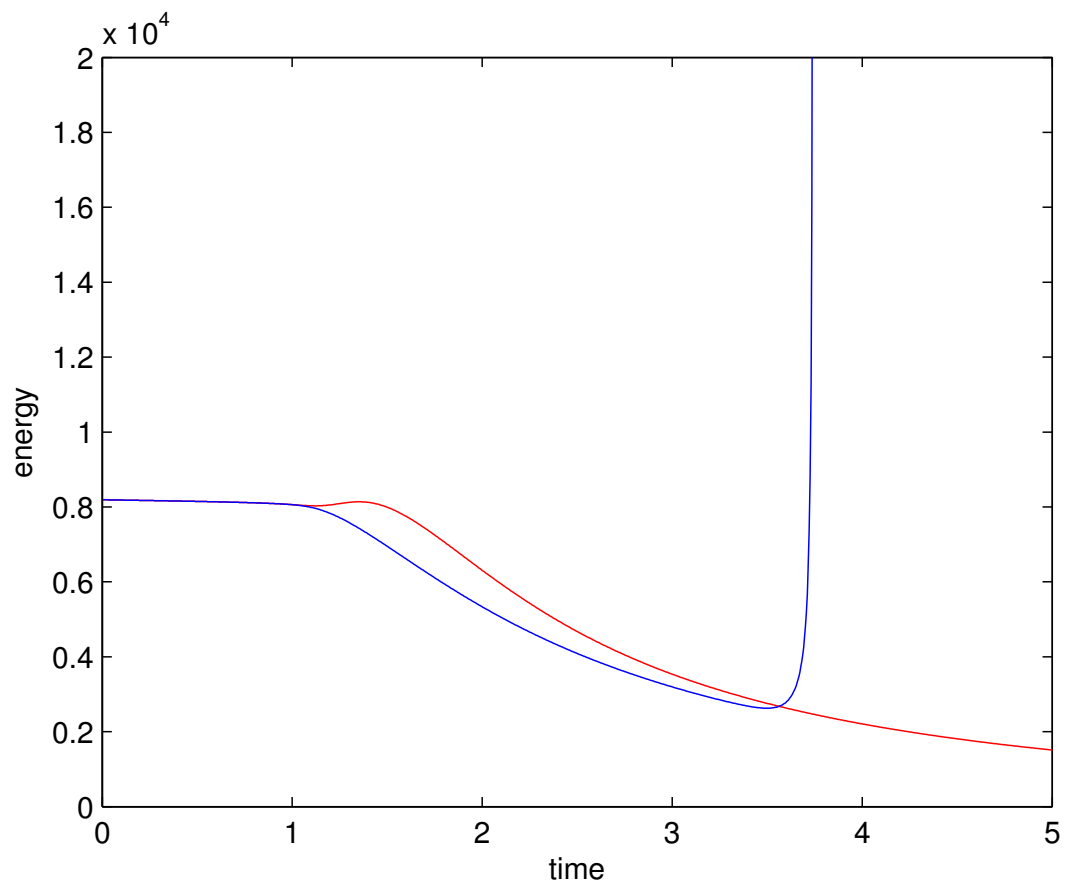


Figure 3.5: Solution to the viscous Burgers equation using spectral (red) and pseudospectral (blue).

which converts the spatial parts of the Navier-Stokes equations into algebraic equations. To demonstrate the formulation in Fourier space, let us cast the standard Navier-Stokes equations into Fourier space.

$$\frac{\partial \mathbf{u}}{\partial t} + \mathbf{u} \cdot \nabla \mathbf{u} = -\frac{1}{\rho_0} \nabla p + \nu \nabla^2 \mathbf{u}, \quad \nabla \cdot \mathbf{u} = 0 \quad (3.52)$$

Taking the Fourier transform of the above equation is straight-forward for all terms except the advection term  $\mathbf{u} \cdot \nabla \mathbf{u}$ , which we postpone for now.

In Fourier space, we can also exploit the following observation to eliminate the pressure term. The incompressibility condition becomes  $\mathbf{k} \cdot \hat{\mathbf{u}}(\mathbf{k}, t) = 0$  in Fourier space. Geometrically, this means that the vectors  $\mathbf{k}$  and  $\hat{\mathbf{u}}$  are orthogonal. This realisation tells us that vectors that are proportional to  $\hat{\mathbf{u}}$  are orthogonal to vectors that are proportional to  $\mathbf{k}$ . Thus writing out the Navier-Stokes equations

$$\frac{\partial \hat{\mathbf{u}}}{\partial t} + \mathcal{F}(\mathbf{u} \cdot \nabla \mathbf{u}) = -\frac{1}{\rho_0} \mathbf{k} \hat{p} - \nu k^2 \hat{\mathbf{u}}, \quad (3.53)$$

take the dot product with  $\mathbf{k}$  and using the orthogonality condition we obtain

$$\mathbf{k} \cdot \mathcal{F}(\mathbf{u} \cdot \nabla \mathbf{u}) + \frac{1}{\rho_0} k^2 \hat{p} = 0. \quad (3.54)$$

Isolating for pressure and substituting back into (3.53) we obtain

$$\frac{\partial \hat{\mathbf{u}}}{\partial t} + \mathcal{F}(\mathbf{u} \cdot \nabla \mathbf{u}) \left( \mathbf{1} - \frac{\mathbf{k} \mathbf{k}}{k^2} \right) = -\nu k^2 \hat{\mathbf{u}}. \quad (3.55)$$

This result is unsurprising, since all we have done is take the divergence of the Navier-Stokes equations, which in Fourier space corresponds to taking the dot product with respect to  $\mathbf{k}$ . But using this observation we can avoid the need for solving the pressure altogether because the pressure term is orthogonal to the  $\hat{\mathbf{u}}$ -plane. But what about the advection term? As can be seen in (3.55), it has this factor  $\mathbf{1} - \mathbf{k} \mathbf{k} / k^2$  multiplying it. This term represents a projection into the  $\hat{\mathbf{u}}$ -plane. The advection term can be thought of as a vector that is pointing in some direction in-between the planes of  $\mathbf{k}$  and  $\hat{\mathbf{u}}$ . By projecting the advection term into the  $\hat{\mathbf{u}}$ -plane, we would have a set of equations that are independent of the pressure completely.

### 3.5.2 Projection Tensor

In order to project the Navier-Stokes equations onto the  $\hat{\mathbf{u}}$ -plane, we define the following projection operator

$$\mathbf{P} = \mathbf{1} - \frac{\mathbf{k}\mathbf{k}}{k^2} \text{ or } P_{ij}(\mathbf{k}) = \delta_{ij} - \frac{k_i k_j}{k^2} \quad (3.56)$$

where we are using Einstein summation notation [28, 57]. It is straightforward to verify that  $P_{ij}P_{jk} = P_{ik}$  or in matrix notation  $\mathbf{P}^2 = \mathbf{P}$ , in other words the projection tensor is idempotent. Idempotence is a defining feature of projection operators [36]. It is straightforward to verify that  $k_j P_{ij} = 0$  and  $\hat{u}_j P_{ij} = \hat{u}_i$ . These simple observations confirm that the projection tensor projects a vector onto the  $\hat{\mathbf{u}}$ -plane.

Applying  $P_{ij}$  to (3.53) we obtain the following

$$\frac{\partial \hat{\mathbf{u}}}{\partial t} + \mathbf{P} \mathcal{F}(\mathbf{u} \cdot \nabla \mathbf{u}) = -\nu k^2 \hat{\mathbf{u}} \quad (3.57)$$

where  $\mathbf{P}$  is acting on the Fourier transform of the advection term. In order to compute the Fourier transform of the advection term, we note that

$$\mathbf{u} \cdot \nabla \mathbf{u} = u_j \frac{\partial u_i}{\partial x_j} = \frac{\partial (u_i u_j)}{\partial x_j} \quad (3.58)$$

where the incompressibility condition has been used to bring the velocity inside the derivative. Thus we are able to write

$$\mathcal{F}(\mathbf{u} \cdot \nabla \mathbf{u}) = ik_j \int_{\mathbf{p}+\mathbf{q}=\mathbf{k}} d\mathbf{k} \hat{u}_i(\mathbf{p}) \hat{u}_j(\mathbf{q}) \quad (3.59)$$

and hence we can finally write out the Navier-Stokes equations in Fourier space as [28]

$$\frac{\partial \hat{u}_i}{\partial t} + iP_{ij}k_m \int_{\mathbf{p}+\mathbf{q}=\mathbf{k}} d\mathbf{k} \hat{u}_j(\mathbf{p}) \hat{u}_m(\mathbf{q}) = -k^2 \hat{u}_i \quad (3.60)$$

### 3.5.3 Numerical Formulation of NS in Fourier

Although we have eliminated the pressure completely, we still have the nonlinear term in the equation. To formulate this problem numerically, we make the following observation that is useful in spectral methods [28, 41].

Recall the following identity [27, 1]

$$\mathbf{u} \cdot \nabla \mathbf{u} = \boldsymbol{\omega} \times \mathbf{u} - \frac{1}{2} \nabla \mathbf{u}^2 \quad (3.61)$$

When we apply the projection operator  $\mathbf{P}$  to the above equation, the  $\nabla \mathbf{u}^2$  term will vanish since it is orthogonal to the  $\hat{\mathbf{u}}$ -plane. For the cross product between the vorticity and velocity, we use the methods discussed above from dealiasing. Thus to evaluate the cross product term, we assume we have the Fourier transform of the vorticity and velocity  $\hat{\boldsymbol{\omega}}, \hat{\mathbf{u}}$  and re-write the cross product term as

$$\mathcal{F}(\boldsymbol{\omega} \times \mathbf{u}) = \mathcal{F}(\mathcal{F}^{-1}(\hat{\boldsymbol{\omega}}) \times \mathcal{F}^{-1}(\hat{\mathbf{u}})) \quad (3.62)$$

Using this result we can reformulate the Navier-Stokes equations into a form to be solved numerically using a spectral method

$$\frac{\partial \hat{\mathbf{u}}}{\partial t} = \mathbf{P}(\mathbf{k}) \mathcal{F}(\mathcal{F}^{-1}(\hat{\boldsymbol{\omega}}) \times \mathcal{F}^{-1}(\hat{\mathbf{u}})) - k^2 \hat{\mathbf{u}} \quad (3.63)$$

where the  $\mathcal{F}, \mathcal{F}^{-1}$  can be evaluated by FFTs, as discussed above.

This reformulation of the Navier-Stokes equations into Fourier space simplifies numerical calculations immensely and provides many advantages over the real space formulation. The absence of the pressure term means that there is no Poisson equation to be solved at each time-step for the pressure. If one did want the pressure, one can solve (3.54) for  $\hat{p}$ . In addition there is no need to enforce a divergence free solution<sup>2</sup> as the equations are formulated by definition to satisfy divergence free condition. The only additional technical difficulty is evaluating the vorticity, but this can easily be handled because of the simple structure of the curl.

The above has been focused on the Navier-Stokes equations and not the Boussinesq equations, however the extension to these equations is straightforward. The only additional complexities are an additional equation which can be solved analogously to the momentum equation [28].

### 3.5.4 Integrating Factor

Another advantage of the Fourier formulation is the ability to exactly integrate the diffusion term. Let us denote the advective projective term as  $F(\hat{\mathbf{u}})$  and we have

$$\frac{\partial \hat{\mathbf{u}}}{\partial t} + \nu k^2 \hat{\mathbf{u}} = F(\hat{\mathbf{u}}) \quad (3.64)$$

---

<sup>2</sup>Except possibly at the initial time step and periodically during a simulation due to numerical errors.



where the left-hand side has been explicitly written out. Written in this form, the common trick of writing a product as a derivative is observed since

$$\frac{\partial \hat{\mathbf{u}}}{\partial t} + \nu k^2 \hat{\mathbf{u}} = e^{-\nu k^2 t} \frac{\partial}{\partial t} (\hat{\mathbf{u}} e^{\nu k^2 t}) \quad (3.65)$$

Thus we can re-write the Navier-Stokes equations as

$$\frac{\partial}{\partial t} (\hat{\mathbf{u}} e^{\nu k^2 t}) = e^{\nu k^2 t} F(\hat{\mathbf{u}}) \quad (3.66)$$

For notational convenience, let us write  $g(t) = e^{\nu k^2 t}$  and note the following trivial identities

$$g(t \pm \Delta t) = g(t)g(\pm \Delta t), \quad g(0) = 1, \quad g(t)^{-1} = g(-t). \quad (3.67)$$

With this notation the Navier-Stokes equations become

$$\frac{\partial(\hat{\mathbf{u}}g(t))}{\partial t} = g(t)F(\hat{\mathbf{u}}). \quad (3.68)$$

Now let us solve the above system using an Adams-Bashforth 2nd order time-stepping scheme. Initially we obtain

$$\hat{\mathbf{u}}^{n+1}g(t_n + \Delta t) = \hat{\mathbf{u}}^n g(t_n) + \frac{3}{2}\Delta t g(t_n)F(\hat{\mathbf{u}}^n) - \frac{1}{2}\Delta t g(t_{n-1})F(\hat{\mathbf{u}}^{n-1}). \quad (3.69)$$

Using the identities in (3.67) the scheme reduces to

$$\hat{\mathbf{u}}^{n+1} = g(-\Delta t)\hat{\mathbf{u}}^n + \frac{3}{2}\Delta t g(-\Delta t)F(\hat{\mathbf{u}}^n) - \frac{1}{2}\Delta t g(-2\Delta t)F(\hat{\mathbf{u}}^{n-1}), \quad (3.70)$$

and the diffusion term has been reduced to a multiplication by a constant factor  $g(-\alpha\Delta t)$ .

### 3.5.5 Hyperviscosity

Hyperviscosity is a method of simulating higher Reynolds number flow by replacing the diffusion term with higher derivatives. In the Fourier picture, the diffusion term is  $-\nu k^2 \hat{\mathbf{u}}$ . The diffusion timescale  $\tau_d$  is given by the inverse of  $\nu k^2$ . This implies that the longest wavelengths (smallest  $k$ ) have very long diffusive time-scales while the shortest wavelengths (larger  $k$ ) have very short diffusive time-scales. This picture makes physical sense since viscosity plays the most important role at the very small scales. As we decrease the

viscosity  $\nu$  the time-scales of all scales increases. Numerically, if we decrease the viscosity too much, resolution of the smallest scales becomes critical and can lead to unwanted grid-scale effects. Thus, in order to decrease the diffusive time-scales of all wavelengths we can instead vary the power of the wave number. For example, going from  $k^2$  to  $k^4$ , and adjusting the coefficient accordingly, the time-scales of the various wavelengths would decrease. This is illustrated in Fig 3.6.

REPLACE THIS PARAGRAPH WITH EXAMPLES FROM LITERATURE

In order to incorporate hyperviscosity numerically, we scale the coefficient by the maximum wavenumber  $k_{max}$ . We want the diffusive timescales of the smallest scales to be the same for both the regular viscosity and the hyperviscosity. That is we want

$$\nu k_{max}^2 = \nu_i k_{max}^i, \quad (3.71)$$

where  $i$  is an even integer. Solving for  $\nu_i$  then gives the following replacement

$$\nu k^2 \Rightarrow \nu k_{max}^{2-i} k^i. \quad (3.72)$$

Throughout this thesis, we will use  $i = 4$ .

### 3.5.6 Concluding Remarks

Although we have done all our manipulations in Fourier space, we could have equally well formulated the above equations in real space. The idea of projecting the velocity field onto the  $\hat{\mathbf{u}}$ -plane is motivated by the Helmholtz decomposition. This decomposition states, for any  $C^2$  vector field in a bounded region of  $\mathbb{R}^3$ , we can decompose the vector field into a divergence-free and curl-free component. The divergence free part corresponds to taking the divergence of the Navier-Stokes equations which would yield the Poisson equation for the pressure. Taking the curl of the Navier-Stokes equation - which we define to be the vorticity - would yield the vorticity equation which does not have a pressure term.

## 3.6 Numerical Scheme for Linear and Nonlinear Boussinesq Equations

### 3.6.1 Linear Boussinesq Equations Scheme

We now write the fields as a basic state, denoted by a subscript 0, plus perturbations, denoted by  $\sim$ . Ignoring the viscous diffusion of the basic state [21] and neglecting products

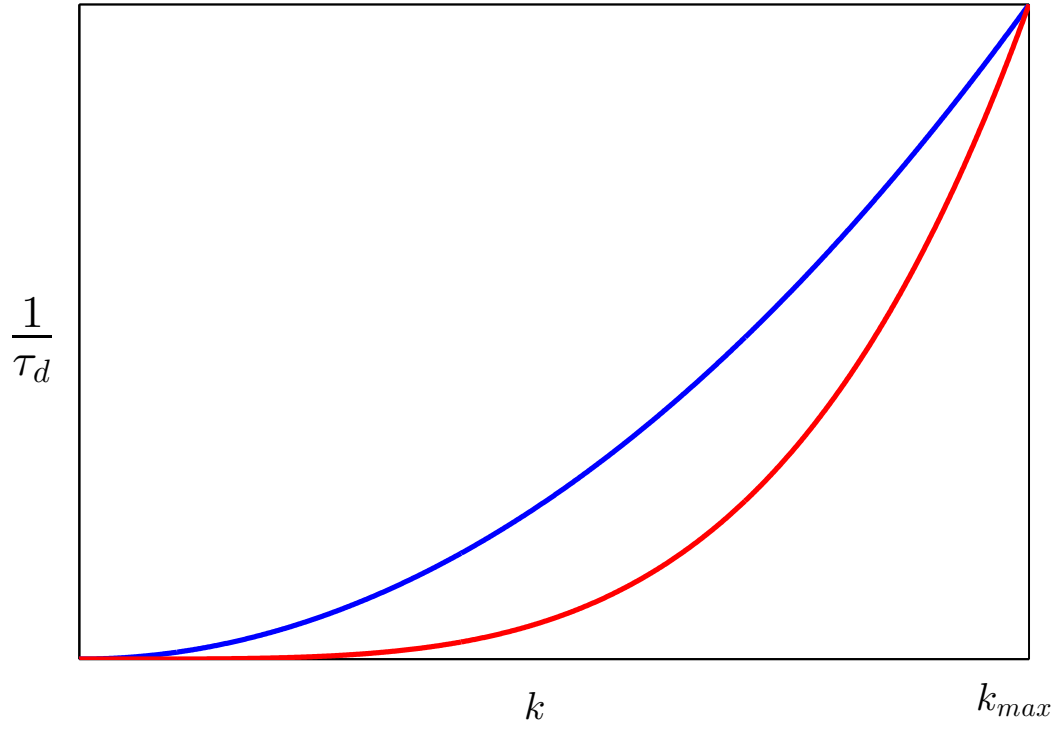


Figure 3.6: The inverse diffusion times,  $1/\tau_d$ , of the wavenumbers for the regular viscosity, blue, and the hyperviscosity case, red. The hyperviscosity inverse diffusion times are lower than the regular viscosity case, corresponding to longer diffusion times. This has the effect of simulating larger Reynolds numbers. Note that at  $k_{max}$  the two cases coincide.

of the perturbations, we obtain the following set of linear equations for the perturbations

$$\frac{\partial \tilde{\mathbf{u}}}{\partial t} + \omega_{z0} \hat{\mathbf{e}}_z \times \tilde{\mathbf{u}} + \tilde{\boldsymbol{\omega}} \times \mathbf{u}_{h0} = -\nabla(\tilde{p} + \mathbf{u}_{h0} \cdot \tilde{\mathbf{u}}) - \tilde{\rho}' \hat{\mathbf{e}}_z + \frac{1}{Re} \nabla^2 \tilde{\mathbf{u}}, \quad (3.73)$$

$$\nabla \cdot \tilde{\mathbf{u}} = 0, \quad (3.74)$$

$$\frac{\partial \tilde{\rho}'}{\partial t} + \mathbf{u}_{h0} \cdot \nabla_h \tilde{\rho}' - \frac{1}{F_h^2} \tilde{w} = \frac{1}{ScRe} \nabla^2 \tilde{\rho}', \quad (3.75)$$

where  $\tilde{\boldsymbol{\omega}} = \nabla \times \tilde{\mathbf{u}}$ . To test how much the basic state diffuses, we used the full nonlinear code, which will be discussed below, with the same Lamb-Chaplygin dipole initial state, and let it diffuse out. We found that over 50 time units, the basic state only diffused by about 10%, and hence we are justified in ignoring the viscous diffusion of the basic state.

As stated above, the Lamb-Chaplygin dipole is oriented vertically. As a result we can separate the perturbation into the vertical and horizontal directions as

$$[\tilde{\mathbf{u}}, \tilde{p}, \tilde{\rho}'](x, y, z, t) = [\mathbf{u}, p, \rho'](x, y, t) e^{ik_z z} + \text{c.c.}, \quad (3.76)$$

where c.c. is the complex conjugate. From here we can now take the 2D Fourier transform and recall the projection operator  $\mathbf{P}(\mathbf{k})$ , with components  $P_{ij}(\mathbf{k}) = \delta_{ij} - k_i k_j / k^2$  to eliminate pressure, to obtain a set of equations for the Fourier coefficients

$$\frac{\partial \hat{\mathbf{u}}}{\partial t} = \mathbf{P}(\mathbf{k}) [\widehat{\mathbf{u} \times \omega_{z0} \hat{\mathbf{e}}_z} + \widehat{\mathbf{u}_{h0} \times \boldsymbol{\omega}} - \hat{\rho}' \hat{\mathbf{e}}_z] - \frac{k^2}{Re} \hat{\mathbf{u}}, \quad (3.77)$$

$$\frac{\partial \hat{\rho}'}{\partial t} = -i \mathbf{k}_h \cdot \widehat{\mathbf{u}_{h0} \rho'} + \frac{1}{F_h^2} \hat{w} - \frac{k^2}{ScRe} \hat{\rho}', \quad (3.78)$$

where  $k_z, Re, Sc, F_h$  are input parameters,  $\mathbf{k}_h = (k_x, k_y)$  is the horizontal wavenumber and  $k^2 = k_x^2 + k_y^2 + k_z^2$  is the total wavenumber.

To numerically solve (4.1) and (3.78), we use a spectral transform method to evaluate derivatives, with 2/3-rule de-aliasing and second order Adams-Bashforth for time-stepping. Each simulation was initialised with a random field and integrated over an  $N \times N$  grid for 100 time units to determine the behaviour of the fastest growing mode. After several time units, the leading eigenmodes for  $\mathbf{u}, \rho$  behave exponentially (e.g. Billant and Chomaz [9])

$$\mathbf{u}, \rho \propto C(x, y) e^{\sigma t}, \quad (3.79)$$

and we can obtain the largest growth rate by the formula

$$\sigma = \lim_{t \rightarrow \infty} \frac{1}{2} \frac{d \ln E}{dt}, \quad (3.80)$$

where  $\sigma$  is the real growth rate of the mode and  $E$  is the kinetic energy  $\frac{1}{2}(u^2 + v^2 + w^2)$ . This follows directly from the exponential behaviour of the leading eigenmode. The energy behaves as

$$E \sim \frac{3}{2}C(x, y)^2 e^{2\sigma t} \Rightarrow \ln E = \ln(3C^2/2) + 2\sigma t \quad (3.81)$$

and upon taking the time derivative of both sides yields the desired result. To obtain the energy, we use Parseval's theorem which relates the real space energy to the sum of the squares of the Fourier coefficients. Thus the total kinetic energy is obtained by summing the squares of the Fourier transform of the velocities over all wavenumbers.

To evaluate  $\sigma$ , we compute the average value of the growth rate from the time series. Initially, there is transient behaviour where the various modes are all growing and none dominant. After  $t = 20$ , after the initial transient behaviour has died out and the leading mode dominates in all the cases observed. In the case of an oscillatory growth rate, as considered in [6], we drop the assumption that  $\sigma$  is real and instead compute the growth rate from

$$\sigma_r = \lim_{t \rightarrow \infty} \frac{1}{2T} \ln \left( \frac{E(t+T)}{E(t)} \right), \quad (3.82)$$

where  $T$  is the period of the oscillatory mode. The imaginary growth rate is given as  $\sigma_i = 2\pi/T$ . As above, we compute  $\sigma$  from the time series beginning at  $t = 20$ , however we first measure the period  $T$  from roughly 10 oscillations, and then compute the average.

### 3.6.2 Nonlinear Boussinesq Scheme

We now turn to the problem of numerically solving the nonlinear Boussinesq equations. Discuss KE transfer + describe how the code works.

# Chapter 4

## Linear Theory

### 4.1 Introduction

In this chapter we extend the results of Billant and Chomaz [9] to the sub-buoyancy length-scales. We also reproduce the numerical results presented by Billant and Chomaz and confirm their conclusions about the existence of the zigzag instability at the buoyancy scale. The results in this chapter are based on the paper by Bovard and Waite [11].

### 4.2 Set-up

The equations that we want to solve are the linear Boussinesq equations, which we derived in Chapter 2 and for which we derived the numerical scheme in Chapter 3. We repeat the equations here:

$$\frac{\partial \hat{\mathbf{u}}}{\partial t} = \mathbf{P}(\mathbf{k})[\widehat{\mathbf{u} \times \omega_{z0} \hat{\mathbf{e}}_z} + \widehat{\mathbf{u}_{h0} \times \boldsymbol{\omega}} - \hat{\rho}' \hat{\mathbf{e}}_z] - \frac{k^2}{Re} \hat{\mathbf{u}}, \quad (4.1)$$

$$\frac{\partial \hat{\rho}'}{\partial t} = -i \mathbf{k}_h \cdot \widehat{\mathbf{u}_{h0} \rho'} + \frac{1}{F_h^2} \hat{w} - \frac{k^2}{ScRe} \hat{\rho}'. \quad (4.2)$$

The parameter regime to be explored is a function of  $k_z, Re, F_h$ .

In our simulations, we investigate a range of Reynolds numbers  $Re = 5000 - 20,000$  and Froude numbers  $F_h = 0.05 - 0.2$ . These numbers have been chosen to be within the range of the results of Billant and Chomaz [9], who investigated a similar range. This

range also falls within potential experimental regimes which could be investigated using the techniques of Billant and Chomaz [7]. For each  $F_h$  and  $Re$  a wide range of vertical wavenumber,  $k_z$ , were investigated with  $k_z$  ranging from 1 to 200. This wavenumber range incorporates the scale of the zigzag instability down to the viscous damping scale. We additionally consider the Schmidt number to be unity, following the main results of Billant and Chomaz [9]. In order to compare with experiments, Billant and Chomaz did investigate a non-zero Schmidt number, however their numerical work was dedicated to  $Sc = 1$  and thus we do not consider different Schmidt numbers here.

For our simulations a box size of  $L = 9$  with  $N = 512$  grid points was used. The reason for choosing  $L = 9$  was to minimise interactions of the fields with themselves across the periodic boundary. As discussed previously, a box size as small as  $L = 5$  could be used safely although  $L = 4$  has been used in practice (cite), however we erred on the side of caution and repeated the box size conditions of Billant and Chomaz [9]. We used the timesteps of  $\Delta t = 0.000950$  for  $F_h = 0.2$ ,  $Re = 2000, 5000, 10000$  and  $\Delta t = 0.000375$  for all the other simulations. These were chosen following Billant and Chomaz [9].

The code was written in Fortran and all the FFTs were done by FFTW V3.0[23] and was tested by comparing the growth rates given by Billant and Chomaz in [9], specifically their Figure 1 and Tables 1 and 2. Unlike Billant and Chomaz [9] we did not restart each simulation with the previous eigenmode because we used a parallel approach for evaluating multiple  $k_z$  simultaneously. The trade-off is the individual simulations had to be run longer but they could be done in parallel allowing for a greater variability in the parameters explored.

## 4.3 Growth Rate

As discussed in Chapter 3, the growth rates are computed by evaluating the time derivative of the energy of the eigenmode. Fig. 4.1 demonstrates two different types of growth rates that are representative of all the growth rate plots for all the simulations. Here we have chosen  $F_h = 0.1$ ,  $Re = 20,000$  and  $k_z = 20$  in panel a and  $k_z = 60$  in panel b. In both panels, the perturbation initially goes through some transient behaviour which is when the various eigenmodes all grow together and none of have become dominant. After about 20 time units this transient behaviour has died off the dominant eigenmode has emerged. This 20 time unit delay was observed for all simulations. In panel (a), there is a case of an oscillatory growth rate. As can be observed, the growth rate of this wavenumber is highly oscillatory and thus the true value of the growth rate must be computed using the

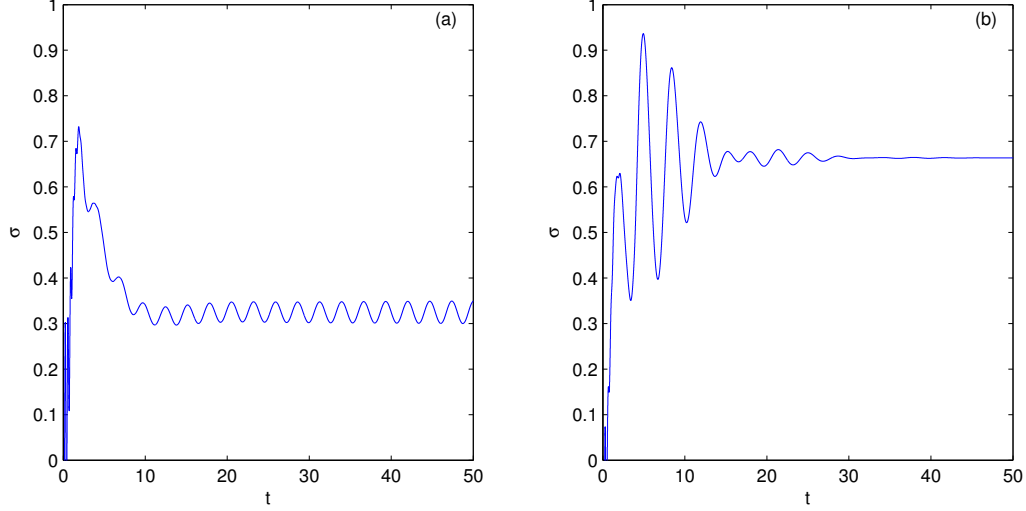


Figure 4.1: Time series of the growth rate, obtained from the derivative of the energy, for  $F_h = 0.1$  and  $Re = 10,000$ . Panel (a) is  $k_z = 20$  and Panel (b) is  $k_z = 60$ .

period of the oscillatory. Panel (b) represents the more typical case of the growth being non-oscillatory and quickly settling down onto a certain value.

Using these types of plots of the growth rate, we are able to extract the leading growth rate of the maximum eigenmode by examining the long term behaviour. From these times series, we determined the maximum growth rate of the leading eigenmode for a wide range of wavenumbers, Reynolds numbers, and Froude numbers. The growth rate curves for a given  $F_h$  and  $Re$  can be plotted by determining this maximum growth rate for each vertical wavenumber. Following Billant and Chomaz[9], we scale the vertical wavenumber by  $F_h$  to obtain a horizontal scaling  $k_z F_h$ . This is, in our units, scaling by the buoyancy scale  $L_b = U/N$ . Recall that  $k_z$  has been non-dimensionalised by  $R$  so the dimensionless  $F_h k_z$  would become  $F_h k'_z R$  in dimensional units,  $k'_z$  denoting the dimensional vertical wavenumber. Re-writing this we obtain  $F_h k'_z R = k'_z U/N = k'_z L_b$ , using the definition of the Froude number, and hence dimensional  $F_h k'_z R = k'_z L_b$  but since  $R = 1$ ,  $k'_z$  and  $k_z$  have the same value, but with different units, scaling dimensionless  $F_h k_z$  is like scaling by the buoyancy length.

Fig. 4.2 shows the largest eigenmode growth rate as a function of vertical wavenumber for fixed  $F_h$  and  $Re$  for a wide range of  $F_h$  and  $Re$ . The qualitative behaviour for the growth



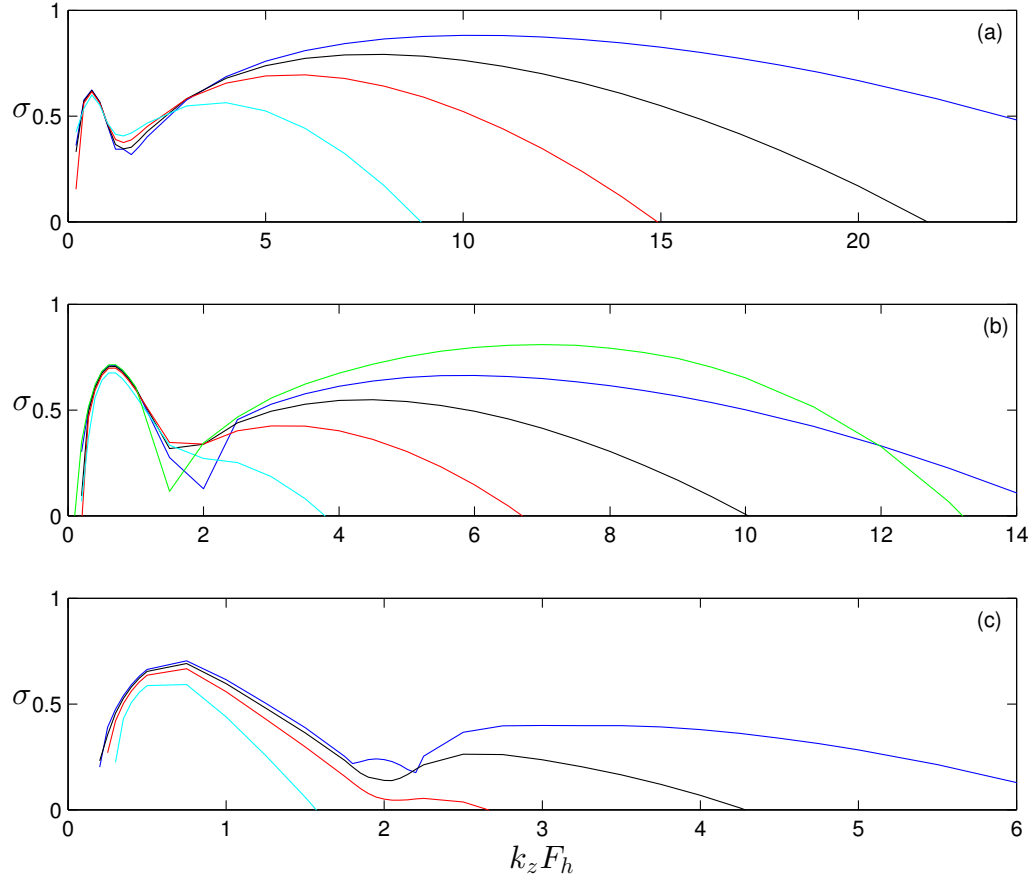


Figure 4.2: Growth rate  $\sigma$  as a function of  $k_z F_h$  for fixed  $F_h$  =(a) 0.2, (b) 0.1, (c) 0.05 with  $Re= 2000$  (cyan),  $Re= 5000$  (red),  $Re= 10000$  (black),  $Re= 20,000$  (blue). In panel (b) the green line is the hyperviscosity case with  $Re = 20,000$ .

rates at different Reynolds numbers are very similar to one another. We now investigate the various regimes in some detail.

At small  $F_h k_z$ , the growth rate reaches a local maximum, the zigzag peak, as predicted by Billant and Chomaz [7, 8, 9]. As discussed in Chapter 2 the zigzag instability appears at the buoyancy wavelength  $L_b$ . This is clear from the figure where we can see that peak growth rate occurs at the same  $F_h k_z$ , here roughly  $F_h k_z \approx 0.6$ . In panels (a) and (b) it is especially clear that the growth rate curves all collapse onto each other and have almost identical growth rates regardless of Reynolds number, confirming the results of the prediction of Billant and Chomaz [8, 9]. Panel (c) has similar growth rates for  $Re = 20,000, 10,000$ , and  $5000$  but for  $Re = 2000$  the growth rate is a bit lower. Despite the slight difference in growth rates, they do all occur at the same  $k_z F_h$ . The  $Re = 2000$  case being lower suggests that the diffusion effects are beginning to dominate, as can be seen by the rapid decrease in the growth rate of the curve. Since the theoretical results of Billant and Chomaz [8] were conducted in an inviscid regime, it is not unexpected to observe a breakdown of this assumption. Some numerical experiments were run at even lower Froude number, but here the diffusion was dominating and the growth rate curves were dropping off very rapidly near the zigzag peak and thus even obscuring the zigzag peak. Thus for  $F_h < 0.05$  and  $Re < 10,000$  we find that the sub-buoyancy length scales are being diffused out.

For  $k_z$  increasing beyond the zigzag peak, the growth rate then decreases for increasing  $F_h k_z$  to a local minimum before increasing to a second local maximum. At this local minimum oscillatory growth rates are observed. The imaginary part of the growth rate  $\sigma_i$  remains zero everywhere else except in this small region between the two local maximum, with the exception of very small  $k_z F_h$ . Oscillatory growth rates are also observed in this small regime, as observed in [6] and have been observed before [6] (add in ref 31 of BC1999) and we did not explore this regime. Fig. 4.3 displays the imaginary growth rates for  $F_h = 0.05$  and  $Re = 10,000, 20,000$ . The imaginary growth rate for  $Re = 10000$  is a straight line but such a trend is not observed for  $Re = 20,000$ . The shape of this curve, when it did appear, depended highly on the Reynold and Froude number, and did not suggest any sort of general result that could be determined about the imaginary growth rate. Additionally, the range of this oscillatory instability also depended on the Froude and Reynolds number and also did not suggest any sort of general result. Due to these observations, we did not explore this regime too closely.

After this local minimum, the growth rate increases to a secondary maximum. We will discuss it further below. Continuing to even smaller vertical scales, viscous effects increase and may damp out the instability, and hence the growth rate decays with increasing  $k_z F_h$  in the limit of large  $k_z F_h$ .

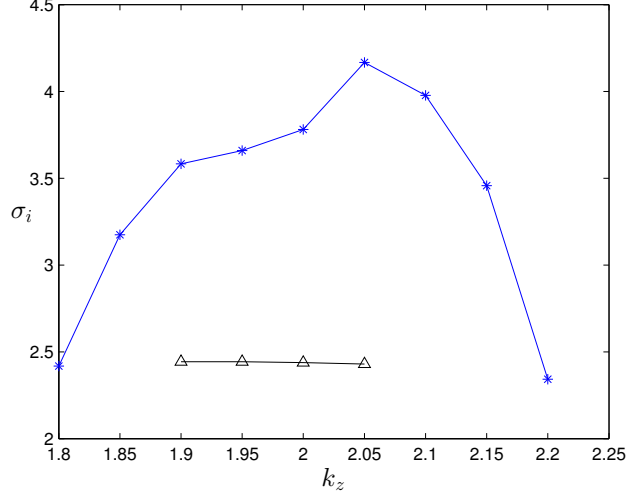


Figure 4.3: Imaginary part of the growth rate for  $F_h = 0.05$  and  $Re = 20,000$  (blue) and  $Re = 10,000$  (black).

For  $F_h = 0.2$  (Fig. 4.2a), the peak growth rate of the short-wave instability exceeds that of the zigzag instability for increasing Reynolds numbers. The growth rates at the second peak is smaller for  $F_h = 0.1$  (Fig. 4.2b), but they continue to increase with increasing  $Re$ . For  $F_h = 0.05$  (Fig. 4.2c), the second peak is weaker than the zigzag peak. Fig. 4.4 shows the growth rate for fixed Reynolds numbers with varying Froude numbers. Examining the case of  $Re = 20,000$  (Fig. 4.4a), the growth rate at the second peak increases with increasing Froude. A similar result is observed for  $Re = 10000$  and  $5000$  (Fig. 4.4b-c).  $Re = 2000$  is not included because viscous effects have damped out the second peak in this case. Overall, the dependence of the short-wave growth rate on Froude is also more pronounced than that of Reynolds. For example, the growth rate of the second peak at fixed  $Re = 20,000$  (Fig. 4.4a) doubles from  $F_h = 0.05$  to  $F_h = 0.2$ . By contrast, at fixed  $F_h = 0.2$  (Fig. 4.2a), the increase in the growth rate from  $Re = 5000$  to  $Re = 20,000$  is only about 25% larger.

The above analysis demonstrates that the short-wave growth-rate peak moves to larger  $k_z F_h$  with increasing  $F_h$  and increasing  $Re$ , but has a stronger dependence on Froude than Reynolds. Some of this joint dependence can be explained by examining the dependence on the buoyancy Reynolds number  $Re_b = F_h^2 Re$  [44, 24, 13]. In stratified turbulence, the buoyancy Reynolds number is analogous to the Reynolds number in the viscous term due

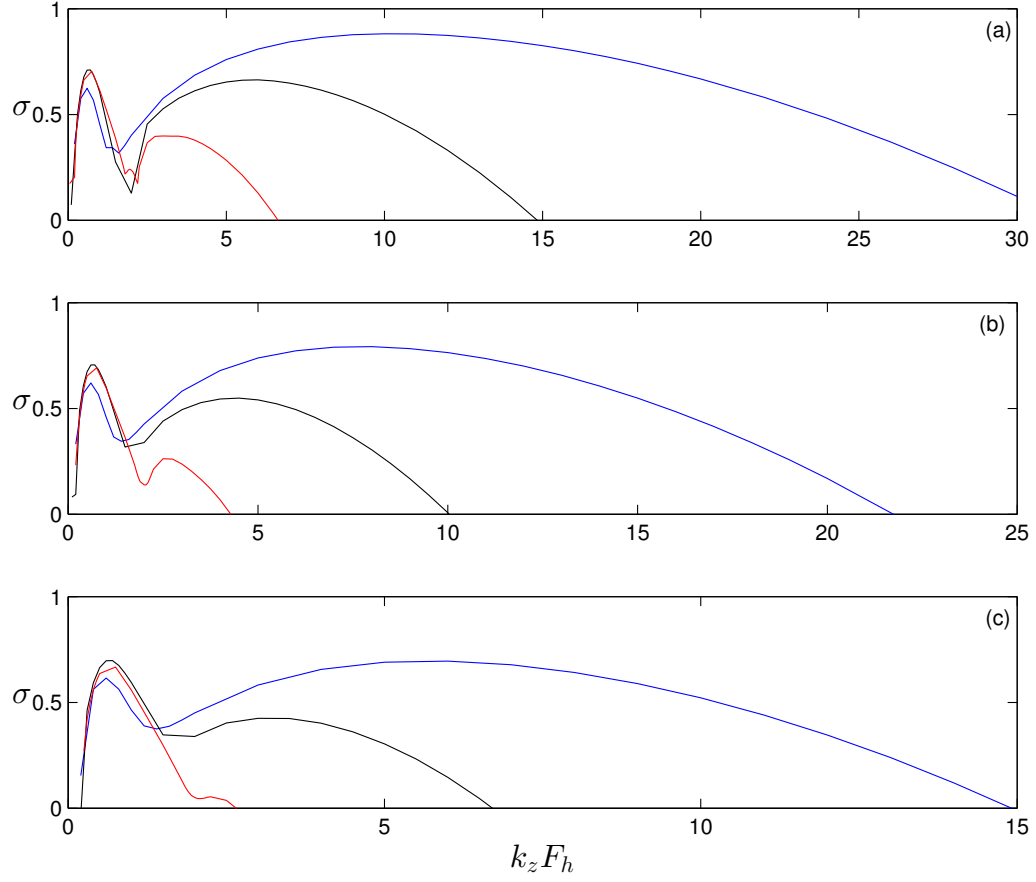


Figure 4.4: Growth rate  $\sigma$  as a function of  $k_z F_h$  for fixed  $Re = (a)20,000, (b)10000, (c)5000$  with  $F_h = 0.05$  (red),  $F_h = 0.1$  (black),  $F_h = 0.2$  (blue).

to the vertical gradients [13]. As  $k_z$  increases, we move to smaller vertical scales where the vertical viscosity terms, controlled by the buoyancy Reynolds number, dominates, so it follows that the second peak may be governed by  $Re_b$ . In Fig. 4.5 the location of the second peak from Fig. 4.2 is plotted as a function of the buoyancy Reynolds number. The peak location line is approximately linear and can be fitted with the curve  $k_z F_h = Re_b^{2/5}$ , which is plotted. This scaling implies that the vertical wavenumber,  $k_z$ , of the short-wave instability is approximately

$$k_z \sim F_h^{-1/5} Re^{2/5}. \quad (4.3)$$

The dependence of the growth rate on  $k_z F_h$  appears to be similar in the cases with different  $F_h$  and  $Re$  but the same  $Re_b$ . Fig. 4.6 demonstrates the similarity of the growth rate plotted against  $k_z F_h$  for two cases with  $Re_b = 500$  and two cases with  $Re_b = 50$ . For both cases, the locations of the zigzag and second peak line up quite well. The difference between the red and blue curves at the second peak is 4% for  $Re_b = 200$  and 6% for  $Re_b = 50$ , a reasonable variation.

In Fig. 4.2 (b) the green curve corresponds to a hyperviscosity run with  $Re = 20,000$ , which has  $Re_h = 2.8 \times 10^8$ . The motivation for using hyperviscosity is to capture the higher-Reynolds number regime by restricting dissipation to only the largest wavenumbers. As the hyperviscosity run demonstrates, the zigzag peak is independent of Reynolds number and the existence of the peak would be expected at higher Reynolds numbers. For the second peak, we note that the growth rate of the hyperviscosity run exceeds that of  $Re = 20,000$  for  $k_z F_h > 3$  and reaches a maximum around  $k_z F_h = 7$ . The maximum growth rate in the hyperviscosity case is around 25% larger than the regular viscosity case with  $Re = 20,000$ . At  $k_z F_h = 12$  we see the hyperviscosity and non-hyperviscosity curves cross. This intersection corresponds to the horizontal wavenumber at which the hyperviscosity damping rate equals the regular viscous damping rate for  $Re = 20,000$ . For  $k_z$  greater than this maximum, the hyperviscosity operator experiences greater damping than the regular viscosity, which can be seen by the sudden drop off of the growth rate. This simulation presents evidence that as  $Re \rightarrow \infty$ , the growth rate of the second peak will be the same order as, or larger than, the growth rate of the zigzag instability.

## 4.4 Structure

Briefly, we discuss the structure of the zigzag instability. Fig. 4.7 demonstrates the vertical vorticity of the zigzag peak for  $F_h = 0.2, 0.1, 0.05$  and  $Re = 20,000$ . In all vertical vorticity plots that follow, we have normalised the plots so red represents the maximum velocity or

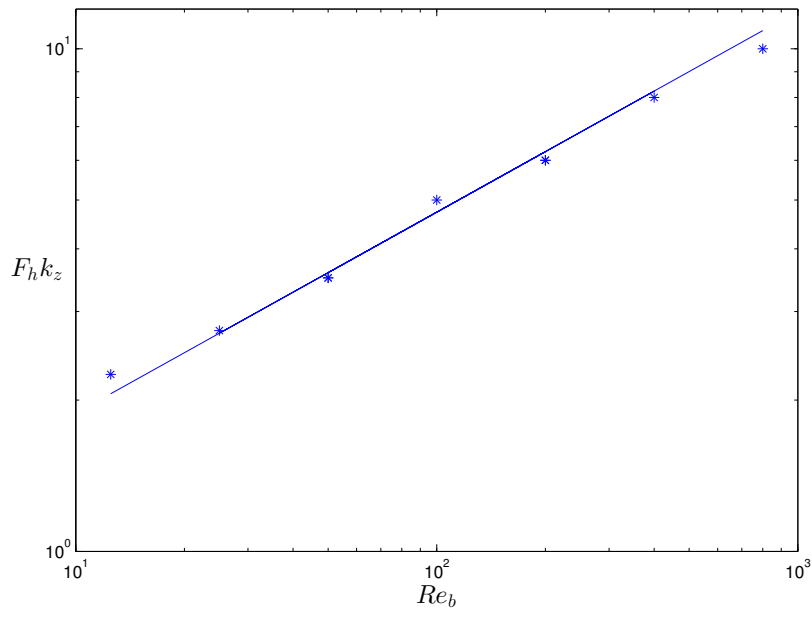


Figure 4.5: The location of the second peak as a function of the buoyancy Reynolds number  $Re_b$ .  $k_z F_h$  is taken from Fig. 4.2. The straight line is  $Re_b^{2/5}$ .

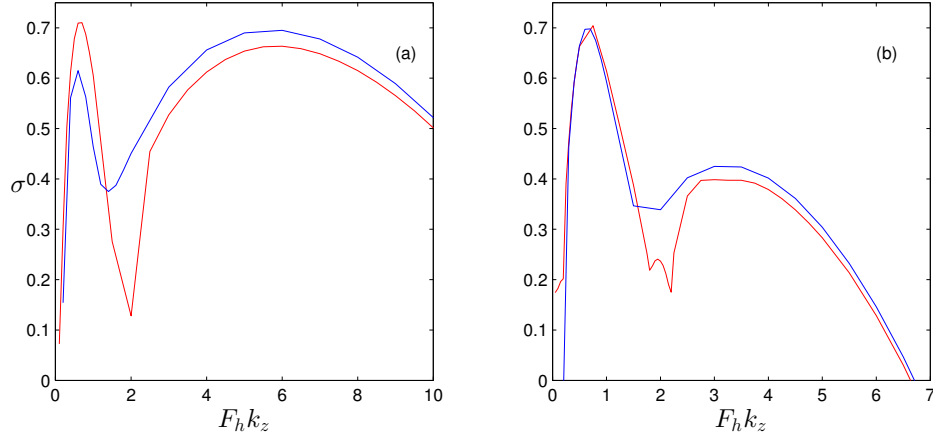


Figure 4.6: Growth rate  $\sigma$  as a function of  $F_h k_z$  for fixed  $Re_b$ . In (a), red is  $Re = 20,000, F_h = 0.1$  and blue is  $Re = 5000, F_h = 0.2$ , both corresponding to  $Re_b = 500$ ; in (b) red is  $Re = 20,000, F_h = 0.05$  and blue is  $Re = 5000, F_h = 0.1$ , both corresponding to  $Re_b = 50$ .

vorticity and blue represents the minimum velocity or vorticity. Since the vorticity field is real, we have chosen the real part. Only  $Re = 20,000$  has been included, see Fig. 4.8, since the structure is nearly identical for  $Re = 10,000$  and  $5000$ . This confirms the assumption made by Billant and Chomaz [8] that the zigzag peak emerges at the buoyancy scale  $U/N$  independent of  $Re$ . A detailed study of the structure of the zigzag instability is done by Billant and Chomaz [9].

The minimum between the zigzag and short-wave instability is the oscillatory minimum. Fig. 4.9 and Fig. 4.10 are the vorticity and velocity fields respectively. In the vorticity structure, for  $Re = 20,000$  the structure is much more defined than the smoothed out structure of the zigzag instability. At the largest Froude number, the vorticity is in thin strips around the dipole. At the middle Froude number (b),(e),(h) the core of the dipole, new structure has emerged has a swirl-like pattern. At the smallest Froude number (c),(f),(i), this structure has become much more detailed and a swirl-like pattern has clearly emerged. Additionally, as we increase the viscosity, this swirl-like structure becomes more diffused out.

Fig. 4.11 and Fig. 4.12 show the spatial structure of the perturbation vertical vorticity and fields at the second peak for different  $Re$  and  $F_h$ . Qualitatively, we observe greater vari-

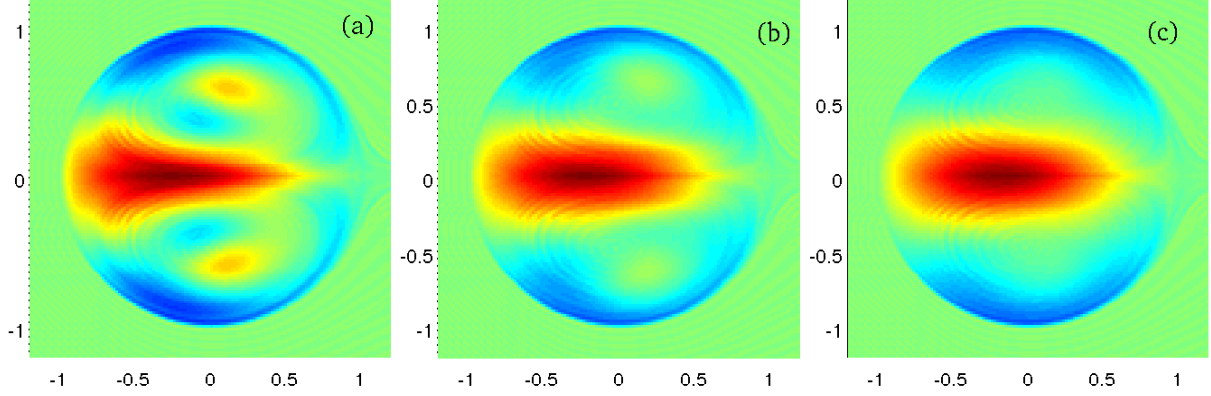


Figure 4.7: Perturbation vertical vorticity  $\omega_z$  at the zigzag peak for  $F_h = 0.2$  (left) ,  $0.1$  (middle) ,  $0.05$  (right) and  $Re = 20,000$ .

ation for different Froude numbers versus different Reynolds number as suggested above. At the largest Froude number, the perturbation vorticity is organised in thin strips around and inside the dipole core between the two vortices. Panels (b),(e),(h) have  $F_h = 0.1$  and have a similar overall structure to the larger Froude number. Here, in the cores of the vortices, there is an emergence of a swirl-like pattern. At lower Reynolds number, the structure is spread out due to diffusion, while at higher Reynolds number, small-scale structure is beginning to emerge. This trend continues overall as we move to lower Froude numbers.

Examining Figs. 4.11 (g)-(i) (fixed  $Re$  and decreasing  $F_h$ ), the core of the dipoles has a twisting-like behaviour as the Froude number decreases. From this we can conclude that the instability structure of the second peak depends more on the Froude number than on the Reynolds number, which again reinforces the buoyancy Reynolds number scaling. Indeed, if we consider the cases with  $Re_b = 50$  and  $200$  as above, which correspond to Fig. 4.11 (b),(g) and (c),(h) respectively, we can see similar structure in the vorticity fields. Additionally, the anti-symmetric structure of the perturbation can be observed in the dominant eigenmodes in all cases, as found by [6, 9].

Fig. 4.13 shows the perturbation structure for the zigzag peak (a) and the short-wave peak (b) for the case of  $Re = 5000$ ,  $F_h = 0.2$ . This case was chosen because the growth rates of the two wavenumbers is roughly the same (see Fig 4.2 a). The zigzag instability exhibits a quadrupole vorticity structure as discussed in [9], which corresponds to a bend and a



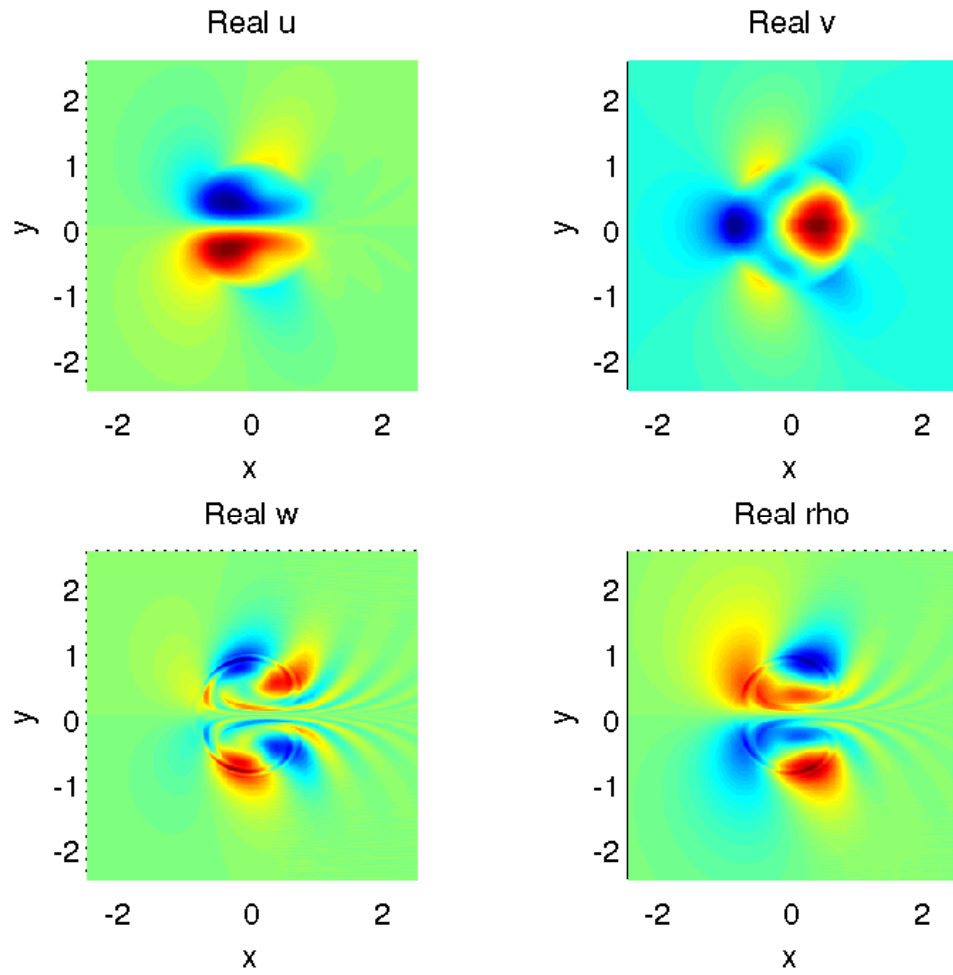


Figure 4.8: Perturbation fields  $u, v, w, \rho$  at the zigzag peak for  $F_h = 0.1$  and  $Re = 20,000$ . Here  $k_z = 6$ .

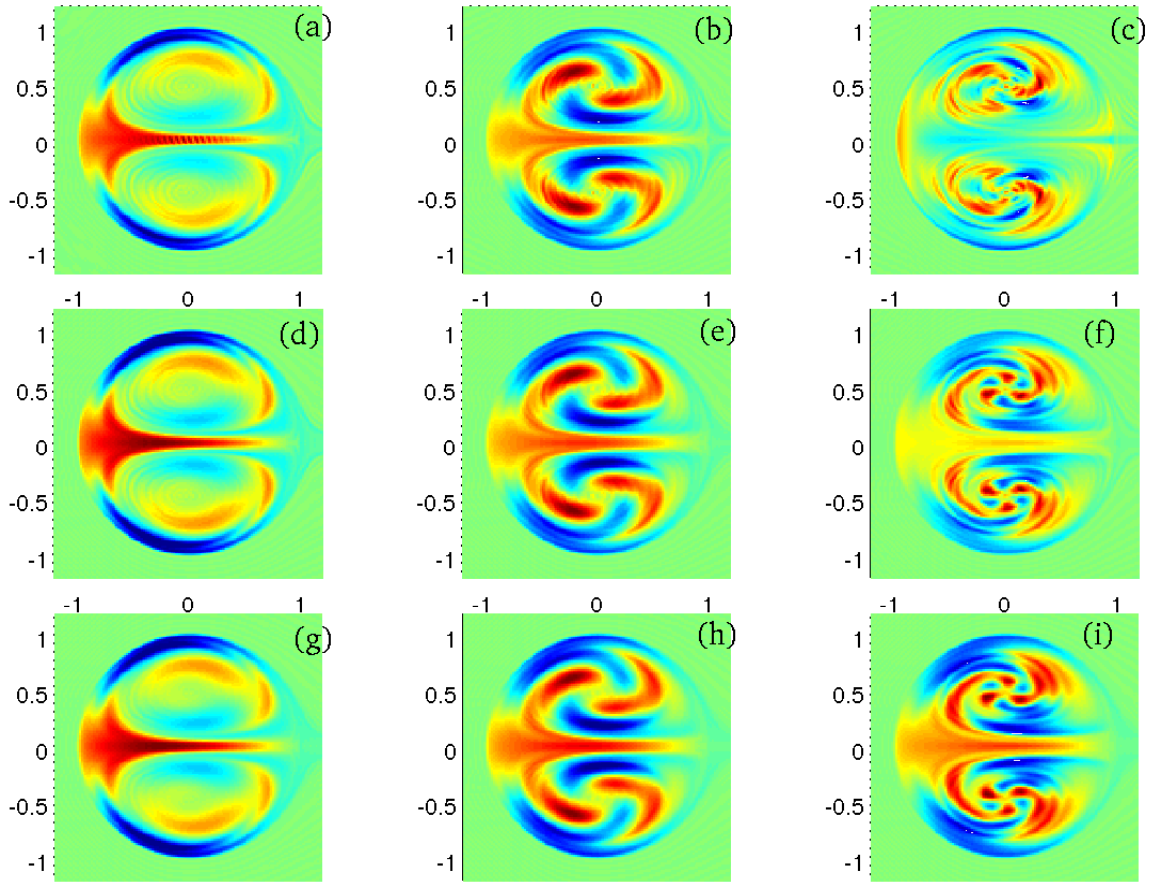


Figure 4.9: Perturbation vertical vorticity  $\omega_z$  at local oscillatory minimum for  $Re = 20,000$  (top) ,  $10,000$  (middle) ,  $5,000$  (bottom) ; and  $F_h = 0.2$  (left) ,  $0.1$  (middle) ,  $0.05$  (right) .

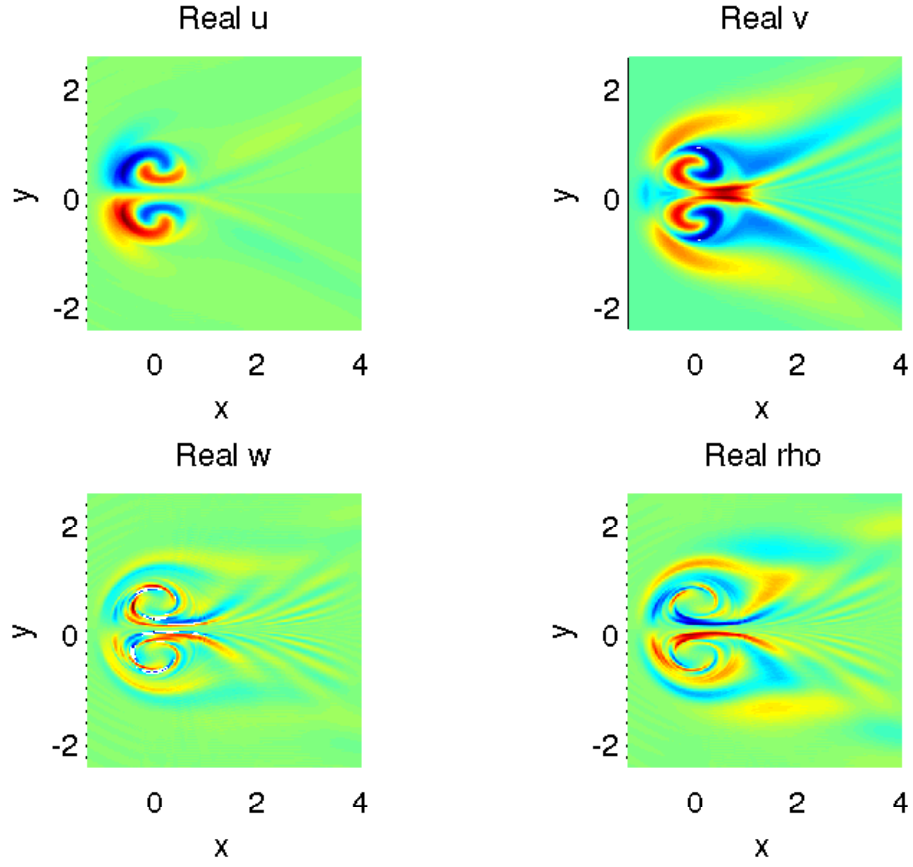


Figure 4.10: Perturbation fields  $u, v, w, \rho$  at the oscillatory minimum for  $F_h = 0.1$  and  $Re = 20,000$ . Here  $k_z = 20$ .

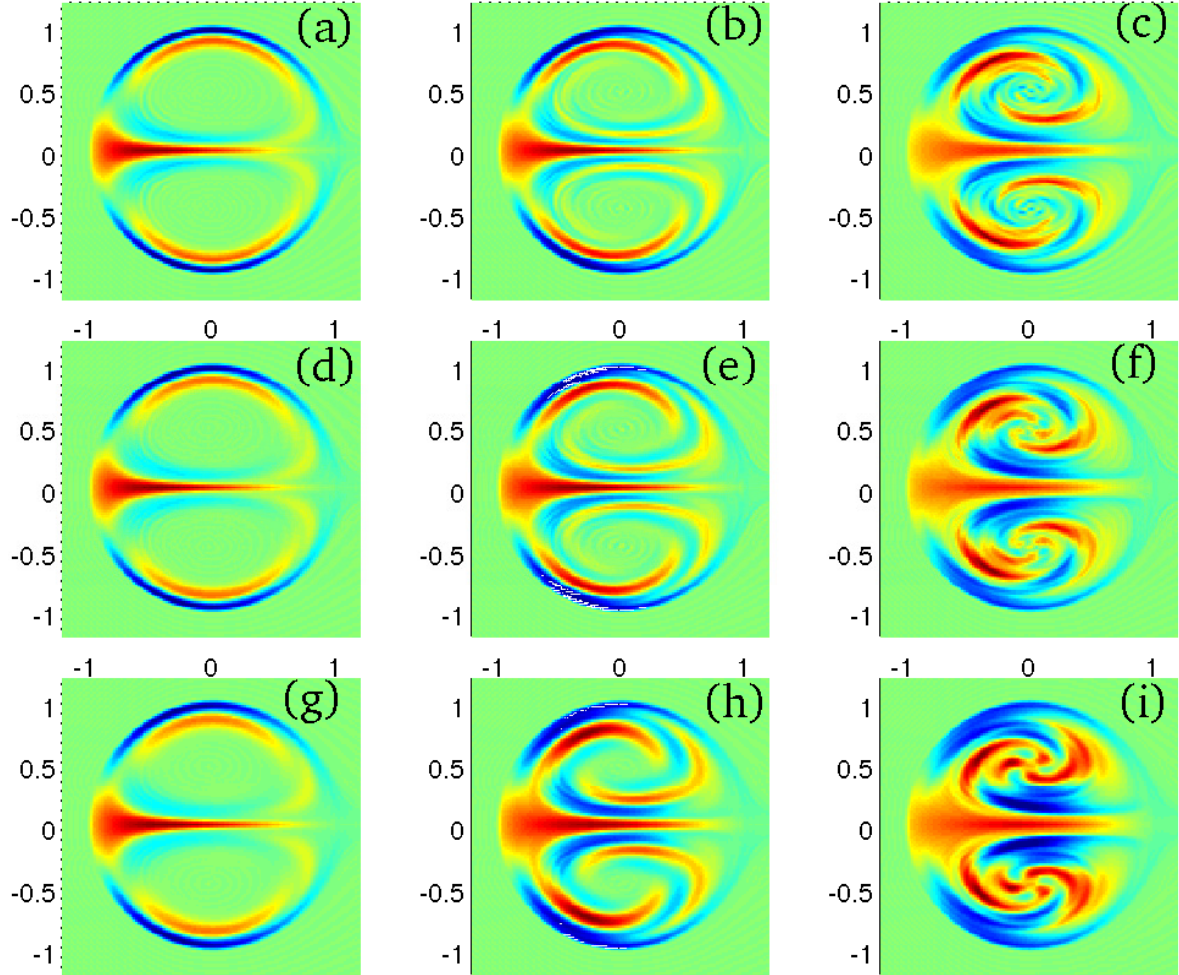


Figure 4.11: Perturbation vertical vorticity  $\omega_z$  at second peak for  $Re = 20,000$  (top) ,  $10,000$  (middle) ,  $5,000$  (bottom) ; and  $F_h = 0.2$  (left) ,  $0.1$  (middle) ,  $0.05$  (right) .

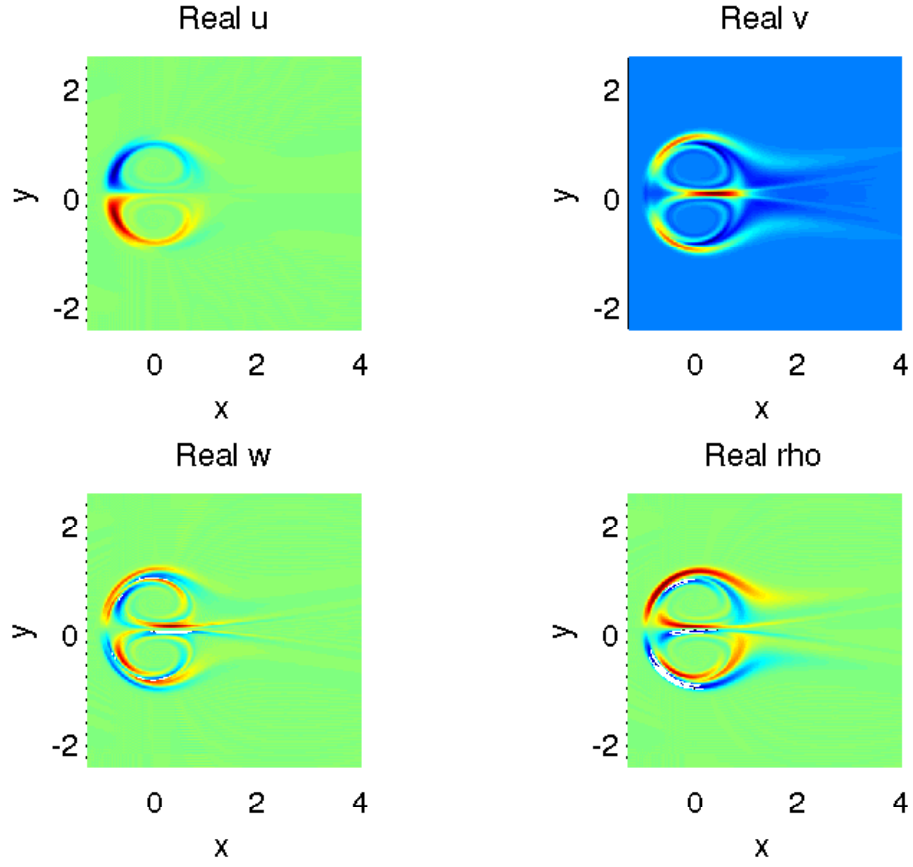


Figure 4.12: Perturbation fields  $u, v, w, \rho$  at the short wave instability for  $F_h = 0.1$  and  $Re = 20,000$ . Here  $k_z = 60$ .

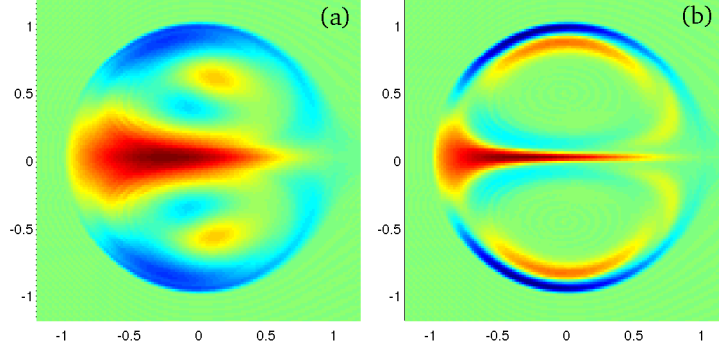


Figure 4.13: Perturbed vertical vorticity  $\omega_z$  at (a) the zigzag peak (b) the second peak for  $Re = 5000$ ,  $F_h = 0.2$

twist of the basic state dipole. The short-wave instability shares some common overall structure with the zigzag instability. Both have a line of vorticity centred in between two Lamb-Chaplygin vortices and have a ring of vorticity negative vorticity around the outer edges of the dipoles. Additionally, the number of local maximum and minimum remains the same. However, in the short-wave instability, these bands of vorticity have been squeezed into thinner strips and are much more localised along the outer edges of the vortices. In the cores of the dipoles, there is almost no structure and we do not see a quadrupole moment. The full vorticity field of the short-wave instability has a much more dominant twist than the zigzag instability and the bending of the dipole is reduced. As the stratification is increased, this behaviour continues but there is a significant emergence of structure within the cores of the vortices, as observed in Fig 4.11.

Fig. 4.14 demonstrates the structure of the  $v$  component of velocity for  $F_h = 0.1$  and  $Re = 20,000$  for a range of wavenumbers. Here the transition from the zigzag peak, through the oscillatory minimum to the short-wave instability is explicit. Initially the structure has a large positive and negative velocity but as we increase  $k_z$  this positive velocity is stretched forward and flattened out and becomes stretched out in the middle of the velocity field. The initial negative velocity simply dies out. The initial small areas of positive velocity in front of the dipole undergo an interesting evolution and become larger and stretched out wrapping around the back of the dipole and become very thin. The small initial negative velocity also becomes stretched out but instead forms a v-like shape behind the dipole. The evolution of this wake looks quantitatively similar to the wake of a boat through water. Fig. 4.15 is a loglog plot of the angle of this wake as a function of the perturbation

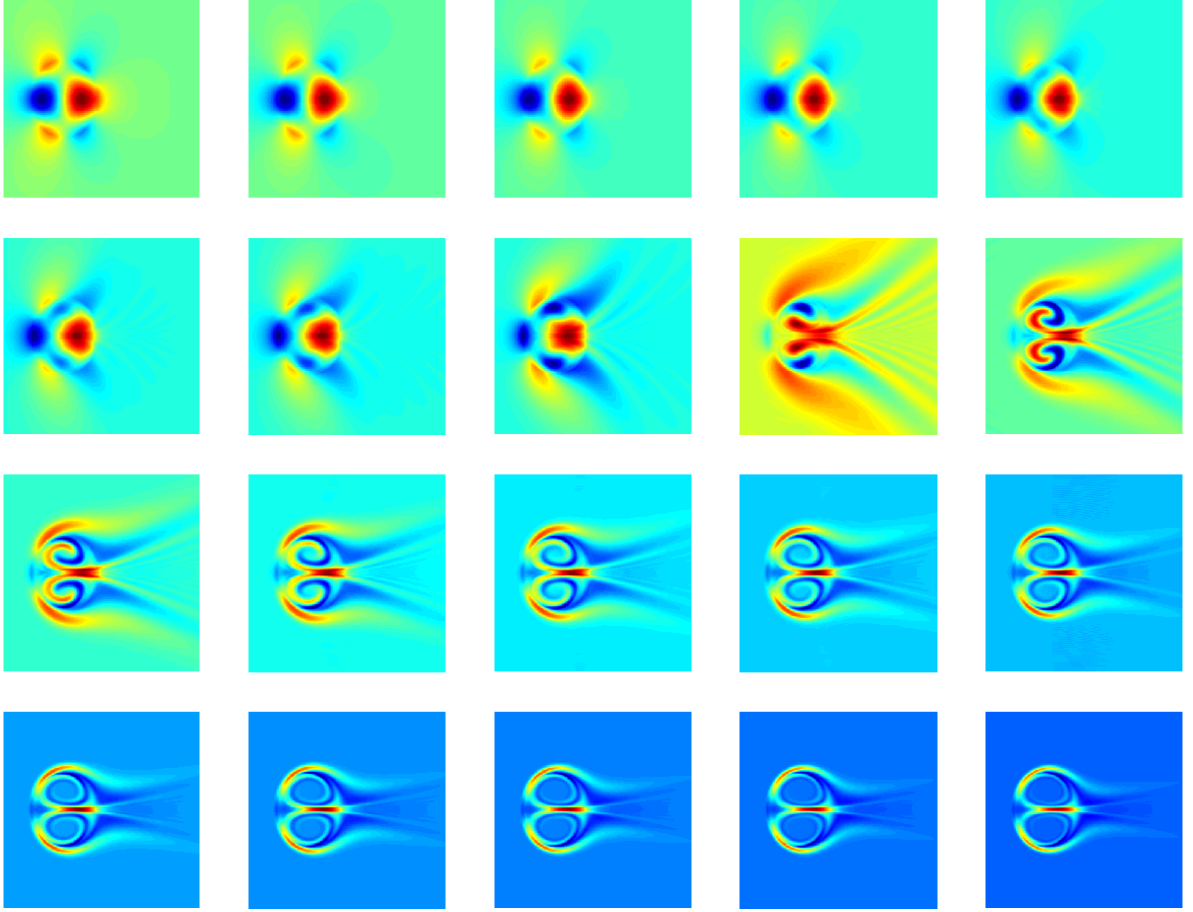


Figure 4.14: Structure of the  $v$  velocity from  $k_z = 3$  up to  $k_z = 110$  for  $F_h = 0.1$  and  $Re = 20,000$ . The wavenumber is increasing left to right and top to bottom. Here the scaling has not been applied to better illustrate the structure.

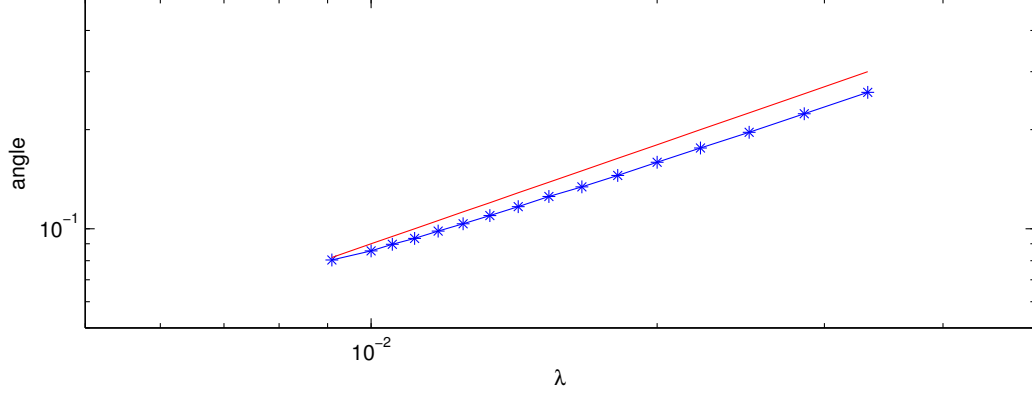


Figure 4.15: Angle of the wake behind the  $v$  velocity field as a function of the perturbation wavelength for  $F_h = 0.1$  and  $Re = 20,000$ . The red line is a reference slope of 1.

wavelength. The red line is a reference slope of  $k = 1$  and suggests the relationship between the angle and the wavenumber to be

$$\theta \sim \frac{1}{k_z}. \quad (4.4)$$

An investigation by Sharman and Wurtele [47] suggests an inverse relationship between the angle of the wake and the vertical wavenumber. However their stratification set-up is different from ours and it is unlikely their analysis carries over directly, however it does suggest there maybe a similar theory that can be derived for the case of waves behind vortices.

## 4.5 Subdominant modes

The method we have used so far is limited to only determining the leading eigenmode. An interesting question is whether or not we can determine sub-dominant eigenmodes and what we can learn from these modes. For example, is the same eigenmode dominating at both the zigzag peak and the short wave peak? To investigate this question, we use a Krylov space method to obtain the growth rates for subdominant modes (cite jet paper). Recall that our linear stability problem can be written as

$$\frac{d\mathbf{u}}{dt} = A\mathbf{u} \quad (4.5)$$



where  $\mathbf{u} = \mathbf{u}(\mathbf{x}, t)$  is vector of the unknowns and  $A$  is the associated linear operator. We can consider solutions of the form  $\mathbf{u}(\mathbf{x}, t) = \hat{\mathbf{u}}(\mathbf{x})e^{\sigma t}$ , where  $\sigma$  is the growth rate. Plugging in we obtain the following eigenvalue equation for  $u$

$$\sigma \hat{\mathbf{u}} = A \hat{\mathbf{u}}. \quad (4.6)$$

As mentioned, we have only been trying to find the leading eigenvalue  $\sigma$  but since this is an eigenvalue problem, many algorithms exist to find the eigenspectrum.

If we want to solve this eigenvalue problem, we must discretise the operator  $A$ . For our numerical scheme, we do not explicitly construct this operator because it would get very large. Our code is equivalent to this matrix multiplication if one were to write all the FFTs as a matrix multiplication. Writing out operators this way in practice is unfeasible since for our problem, it would require a matrix that is of size  $4N^2 \times 4N^2$  and is very dense. Thus trying to find the eigenvalues using a direct eigenvalue routine is not possible. Instead we investigate other algorithms that can determine the eigenvalues without computing  $A$  explicitly.

### 4.5.1 Krylov Eigenvalue Routines

One of the simplest and easiest to code algorithms for finding eigenvalues is the power method. It is given by the following iteration [36]

$$u_{k+1} = \frac{Au_k}{|Au_k|}, \sigma_k = \frac{u_k^t Au_k}{u_k^t u_k}. \quad (4.7)$$

The reasoning for this algorithm is very simple. If we suppose that the operator  $A$  has a spectrum of eigenvalues such that  $\lambda_1 > \lambda_2 > \dots$  then by the spectral theorem we can re-write the operator  $A$  as

$$A = \lambda_1 \mathbf{u}_1 \mathbf{u}_1^T + \lambda_2 \mathbf{u}_2 \mathbf{u}_2^T + \lambda_3 \mathbf{u}_3 \mathbf{u}_3^T + \dots \quad (4.8)$$

where  $\mathbf{u}_i$  is the eigenvector associated with  $\lambda_i$ . Now recall that by the spectral theorem we have the following [36]

$$\left(\frac{A}{\lambda_1}\right)^n = \mathbf{u}_1 \mathbf{u}_1^T + \left(\frac{\lambda_2}{\lambda_1}\right)^n \mathbf{u}_2 \mathbf{u}_2^T + \left(\frac{\lambda_3}{\lambda_1}\right)^n \mathbf{u}_3 \mathbf{u}_3^T + \dots \quad (4.9)$$

and since there is an ordering on the eigenvalues we have that  $\lambda_i/\lambda_1 < 1$  and hence as  $n \rightarrow \infty$  these terms will vanish. Thus if we consider a random initial vector  $\mathbf{b}_0$  we have

that

$$\frac{A^n \mathbf{b}_0}{\lambda_1^n} \rightarrow \mathbf{u}_1 \mathbf{u}_1^T \mathbf{b}_0, n \rightarrow \infty. \quad (4.10)$$

Now in practice we don't have  $\lambda_1$  but if we replace  $\lambda_1$  with the norm of  $|A^n \mathbf{b}_0|$  we can still get a good approximation [36]. By repeated iteration we obtain the scheme from above. This very simple algorithm is able to give us the leading eigenvalue and eigenvector starting from any random initial vector. A rigorous derivation is contained in any good numerical linear algebra book, e.g. Trefethen and Bau (cite).

One drawback of this method is that we are throwing away a lot of information at each iteration. It does not seem unreasonable that maybe these previous approximations can tell us something. Utilising this extra information is the key of Krylov methods. First, we define a Krylov sequence to be

$$\{u, Au, A^2u, \dots, A^{n-1}u\} \quad (4.11)$$

This definition is just taking the first  $n$  iterations of the power method and defining a sequence of them. Likewise we can also define the Krylov matrix as

$$K_n(A, u) = (u | Au | A^2u | \dots | A^{n-1}u) \quad (4.12)$$

where we are defining a new matrix whose  $i$ th column is the  $i$  iteration. This Krylov matrix allows us to compute the sub-dominant modes.

Consider the following matrix,  $L = K^{-1}AK$ , which is the similarity transformation of  $A$  by  $K$ . Recall that the eigenvalues of similar matrices are the same [36]. This is the key idea of the Krylov methods, if we apply a similarity transform to our original matrix  $A$  by  $K$  we can instead compute the eigenvalues of  $L$ . However we still are stuck with the inverse matrix  $K^{-1}$ . To compute this inverse, we orthogonalise  $K$  (by Gram-Schmidt) and thus  $K^{-1} = K^t$ .

So far everything has been exact since the size of  $K$  must be the same size as  $A$ . Now we make the approximation that we can replace  $K$  with  $K_n$ . Now taking the first  $n$  iterations, and  $n$  being small in some sense, let us define a new matrix  $P$  as above

$$P = K_n^t A K_n. \quad (4.13)$$

Now  $P$  is no longer the same size as  $A$ . Clearly the similarity properties no longer hold but if the eigenvalues of  $P$  are computed, they, rather amazingly, turn out to be a very good approximation to  $A$ . This leads to a very simple idea for finding dominant eigenvalues for

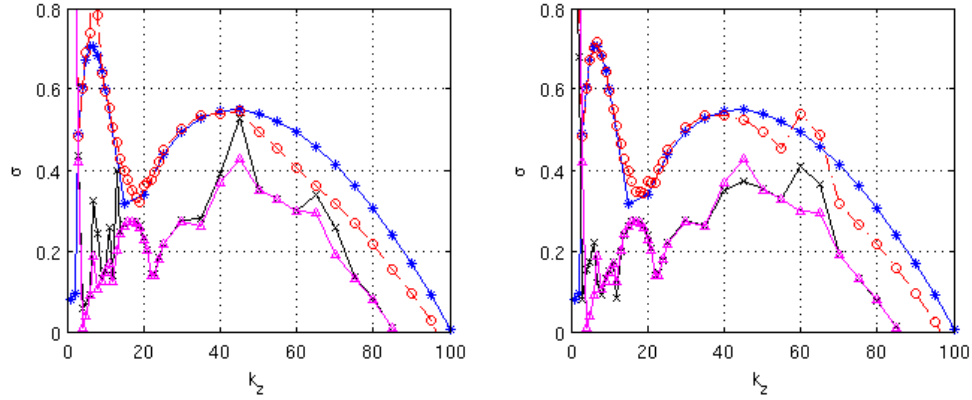


Figure 4.16: Krylov methods with two different choices of  $n = 50$  (left),  $100$  (right) for  $Re = 10000, N = 256, F_h = 0.1$ . Star denotes the dominant eigenvalues from the energy method, circle is the leading approximation from the Krylov method, triangle and x are the second and third eigenvalues respectively.

A: simply choose a small  $n$  and then find the eigenvalues of  $P$  which is only  $n \times n$  and there exist many good algorithms for finding the eigenvalues of small  $n$ .

This amazing fact has been fairly well understood for symmetric  $A$  and leads to the Lanczos algorithm [36] (Krylov book). The non-symmetric case is less well understood and leads to the Arnoldi iteration. Similar ideas of using Krylov sequences and matrices form the theoretical basis for conjugate gradient and GMRES algorithms for solving linear systems.

### 4.5.2 Results

Fig. 4.16 uses the Krylov method for finding sub dominant eigenvalues for the linear stability of a Lamb-Chaplygin dipole in a stratified fluid for  $Re = 10000, F_h = 0.1, N = 256$ . The reason  $N = 256$  was chosen was for memory issues in MATLAB. Some tests of various sizes of  $N$  showed some robustness although a thorough convergence investigation was not completed and the results were only compared to those of the previous sections. To find the Krylov sequence, the output from the simulation of the previous section was saved at certain times. Selecting  $n$  samples, they were orthogonalised using a Gram-Schmidt procedure and used to form the Krylov matrix  $K$ . To evaluate  $AK$  the linear code was

simulated as normal and reformatted into a giant vector. Then  $P$  was constructed and the eigenvalues of the resulting matrix were found using MATLAB's `eigs` routine.

The results of Fig. 4.16 are somewhat promising. As can be seen, doubling  $n$  does improve convergence, although there are still numerical anomalies, such as the random jump in growth rate at  $k_z = 60, 65$  for  $n = 100$ . As mentioned above, the theory of Krylov methods for non-symmetric matrices is still not well developed and few rigorous results on errors have been derived. The leading eigenvalue is reproduced accurately up to just about the short-wave peak before the Krylov results decay faster. The most promising result is at the local minimum between the two peaks. Here there is a very smooth curve of the growth rates of the second and third eigenmodes whose values are close to the values of the leading eigenmode. This result suggests that at this local minimum, a different eigenmode might be the dominate eigenmode for the short wave instability than that of the zigzag peak. Returning to the structure, Fig. 4.14 supports this viewpoint as the the zigzag and short-wave peak velocity fields are different and the oscillatory region in between suggests a combination of the two which might be the two different modes interchanging dominance and resulting in a mix of the two.

Finally, some attempts were made use MATLABs `eigs` routine and passing the operator  $A$  explicitly, instead of evaluating from a time series, were unsuccessful despite many hours of debugging.

## 4.6 Dimensional Analysis

Motivated by the scale analysis of those presented in the Chapter 2 review [32, 45, 10, 13], we present a scaling analysis for small vertical scales as considered in the above numerical simulations. We consider the Boussinesq equations

$$\frac{\partial \mathbf{u}'_h}{\partial t'} + \mathbf{u}'_h \cdot \nabla'_h \mathbf{u}'_h + u'_z \frac{\partial \mathbf{u}'_h}{\partial z'} = -\frac{1}{\rho_0} \nabla'_h p' + \nu \nabla'^2 \mathbf{u}_h, \quad (4.14)$$

$$\frac{\partial u'_z}{\partial t'} + \mathbf{u}'_h \cdot \nabla'_h u'_z + u'_z \frac{\partial u'_z}{\partial z'} = -\frac{1}{\rho_0} \frac{\partial p'}{\partial z'} - \frac{\rho' g}{\rho_0} + \nu \nabla'^2 u_z, \quad (4.15)$$

$$\nabla'_h \cdot \mathbf{u}'_h + \frac{\partial u'_z}{\partial z'} = 0, \quad (4.16)$$

$$\frac{\partial \rho'}{\partial t'} + \mathbf{u}'_h \cdot \nabla'_h \rho' + u'_z \frac{\partial \rho'}{\partial z'} + \frac{\partial \rho}{\partial z'} u'_z = D \nabla'^2 \rho', \quad (4.17)$$

where the primed notation denotes the dimensional variables in this section only.

Following [10] let  $U, W$  be the characteristic velocities in the horizontal and vertical directions,  $L_h, L_v$  be the corresponding characteristic length scales,  $P$  be the pressure, and  $R$  be density perturbation scales, not to be confused with the dipole radius  $R$  from above. We assume, differing from the analysis of [32, 10], that in addition to  $U, L_h$  being imposed on the system, we also impose a separate vertical scale  $L_v$ . This scaling is motivated by the above numerical simulations where we impose a vertical length scale through the vertical wavenumber  $k_z$ . The aspect ratio  $\delta = L_v/L_h$  is assumed to be small, i.e.  $\delta < 1$ . We define the horizontal Froude number to be  $F_h = U/NL_h$ , which is also assumed to be small. Following the above numerical simulations, let  $\delta < F_h$ , which we can also write as  $L_v < U/N$ , i.e. vertical scales are assumed to be smaller than the buoyancy scale. We now define the advective time scale  $T = L_h/U$ . To determine the characteristic scale of  $W$ , we are left with two choices: imposing the scaling from the continuity equation or from the density equation. Previous work [10] chose the latter and obtained a characteristic velocity

$$W \lesssim \frac{RF_h g}{\rho_0 N}. \quad (4.18)$$

By contrast, we use the continuity equation (4.16), which implies

$$W \lesssim \delta U. \quad (4.19)$$

This scaling for  $w$  is consistent with the assumption that  $\delta < F_h$ . Using (4.19), the vertical momentum equation (4.15) gives a density scaling of  $R \sim \rho_0 U^2 / (gL_v)$ . Plugging this result into (4.18), we obtain  $W \sim UF_h^2 / \delta$ . Because  $\delta < F_h$  we have  $U\delta < UF_h^2 / \delta$  so our assumptions are consistent. Setting  $W \sim U\delta$  the horizontal momentum equation (4.14) gives  $P \sim \rho_0 U^2$ . Combining this all, we obtain the following scaling for the Boussinesq equations with  $L_v < U/N$ :

$$\begin{aligned} \mathbf{u}'_h &= U \mathbf{u}_h, & u'_z &= U \delta u_z, & \rho' &= \frac{U^2 \rho_0}{gL_v} \rho, & p' &= \rho_0 U^2 p, \\ \mathbf{x} &= L_h x, & z' &= L_v z, & t' &= \frac{L_h}{U} t, & Re &= \frac{UL_h}{\nu}, & Sc &= \frac{\nu}{D} \end{aligned} \quad (4.20)$$

which leads to

$$\frac{\partial \mathbf{u}_h}{\partial t} + \mathbf{u}_h \cdot \nabla_h \mathbf{u}_h + u_z \frac{\partial \mathbf{u}_h}{\partial z} = -\nabla_h p + \frac{1}{Re} \nabla_h^2 \mathbf{u}_h + \frac{1}{\delta^2 Re} \frac{\partial^2 \mathbf{u}_h}{\partial z^2}, \quad (4.21)$$

$$\delta^2 \left( \frac{\partial u_z}{\partial t} + \mathbf{u}_h \cdot \nabla_h u_z + u_z \frac{\partial u_z}{\partial z} \right) = -\frac{\partial p}{\partial z} - \rho' + \frac{\delta^2}{Re} \nabla_h^2 u_z + \frac{1}{Re} \frac{\partial^2 u_z}{\partial z^2}, \quad (4.22)$$

$$\nabla_h \cdot \mathbf{u}_h + \frac{\partial u_z}{\partial z} = 0, \quad (4.23)$$

$$\frac{\partial \rho'}{\partial t} + \mathbf{u}_h \cdot \nabla_h \rho' + u_z \frac{\partial \rho'}{\partial z} - \frac{\delta^2}{F_h^2} u_z = \frac{1}{ReSc} \nabla_h^2 \rho' + \frac{1}{\delta^2 ReSc} \frac{\partial^2 \rho'}{\partial z^2}, \quad (4.24)$$

which holds when  $\delta < F_h \ll 1$ . This suggests that for very small vertical scales with  $\delta \ll F_h$  the effects of stratification should be negligible. At such small vertical scales, density variation due to stratification would be negligible and thus we would not expect stratification to play an important role in the overall evolution. Additionally, the presence of the factors of  $\delta$  in the denominator of the vertical viscous terms suggests that the effects of viscosity become more dominant at very small vertical scales.

As a result of this scaling analysis we expect that the nature of the instability at short vertical scales to become independent of  $F_h$  for large  $k_z$ . To test this hypothesis Fig. 4.17 shows growth rate as a function of  $k_z$  for four sets of simulation with  $Re = 10,000$ :  $F_h = 0.2, 0.1, 0.05$  and a new unstratified case with  $F_h = \infty$  (note that, unlike in Fig. 4.4, we are not scaling  $k_z$  by  $F_h$ ). The growth rate curves appear to be converging for large  $k_z$  where  $\delta \ll F_h$ , which agrees with the conclusion of the above scaling analysis. These large  $k_z$  are well into the viscous damping range and as discussed above, the effects of viscosity become stronger and we observe a sharper decrease in the growth rate.

For the short-wave instability examined above,  $\delta/F_h = 1/(k_z F_h)$  ranges from  $\approx 0.5$  down to 0.1, which is  $< 1$  but not  $\ll 1$ . As a result, we do not necessarily expect the characteristics of this instability to be independent of  $F_h$  for the parameters considered here. Indeed, our stability analysis shows that the (unscaled) wavenumber  $k_z$  of the short-wave peak is weakly dependent on  $F_h$ , through the  $F_h^{1/5}$  factor in (4.3). However, by examining even larger  $k_z F_h$  (i.e. even smaller  $\delta/F_h$ ), this scale analysis suggests that the nature of the short-wave instability will eventually become independent of  $F_h$ .

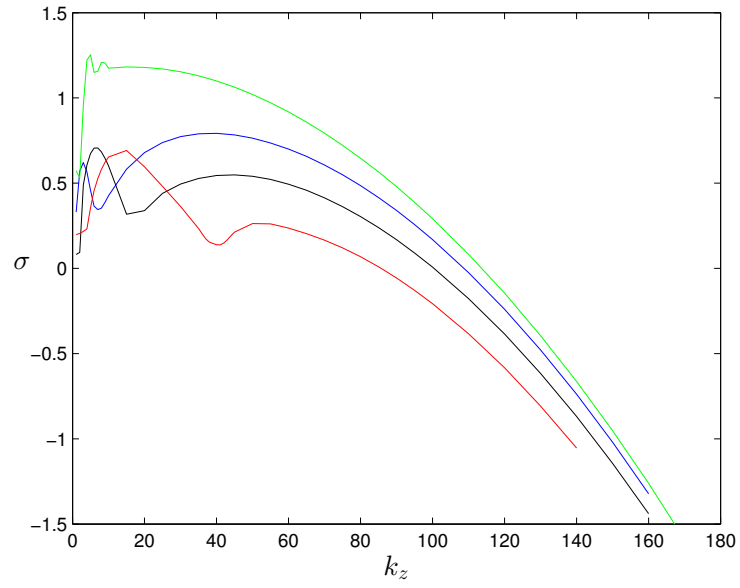


Figure 4.17: Growth rate  $\sigma$  as a function  $k_z$  at  $Re = 10,000$  with  $F_h = \infty$  (green),  $F_h = 0.2$  (blue),  $F_h = 0.1$  (black),  $F_h = 0.05$  (red)

# Chapter 5

## Nonlinear theory

In this chapter we extended the results of the linear stability analysis to a nonlinear analysis. Through numerical simulations, we suggest that the saturation level of the short-wave aspect ratio depends upon the aspect ratio.

### 5.1 Set-up

In this section we discuss some numerical tests of the code to verify that the nonlinear results are correctly resolving the smallest scales. In order to do a full DNS, we need to resolve the Kolmogorov scales. The Kolmogorov scale is given by (cite)

$$\eta = \left( \frac{\nu^3}{\epsilon} \right)^{1/4} \quad (5.1)$$

where  $\epsilon$  is the energy given by

$$\epsilon \sim \frac{U^3}{R} \quad (5.2)$$

where  $U, R$  are the characteristic velocity and length respectively. Rewriting the Kolmogorov scale  $\eta$  in terms of the Reynolds number by multiplying by the characteristic length  $R$ , which we take to be unity as has been suggested from the linear results, to obtain

$$\eta = \frac{1}{\text{Re}^{3/4}} \quad (5.3)$$



For our simulations, the code separates the horizontal and vertical resolutions, which we denote by  $\Delta x$  and  $\Delta z$ . We want to choose the number of grid points to be such that  $\Delta x \approx \Delta z$ .

To illustrate, we consider a test case that was run to determine whether or not to use  $L = 9$  or  $L = 5$  for the box size. Both have been used in practice (cite). Consider a grid with  $N \times N \times n$  points, where we have explicitly separated out the horizontal and vertical directions. Because we need to resolve the Kolmogorov scales, we have restrictions on the total number of grid points. We consider the case of  $Re = 2000$  and  $F_h = 0.2$ . The Reynolds number tells us that the Kolmogorov scale is

$$\eta \sim \frac{1}{Re^{3/4}} \approx 0.003343, \quad \Delta x \sim \eta \quad (5.4)$$

and thus we want a grid spacing that is approximately 0.003343. Since it is desirable for  $N$  to be a power of two, if  $N = 1024$  we have that

$$\Delta x = \frac{L}{1024}. \quad (5.5)$$

If  $L = 9$  then  $\Delta x = 0.00878$  and if  $L = 5$  then  $\Delta x = 0.00488$ . It is clear that it is more desirable to pick  $L = 5$  because the grid spacing is closer to the  $\eta$ .

Now we need to set the vertical resolution. It is important that we have the same resolution for the vertical and horizontal so  $\Delta x \approx \Delta z$ . Since we are interested in investigating the short-wave instability the vertical scale is

$$H \sim \frac{2\pi}{k_z}. \quad (5.6)$$

In this case, the greatest growth rate occurs at the wavenumber  $k_z = 20$  and thus the vertical scale is  $H = 0.314$ . Now setting  $\Delta z \approx \Delta x$  for both  $L = 5, 9$  we find that for  $L = 9$  if  $n = 32$  then  $\Delta z = 0.00982$  which is close to  $\Delta x = 0.00878$ . If  $L = 5$  then if  $n = 64$  then  $\Delta z = 0.00491$  which is close to  $\Delta x = 0.00488$ . Thus to resolve the Kolmogorov scale as much as possible, we should choose  $L = 5$  with  $N = 1024, n = 64$  over  $L = 9$  with  $N = 1024, n = 32$ . However when the code is actually run  $L = 5$  takes roughly 30.8 hours of real time versus 19.5 hours of real time. Additionally, due to the way the code is set-up,  $L = 5$  requires twice as many processors as  $L = 9$ . Additionally, due to the way the code is set-up,  $L = 5$  requires twice as many processors as  $L = 9$  which requires more resources. Thus a trade-off must be made between running at a higher resolution but taking longer versus running at a lower resolution, in the processing potentially not resolving the Kolmogorov scale, but running faster.

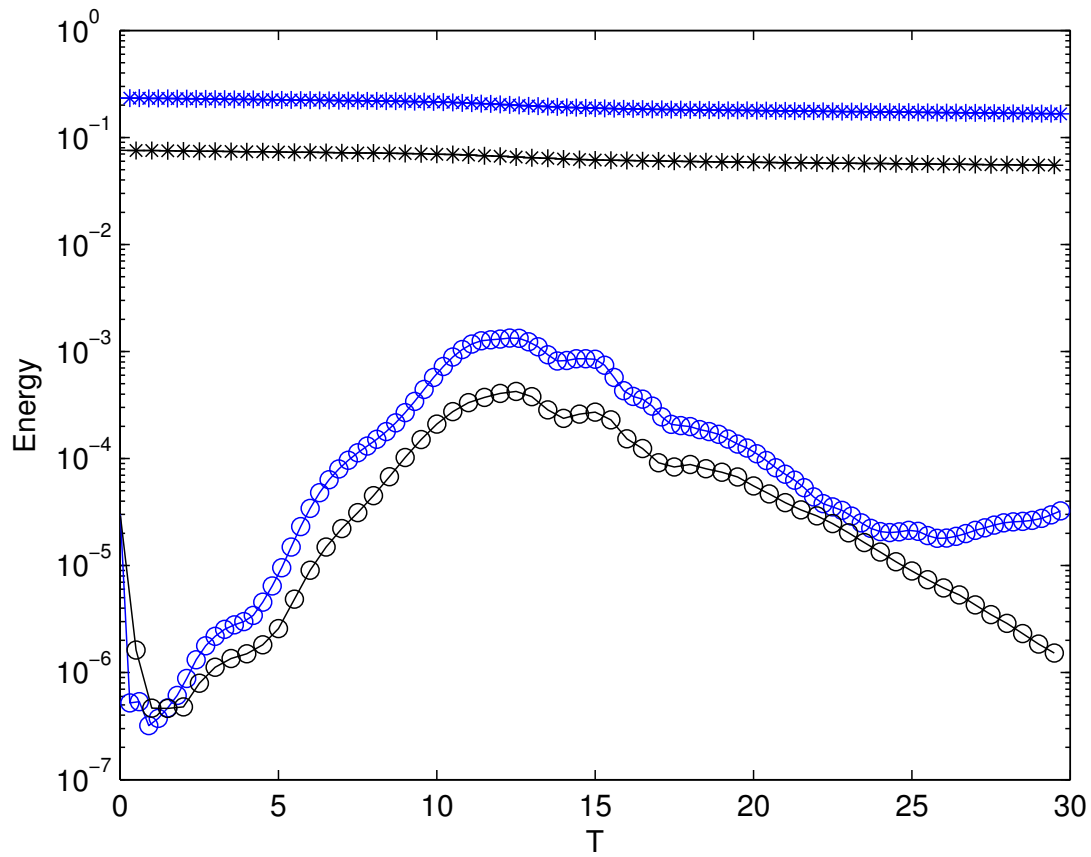


Figure 5.1: Time series of the potential energy (circle) and kinetic energy (star) for  $L = 5$  (blue) and  $L = 9$  (black).

In Fig. 5.1 we demonstrate two tests run that were done to determine what resolution to use. Qualitatively, both curves are very similar, with the  $L = 5$  curves shifted upwards by a constant. This is to be expected because by using a larger domain size, less of the domain is focused on the dipole and thus there is less energy in this dipole. When we decrease the domain size, the dipole takes up a larger percentage of the grid and thus has a larger energy.

When we compute the growth rates and saturation levels, they are in close agreement. Thus we choose  $L = 9$  and  $n = 32$  for our simulations despite not completely resolving the Kolmogorov scale. Our time step  $\Delta = 5.0 \times 10^{-4}$ . Each run was initialised with a random density sinusoidal perturbation with  $\epsilon = 0.01$ .

## 5.2 Results

The nonlinear evolution of the short-wave instability tells us how the zigzag instability and the short-wave instability interact. Investigations by Waite and Smolarkiewicz into the breakdown of the Lamb-Chaplygin dipole into turbulence and observed that the energy of the zigzag instability grew such that it became the same order of magnitude as the kinetic energy. In these simulations, no short-wave instabilities were observed despite having a similar growth rate. We present results that suggest that the short-wave instability saturates at a level proportional to the aspect ratio  $\delta$ .

To investigate the saturation level, nonlinear simulations were run with an initially small,  $\epsilon = 0.01$ , random sinusoidal perturbation of the initial density. Fig. 5.2 is an example of the evolution of the energy for  $Re = 5000$  and  $F_h = 0.2$ . As can be observed in the saturation level occurs at roughly  $T = 20$  after which the potential energy states approximately constant. The saturation is defined to be

$$\text{saturation} = \frac{E_{3D}}{E_{2D}} \quad (5.7)$$

where we find the maximum  $E_{3D}$  at later times and divide that time by the kinetic energy.

Fig. 5.3 and Fig. 5.4 demonstrate the saturation level for  $F_h = 0.2$  and  $Re = 2000, 5000$  respectively. The reference line is a slope of 2. In Fig. 5.4 there is some variation in the data points as the length scales get smaller, the definition of when the saturation first occurs is ambiguous. This effect can be observed in Fig. 5.2 as at  $T = 30$  the saturation level has increased a little bit from the start of the saturation at  $T = 20$ . Despite this slight increase, it is clear that the potential energy has saturated.

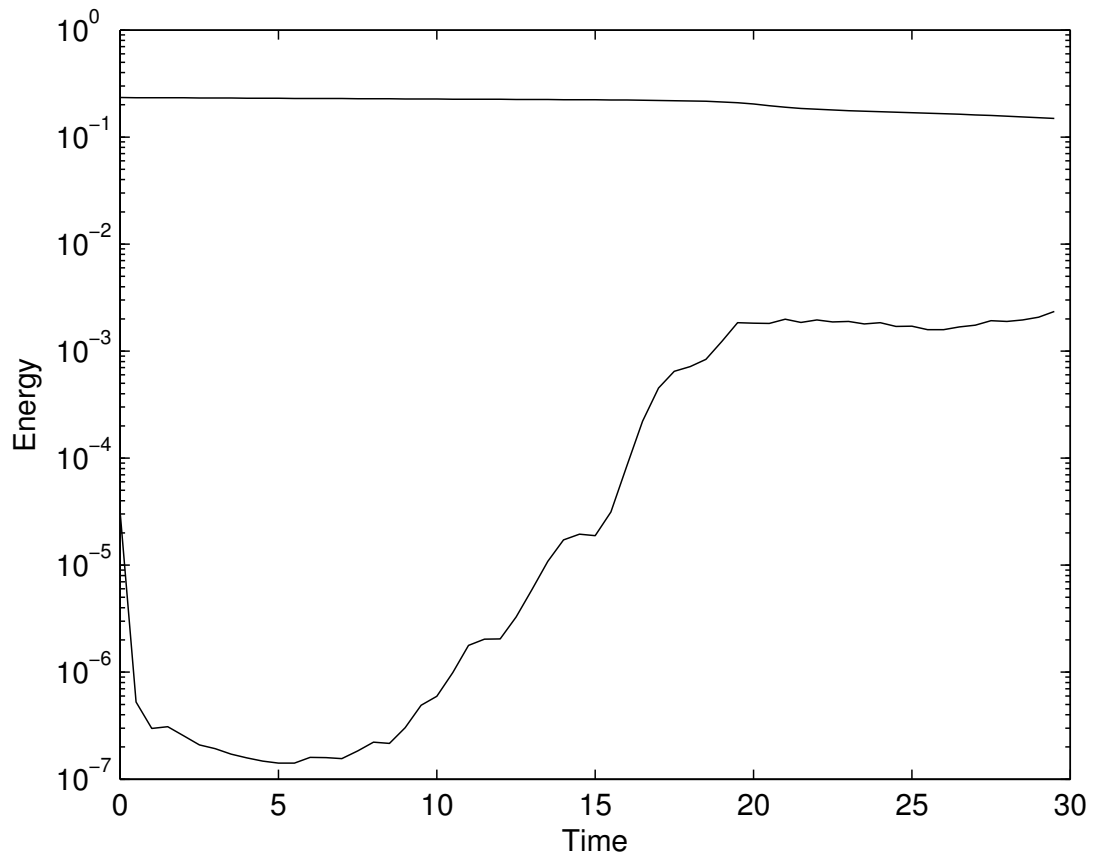


Figure 5.2: Time series of the kinetic energy (top line) and potential energy (bottom line) for  $Re = 5000$  and  $F_h = 0.2$ .

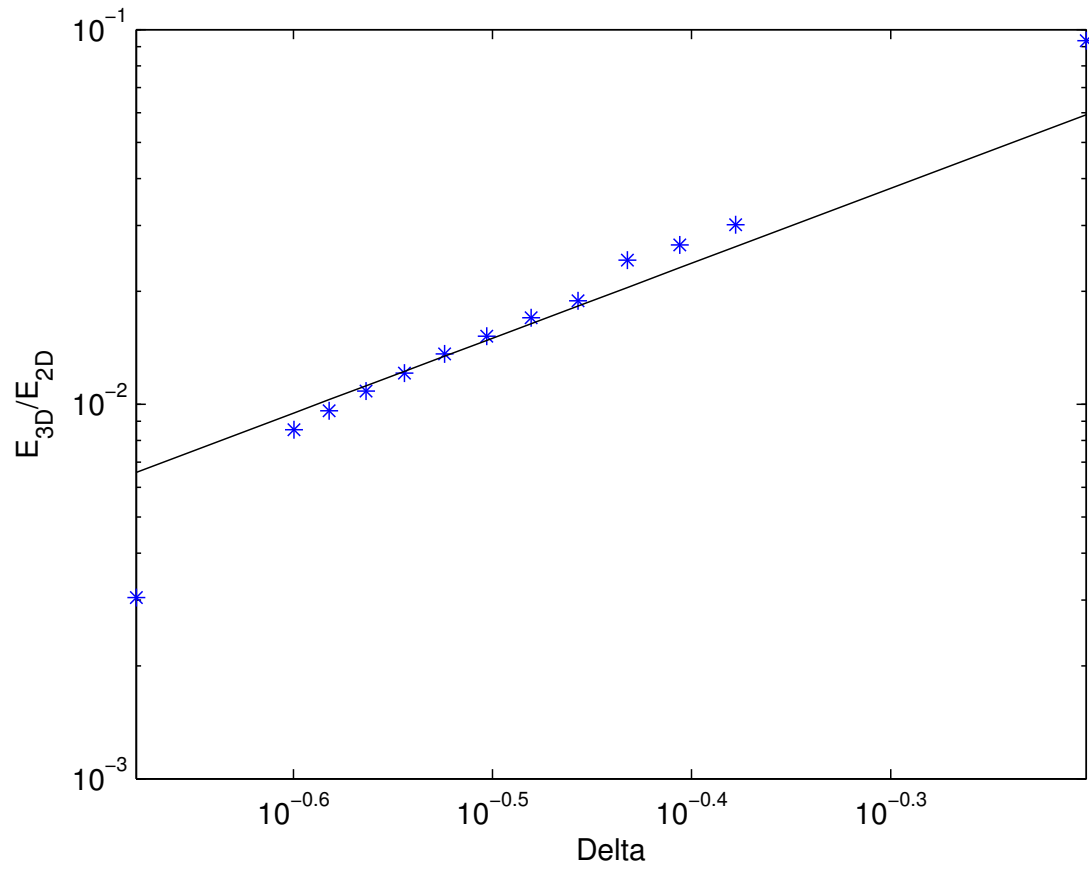


Figure 5.3: Saturation levels for a range of aspect ratios for  $Re = 2000$  and  $F_h = 0.2$ .

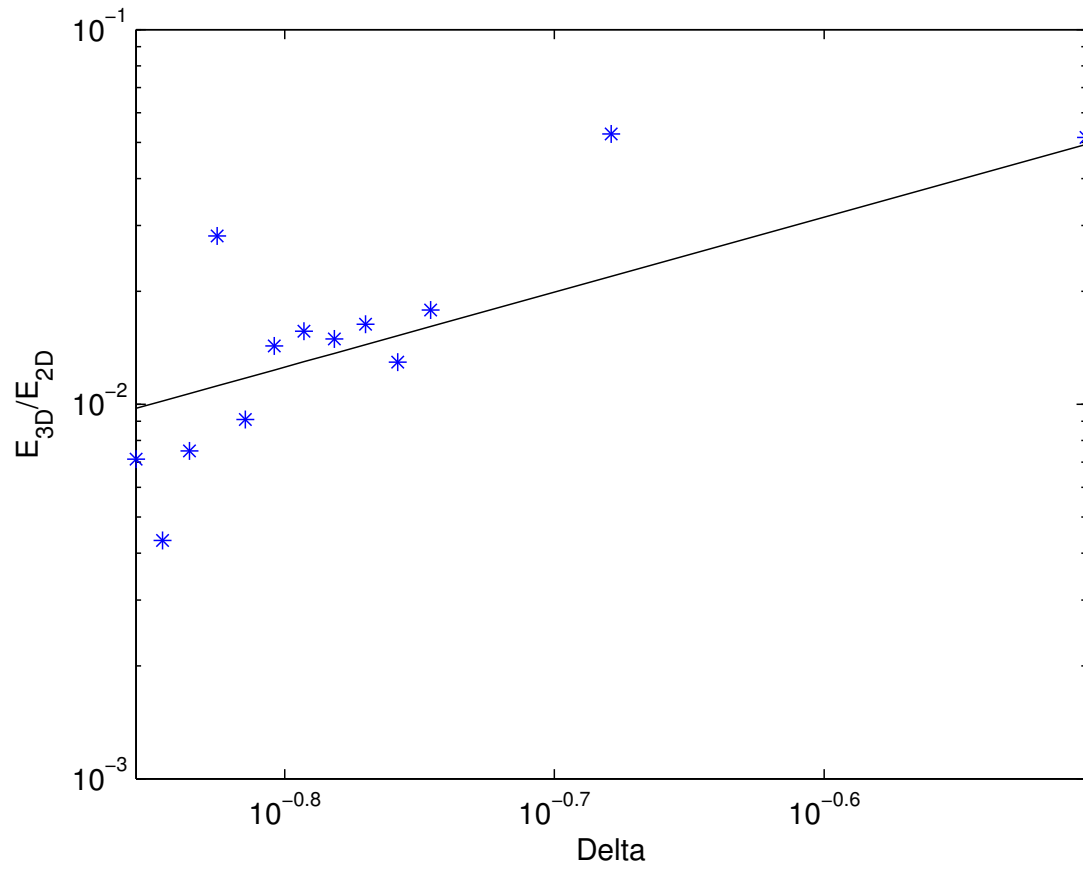


Figure 5.4: Saturation levels for a range of aspect ratios for  $Re = 5000$  and  $F_h = 0.2$ .

The linear fit through these curves suggests that the saturation level depends upon  $\delta$  as

$$\frac{E_{3Dsat}}{E_{2Dsat}} \sim \delta^2. \quad (5.8)$$

This scaling suggests that as the aspect ratio gets smaller, the saturation level decreases. In Chapter 3, we found that the short-wave instability scaled as  $k_z \sim F_h^{-1/5} Re^{2/5}$  thus

$$\frac{E_{3Dsat}}{E_{2Dsat}} \sim \frac{F_h^{2/5}}{H^2 Re^{4/5}}. \quad (5.9)$$

Thus as we increase the  $Re$  or horizontal length scale, the saturation level decreases. Alternatively, if we increase stratification, i.e. decrease the Froude number, the saturation level also decreases. Thus, we should not expect the short-wave instability to play a significant role in the evolution of the Lamb-Chaplygin's transition to turbulence.

The scaling suggested has a theoretical backing. In investigations by Ngan, et al [39] into quasi-two dimensional turbulence, they determined that the saturation level of a perturbation depended linearly upon the aspect ratio. We review their derivation. Ngan et. al [39] consider quasi-two dimensional turbulence, which they define to be the three-dimesionalisation of a two-dimensional flow. The study of such flows are motivated by geophysical applications where aspect ratios range from  $\delta \sim 0.01 - 0.1$  [39].

Ngan et al. now consider a simple scaling analysis [39]. Initially the time scales of the 2D base flow is long compared to that of the 3D base flow. In our results, we verify this. In figure blah note that the time scale of the 2D perturbation, here the top line, is constant while the timescale of the 3D flow is much shorter, which is exemplified by the change that the 3D perturbation goes through over the first 20 or seconds. However once the 3D perturbation saturates, it stops growing and its timescale becomes similar to that of the 2D flow. Now consider the following timescales for these flows [39] as

$$T_{2D} = \frac{U}{L}, \quad T_{3D} = \frac{u}{H} \quad (5.10)$$

where  $U$  is the characteristic velocity of the 2D flow and  $u$  is the characteristic velocity. Thus at saturation  $T_{2D} \sim T_{3D}$  and thus we have that

$$\frac{U}{L} \sim \frac{u}{H} \Rightarrow \frac{u}{U} \sim \frac{H}{L} = \delta. \quad (5.11)$$

However we are considering the energy and thus we would have to square both sides to get the energy resulting in

$$\frac{E_{2D}}{E_{3D}} \sim \delta^2 \quad (5.12)$$

which is the result suggested by Figs. 5.3 and Fig. 5.4. Thus, the short-wave instability, despite having a similar growth rate to that of the zigzag instability, is saturated at a level proportional to the aspect ratio of the flow, which in stratified flows, is small.

Furthermore, in the scaling analysis derived in the previous chapter, if  $\delta < F_h \ll 1$ , let us neglect terms of the form  $F_h/\delta$ , then we would have

$$\frac{\partial \mathbf{u}_h}{\partial t} + \mathbf{u}_h \cdot \nabla_h \mathbf{u}_h + u_z \frac{\partial \mathbf{u}_h}{\partial z} = -\nabla_h p + \frac{1}{Re} \nabla_h^2 \mathbf{u}_h + \frac{1}{\delta^2 Re} \frac{\partial^2 \mathbf{u}_h}{\partial z^2}, \quad (5.13)$$

$$\delta^2 \left( \frac{\partial u_z}{\partial t} + \mathbf{u}_h \cdot \nabla_h u_z + u_z \frac{\partial u_z}{\partial z} \right) = -\frac{\partial p}{\partial z} - \rho' + \frac{\delta^2}{Re} \nabla_h^2 u_z + \frac{1}{Re} \frac{\partial^2 u_z}{\partial z^2}, \quad (5.14)$$

$$\nabla_h \cdot \mathbf{u}_h + \frac{\partial u_z}{\partial z} = 0, \quad (5.15)$$

$$\frac{\partial \rho'}{\partial t} + \mathbf{u}_h \cdot \nabla_h \rho' + u_z \frac{\partial \rho'}{\partial z} - u_z = \frac{1}{ReSc} \nabla_h^2 \rho' + \frac{1}{\delta^2 ReSc} \frac{\partial^2 \rho'}{\partial z^2}. \quad (5.16)$$

Here stratification has dropped out of the equations of motion and, as discussed, the short-wave instability shouldn't depend on stratification. These equations are very similar to the starting equations of Ngan et al. [39] (+prev paper) which further suggests a link between their derivation and our result. It is important to note, however, that the results of [39] + other are for an inviscid theory. In Fig. 5.1 the saturation level lasts for only a few seconds before the potential energy decreases, most likely due to viscous effects. Regardless, the result is still robust enough that even if the saturation level begins to decrease due to viscosity, its initial maximum is still determined by the aspect ratio.

We conclude with examining the growth rate of the linear theory and that of the nonlinear theory. In comparing the linear theory with the nonlinear theory, there is a problem with what defines the linear regime of the nonlinear simulation. If we examine Fig. 5.2, the growth of the potential energy between  $T = 5$  and  $T = 20$ , it is very difficult to justify approximating this growth rate as linear. For most of the cases of  $Re = 5000$  and  $F_h = 0.2$ , we were unable to determine a consistent way to determine the growth rate of the perturbation and thus we have not included the results for this simulation. Fig. 5.1, which choses a  $Re = 2000$  and  $F_h = 0.2$  case illustrates the more linear growth rate exhibited by these simulations. Fig. 5.5 illustrates the results for the linear and nonlinear



theories for  $Re = 2000$  and  $F_h = 0.2$ . Here the nonlinear results are greater than those of the linear theory, however the curve still follows the linear theory curve. Again, the issue of the growth in the potential energy not being perfectly linear could contribute to this discrepancy of  $8\% - 40\%$ .

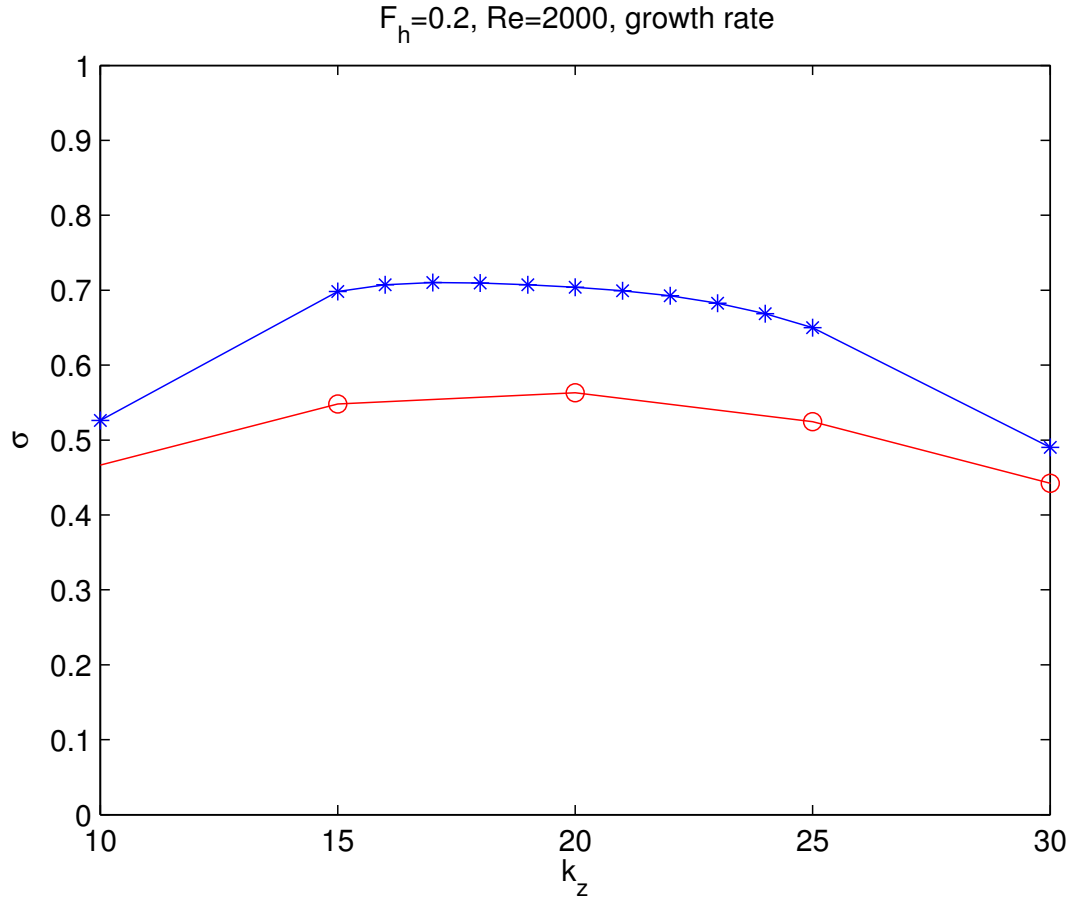


Figure 5.5: Growth rate for  $Re = 5000$  and  $F_h = 0.2$  with the linear results (red) and the nonlinear results (blue). Note we have not scaled by  $F_h$  unlike the results in Chapter 3.

# Chapter 6

## Conclusions

1. oscillatory instability inbetween peak growth rates
2. check for other systems
3. waves behind seem interesting

# APPENDICES

# Appendix A

## Matlab Code for Solving Advection Equation

The following code is the MATLAB code for evaluating the advection-diffusion equation with 2/3s deliasing

```
%construct the grid and basic parameters
N=128; dx=2*pi/N; x=dx*(1:N);t=0;dt=dx/10;tf=5;nsteps=ceil(tf/dt);
c=0.2+sin(x-1).^2;
%store the wavenumbers
kx=[0:N/2-1 0 -N/2+1:-1];
%define cut to cut out the highest Fourier modes
cut=ones(1,N); ksq=kx.*kx;
%cut out the Fourier co-efficients according to dealiasing
%because of wavenumber ordering cut out (most negative wave numbers start
%at N/2) e.g. (2/3)*(N/2) : (N/2+(1/3)(N/2) for 2/3s
cut(ceil(dealias_coeff*N/2):(N/2+ceil((1-dealias_coeff)*N/2))+1)=0;
%initial condition
u=exp(-100*(x-1).^2);uhat=fft(u);
%do initial timestep using Euler
Fold=-fft(c.*real(ifft(1i*cut.*kx.*uhat)));
uhat=(uhat+dt*Fold);

%do Adams Bashforth
for i=1:nsteps
```

```

    F=-fft(c.*real(ifft(1i*cut.*kx.*uhat)));
    uhat=uhat+1.5*dt*F-0.5*dt*Fold;
    Fold=F;
end

```

In the above code the line `ifft(1i*cut.*kx.*uhat)` evaluates the spectral derivative of the velocity field and adds in the dealiasing by cutting out the top 1/3 of the Fourier coefficients. Note that MATLAB stores the wavenumbers `kx=[0:N/2-1 0 -N/2+1:-1]` and thus to zero out the correct coefficients requires some clever index manipulation.

# References

- [1] David J Acheson. *Elementary fluid dynamics*. Oxford University Press, 1990.
- [2] P. Augier and P. Billant. Onset of seconardy instabilities on the zigzag instability in stratified fluids. *J. Fluid Mech*, 682:120–131, 2011.
- [3] P. Augier, J.-M. Chomaz, and P. Billant. Spectral analysis of the transition to turbulence from a dipole in stratified fluid. *J. Fluid. Mech*, 713:86–108, 2012.
- [4] B.J. Bailey. Three-dimensional instability of elliptical flow. *Phys. Rev. Lett.*, 57:2160, 1986.
- [5] G.K. Batchelor. *An Introduction to Fluid Dynamics*. Cambridge University Press, 1967.
- [6] P. Billant, P. Brancher, and J.-M. Chomaz. Three-dimensional stability of a vortex pair. *Phys. Fluids*, 11:2069–2077, 1999.
- [7] P. Billant and J.-M. Chomaz. Experimental evidence for a new instability of a vertical columnar vortex pair in a strongly stratified fluid. *J. Fluid Mech*, 418:167–188, 2000.
- [8] P. Billant and J.-M. Chomaz. Theoretical analysis of the zigzag instability of a vertical columnar vortex pair in a strongly stratified fluid. *J. Fluid Mech*, 419:29–63, 2000.
- [9] P. Billant and J.-M. Chomaz. Three-dimensional stability of a vertical columnar vortex pair in a stratified fluid. *J. Fluid Mech*, 419:65–91, 2000.
- [10] P. Billant and J.-M. Chomaz. Self-similarity of strongly stratified inviscid flows. *Phys. Fluids*, 13(6):1645–1651, 2001.
- [11] L. Bovard and M.L. Waite. Short wave vortex instability in stratified fluids. *Physics of Fluids*, Submitted.

- [12] J.P. Boyd. *Chebyshev and Fourier Spectral Methods*. Dover books on mathematics. Dover Publications, 2001.
- [13] G. Brethouwer, P. Billant, E. Lindborg, and J.-M. Chomaz. Scaling analysis and simulations of strongly stratified turbulent flows. *J. Fluid Mech*, 585:343–368, 2007.
- [14] C. Canuto. *Spectral Methods: Evolution to Complex Geometries and Applications to Fluid Dynamics*. Scientific Computation. Springer, 2007.
- [15] S.A. Orszag C.M. Bender. *Advanced Mathematical Methods for Scientists and Engineers*. Springer, 1999.
- [16] James W Cooley and John W Tukey. An algorithm for the machine calculation of complex fourier series. *Mathematics of computation*, 19(90):297–301, 1965.
- [17] T.H. Cormen, C.E. Leiserson, R.L. Rivest, and C. Stein. *Introduction To Algorithms*. MIT Press, 2001.
- [18] Steven C Crow. Stability theory for a pair of trailing vortices. *AIAA journal*, 8(12):2172–2179, 1970.
- [19] A. Deloncle, P. Billant, and J.-M. Chomaz. Nonlinear evolution of the zigzag instability in stratified fluids: a shortcut on the route to dissipation. *J. Fluid Mech*, 660:229–238, 2008.
- [20] A. Deloncle, P. Billant, and J.-M. Chomaz. Three-dimensional stability of vortex arrays in a stratified and rotating fluid. *J. Fluid Mech*, 678:482–510, 2011.
- [21] P.G. Drazin and W.H. Reid. *Hydrodynamic Instability*. Cambridge University Press, 2004.
- [22] Dale R. Durran. *Numerical Methods for Fluid Dynamics 2nd Edition*. Springer, 2010.
- [23] Matteo Frigo and Steven G Johnson. The design and implementation of fftw3. *Proceedings of the IEEE*, 93(2):216–231, 2005.
- [24] D.A. Herbert and S.M. de Bruyn Kops. Predicting turbulence in flows with strong stable stratification. *Phys. Fluids*, 18:18–28, 2006.
- [25] R. Kerswell. Elliptical instability. *Annu. Rev. Fluid Mech.*, 34:83–113, 2002.
- [26] David Kimmler. *A First Course in Fourier Analysis*. Cambridge University Press, 2008.



- [27] Kundu. *Fluid Dynamics 5th Edition*. Academic Press, 2012.
- [28] M. Lesieur. *Turbulence in Fluids*. Springer, 2008.
- [29] R. LeVeque. *Finite Difference Methods for Ordinary and Partial Differential Equations: Steady-State and Time-dependent Problems*. Society for Industrial and Applied Mathematics, 2007.
- [30] T. Leweke and C.H.K. Williamson. Cooperative elliptic instability of a vortex pair. *J. Fluid Mech*, 360:85–119, 1998.
- [31] T. Leweke and C.H.K. Williamson. Long-wavelength instability and reconnection of a vortex pair. In E. Krause and K. Gersten, editors, *IUTAM Symposium on Dynamics of Slender Vortices*, volume 44 of *Fluid Mechanics and Its Applications*, pages 225–234. Springer Netherlands, 1998.
- [32] D.K. Lilly. Stratified turbulence and the mesoscale variability of the atmosphere. *J. Atmos. Sci*, 40:749, 1983.
- [33] E. Lindborg. The energy cascade in a strongly stratified fluid. *J. Fluid Mech*, 550:207–242, 2006.
- [34] MathWorks. 2-d fast fourier transform. <http://www.mathworks.com/help/matlab/ref/fft2.html>.
- [35] V.V. Meleshko and G. J. F. van Heijst. On Chaplygin’s investigations of two-dimensional vortex structures in an inviscid fluid. *J. Fluid Mech*, 272:157–182, 1994.
- [36] C. Meyer. *Matrix Analysis and Applied Linear Algebra Book and Solutions Manual*. Matrix Analysis and Applied Linear Algebra. Society for Industrial and Applied Mathematics, 2000.
- [37] T. Miyazaki and Y. Fukumoto. Three-dimensional instability of strained vortices in a stably stratified fluid. *Phys. Fluids A*, 4:2515–2522, 1992.
- [38] Saffman PG. Moore DW. The instability of a straight vortex filament in a strain field. *Proc. R. Soc. Lond. A*, 346:413–425, 1975.
- [39] K. Ngan, D.N. Straub, and P. Bartello. Aspect ratio effects in quasi-two-dimensional turbulence. *Phys. Fluids*, 17:1–10, 2005.
- [40] P. Otheguy, P. Billant, and J.-M. Chomaz. Elliptic and zigzag instabilities on co-rotating vertical vortices in a stratified fluid. *J. Fluid Mech*, 553:253–272, 2006.

- [41] Orzag Peterson. Numerical simulation... *collection*, 66614914:1–1000, 1972.
- [42] R.T. Pierrehumbert. Universal short-wave instability of two-dimensional eddies in an inviscid fluid. *Phys. Rev. Lett*, 57(17):2157–2159, 1986.
- [43] Osborne Reynolds. An experimental investigation of the circumstances which determine whether the motion of water shall be direct or sinuous, and of the law of resistance in parallel channels. *Proceedings of the Royal Society of London*, 35(224-226):84–99, 1883.
- [44] J.J. Riley and S. M. de Bruyn Kops. Dynamics of turbulence strongly influenced by buoyancy. *Phys. Fluids*, 15(7):2047–2059, 2003.
- [45] J.J. Riley and M.-P. Lelong. Fluid motions in the presence of strong stable stratifications. *Annu. Rev. Fluid Mech.*, 32:613–657, 2000.
- [46] J.J. Riley and E. Lindborg. Recent progress in stratified turbulence. In K. Sreenivasan P. Davidson, Y. Kaneda, editor, *Ten Chapters in Turbulence*. Cambridge University Press, 2013.
- [47] RD Sharman and MG Wurtele. Ship waves and lee waves. *Journal of the Atmospheric Sciences*, 40:396–427, 1983.
- [48] Lloyd N. Trefethen. *Spectral Methods in MATLAB*. SIAM, 2000.
- [49] D.J. Tritton. *Physical Fluid Dynamics*. Oxford Science Publications. Clarendon Press, 1988.
- [50] Widnall SE Tsai C-Y. The stability of short waves on a straight vortex filament in a weak externally imposed strain field. *J. FLuid Mech*, 73:721–733, 1976.
- [51] G.K. Vallis. *Atmospheric and Oceanic Fluid Dynamics: Fundamentals and Large-scale Circulation*. Cambridge University Press, 2006.
- [52] Milton Van Dyke. *Perturbation Methods in Fluid Mechanics*. Parabolic Press Stanford, 1975.
- [53] Milton Van Dyke. *An Album of Fluid Motion*. Parabolic Press Stanford, 1982.
- [54] M.L. Waite. Stratified turbulence at the buoyancy scale. *Phys. Fluids*, 23:23–35, 2012.
- [55] M.L. Waite and P. Bartello. Stratified turbulence dominated by vortical motion. *J. Fluid Mech*, 517:281–301, 2004.

- [56] M.L. Waite and P.K. Smolarkiewicz. Instability and breakdown of a vertical vortex pair in a strongly stratified fluid. *J. Fluid Mech.*, 606:239–273, 2008.
- [57] R.M. Wald. *General Relativity*. University of Chicago Press, 2010.
- [58] F. Waleffe. On the three-dimensional instability of strained vortices. *Phys. Fluids A*, 3:76, 1990.
- [59] S.E. Widnall, D.B. Bliss, and C.Y. Tsai. The instability of short waves on a vortex ring. *J. Fluid Mech*, 66:35, 1974.
- [60] Wikipedia. Aliasing sines. <http://en.wikipedia.org/wiki/File:AliasingSines.svg>.
- [61] Wikipedia. Wagon-wheel effect. [http://en.wikipedia.org/wiki/Wagon-wheel\\_effect](http://en.wikipedia.org/wiki/Wagon-wheel_effect).